Fermilab FERMILAB-THESIS-2000-37

D_S CHARM STRANGE MESON PRODUCTION AND ASYMMETRY

by

Mithat Kaya

An Abstract

Of a thesis submitted in partial fulfillment of the
requirements for the Doctor of Philosophy
degree in Physics in the
Graduate College of The
University of Iowa

December 2000

Thesis supervisors: Professor Yasar Onel
Professor Edward McCliment

ABSTRACT

Charm hadroproduction physics has been studied by several experiments. One of them is the E781(SELEX) experiment which took data during 1996-1997. SELEX(SEgmented Large X baryon spectrometer) which was designed as a multi-stage spectrometer to study production and decay of charmed baryons is a fixed target experiment at Fermilab studying mostly charmed particles produced by Σ^- and π^- beams at 600 GeV. The production charge asymmetry of D_s mesons as a function of kinematical variables x_F and p_t^2 is presented here. The data sample used for this measurement is $D_s^\pm$ decays to $K^+K^-\pi^\pm$, which covers both resonant and non-resonant channels and $D_s^\pm$ decays to $\phi^0\pi^\pm$ and $\overline{K}^*(892)^0K^\pm$ resonant channels respectively.

Abstract approved: _____
Thesis supervisor

_____
Title and department

_____
Date

_____
Thesis supervisor

_____
Title and department

_____
Date

Graduate College
The University of Iowa
Iowa City, Iowa

CERTIFICATE OF APPROVAL

PH.D. THESIS

This is to certify that the Ph.D. thesis of

Mithat Kaya

has been approved by the Examining Committee
for the thesis requirement for the Doctor of
Philosophy degree in Physics at the December 2000
graduation.

Thesis committee: _____
Thesis supervisor

_____
Thesis supervisor

_____
Member

_____
Member

_____
Member

D_S CHARM STRANGE MESON PRODUCTION AND ASYMMETRY

by

Mithat Kaya

A thesis submitted in partial fulfillment of the
requirements for the Doctor of Philosophy
degree in Physics in the
Graduate College of The
University of Iowa

December 2000

Thesis supervisors: Professor Yasar Onel
Professor Edward McCliment

To My Parents

ACKNOWLEDGEMENTS

I would first like to sincerely and especially thank my thesis advisor, Yasar Onel. He helped me consistently and constructively the entire way. Without his guidance providing a spur to my confidence, I am sure I would not have been able to produce what I finally did. I would like to thank my thesis coadvisor Edward McCliment for his valuable advises, ideas and his continues support in every way possible. I owe a big thank to Maurizio Iori who suggested me to work on this topic and he gave me many ideas and supports during this work. I would like to thank Erhan Gülmez for his valuable ideas and supports. My big appreciation goes to SELEX collaborators. Especially Jim Russ, Peter Cooper, Soon.Y. Jun and Fernanda Gallinucci Garcia who gave me the ideas and helped on my questions. I also would like to thank Aldo Penzo who helped me a lot on my master thesis and gave me a huge moral and support on this one. I also wish to thank to all my friends in Iowa City and elsewhere for listening to my constant thesis stress and strain and having enough fun to keep me in control. I finally want to thank my parents for supporting me in every way possible.

TABLE OF CONTENTS

Page

LIST OF TABLES vi

LIST OF FIGURES viii

CHAPTER

I INTRODUCTION 1

II LEADING PARTICLE EFFECT 3

2.1 Lund String Fragmentation Model 5
2.2 Intrinsic Charm Model 7
2.3 Results from the previous experiments 8

III SEGMENTED LARGE-X SPECTROMETER(SELEX) 11

3.1 Beam Spectrometer 14
3.1.1 Beam Transition Radiation Detector 16
3.1.2 HST Silicon 16
3.1.3 Beam Silicon 18
3.2 The Vertex Spectrometer(Vertex Region) 18
3.2.1 Charm Targets 18
3.2.2 Vertex Silicon Detectors 18
3.3 M1 Spectrometer 20
3.3.1 M1 Multi-wire Proportional Chambers 21
3.3.2 Drift Chambers of the M1 Spectrometer 31
3.4 M2 Spectrometer 32
3.4.1 Hodoscopes 32
3.4.2 M2 wire chambers 33
3.4.3 Ring Imaging Cherenkov(RICH) 33
3.4.4 Detectors Involved in my Measurement 38

IV TRIGGER AND DATA ACQUISITION SYSTEM 39

4.1 Trigger Level Synchronization 40
4.2 Data Acquisition System 41

V DATA ANALYSIS 43

5.1 Event Selection Criteria 48
5.1.1 Statistical Significance 51
5.1.2 Contamination 56
5.2 Data Simulation 57
5.3 Acceptance 58
5.4 D_s Yields: Peak Fitting Method 61
5.5 D_s Yields: Sideband Subtraction Method 73
5.6 Statistical Error Analysis 75
5.6.1 Statistical error for the background subtracted signal . . . 75
5.6.2 Statistical error due to the combined efficiency and acceptance corrections 75
5.7 Systematic Error Analysis 76
5.7.1 Systematic errors due to the sideband subtraction method 76
5.7.2 Error in the efficiency and acceptance correction 77
5.7.3 Error making the cuts(various cuts used for event selection) 77
5.7.4 Systematic effect on asymmetries. 79
5.7.5 RICH efficiency effect: 79
5.7.6 $D^{\pm}$ contamination effect: 79

VI RESULTS AND CONCLUSIONS 80

6.1 x_F Distributions 80
6.2 p_t^2 Distributions 87
6.3 Asymmetry 89
6.3.1 x_F and p_t^2 Dependent Asymmetry 89
6.4 Integrated Asymmetry 95

VIIDISCUSSION OF THE RESULTS 96

APPENDIX

A THE SELEX (E781) COLLABORATION 99

B ADDITIONAL FIGURES 101

REFERENCES 111

LIST OF TABLES

Table		Page
1	Quark contents	3
2	Specifications of the charm targets	19
3	A sample control file for SOAP	45
4	Sample TSEG file	46
5	Sample RECON file	47
6	Sample KUMAC file	49
7	Default cuts	50
8	Optimized cuts	54
9	QQ Sample INPUT file	57
10	QQ Sample DECAY file	58
11	Sample of EMBEDDING output file.	58
12	D_s^- signal and background events from different beam types	65
13	D_s^- signal and background events from different beam types	67
14	D_s yield from different experiment	68
15	$D_s \to \phi\pi$ events from different beam types	69
16	$D_s \to K^*K$ events from different beam types	70
17	$D_s^\pm \to K^+K^-\pi^\pm$ from Σ^- beam	83
18	$D_s^\pm \to \phi\pi^\pm$ from Σ^- beam	84
19	$D_s^\pm \to K^\pm\overline{K}^*(892)^0$ from Σ^- beam	85
20	$D_s^\pm \to \phi\pi^\pm + K^\pm\overline{K}^*(892)^0$	85

21 $D_s^{\pm} \to K^+K^-\pi^{\pm}$ from π^- beam 86

22 Summary of the n parameters 86

23 $D_s^{\pm} \to K^+K^-\pi^{\pm}$ from Σ^- beam 87

24 Summary of the b parameters 88

25 Summary of Asymmetry(x_F) from Σ^- and π^- beam 94

26 Asymmetry(p_t^2) from Σ^- 94

LIST OF FIGURES

Figure Page

1 Production process 5

2 Example of string configuration 6

3 Example of intrinsic charm configuration 7

4 Asymmetries for D, D_s and Λ_c. The solid and dashed lines show results of calculations [1] and references therein. The dotted curve shows the results of tuned PYTHIA for π^- beam obtained by experiment E791 at FNAL [2] 9

5 Comparison of production asymmetry of D_s(solid circles) and D(open circles) from π^- beam obtained by experiment E791[8] 10

6 The SELEX experimental Layout. 12

7 Schematic view of the SELEX Spectrometer 13

8 The E781-SELEX Beam Spectrometer Layout 14

9 The Hyperon Magnet 15

10 BTRD planes active for beam particles 17

11 General layout of the apparatus and details of the charm production targets(figure is not scaled) 19

12 The Vertex silicon detectors 20

13 General view of M1 Spectrometer 21

14 Schematics of one of the MWPC 22

15 Orientation of M1PWC and M3PWCs planes 24

16 Mylar strips(garlands) in Multiwire Proportional chamber 25

17 The block diagram of the readout control logic 28
18 Plateau curves obtained with a Sr^{90} source for M1PWC with different gas mixtures 30
19 General view of M2 Spectrometer 33
20 Display of a Cherenkov light path in the RICH 35
21 Single event Display 36
22 Ring Radius(top) and separation(bottom) vs momentum distributions for interaction data for tracks with 95-105 GeV/c momentums. The two horizontal lines on the lower plot show the achieved resolutions for single track and multitrack events, respectively 37
23 Schematic view of SELEX Trigger Logic and Data Acquisition system . . 42
24 Upper graph shows the data taken with different beams at different runs (x axis run numbers) Lower picture is a percentage of different beams . . 43
25 Primary and secondary vertices and errors associated with them 50
26 Selected optimized cuts 52
27 ϕ Mass Spectrum before and after the probability cut 53
28 Momentum Spectrum of the first and second kaon of the ϕ before and after the probability cut 53
29 Statistical Significance 55
30 $K\pi\pi$ and $\pi K\pi$ Contamination 56
31 Reconstruction efficiency for $D_s^{\pm}$ vs x_F 59
32 Reconstruction efficiency for $D_s^{\pm}$ from 0.15 to 0.6 x_F. This region is used to correct the raw data 60
33 Ratio of reconstruction efficiency between D_s^- and D_s^+ from 0.15 to 0.6 x_F 60
34 Reconstruction efficiency for D_s^- and D_s^+ mesons as a function of p_t^2 . . . 61

35 Ratio of reconstruction efficiency between D_s^- and D_s^+ measons as a function of p_t^2 62
36 D_s and D mass distributions from all three beams(Σ^-, π^- and *proton*) . 63
37 The left and right figures show the D_s^- and D_s^+ mass spectrum from all three beams(Σ^-, π^- and *proton*) 64
38 Mass spectrum of D_s^- and D_s^+ from the Σ^-, π^- and *proton* beam 66
39 Mass Resolution from data 67
40 Mass Resolution from embedding monte carlo simulations 68
41 $\phi^0 \to K^-K^+$ invariant mass distribution 69
42 $K^{*0}(892) \to K^-\pi^+$ invariant mass distribution 70
43 $D_s \to \phi\pi$ mass distributions. Top: Invariant mass distributions from the combined Σ^-, π^-, and *proton* beam(left) and Σ^- beam (right). Bottom: D_s^-(left) and D_s^+(right) from Σ^- beam only 71
44 $D_s \to K^*K$ mass distributions. Top: Invariant mass distributions from the combined Σ^-, π^-, and *proton* beam(left) and Σ^- beam (right). Bottom: D_s^-(left) and D_s^+(right) from Σ^- beam only 72
45 Left/right sideband and signal regions used for sideband subtraction method 74
46 Systematic study on the sideband subtraction method. Upper and lower dots are the n parameter for D_s^+ and D_s^- respectively 78
47 x_F distribution of $D_s^\pm \to KK\pi^\pm$ charm strange meson 82
48 x_F distribution of $D_s^\pm \to K^*K + \phi\pi$ charm strange meson 82
49 x_F distribution of D_s^-(left) and D_s^+(right) charm strange meson from π^- beam 84
50 p_t^2 distribution of $D_s^\pm$ charm strange mesons 88
51 $D_s \to KK\pi$ production asymmetry as a function of x_F from Σ^- beam . . 90

52 $D_s \to K^*K + \phi\pi$ charm strange meson production asymmetry as a function of x_F from Σ^- beam 91
53 $D_s \to KK\pi$ production asymmetry as a function of x_F from π^- beam . . 92
54 $D_s \to KK\pi$ production asymmetry as a function of p_t^2 93
55 Integrated Asymmetry of D_s from Σ^- and π^- beam 95
56 The acceptance corrected x_F distribution from Σ^- beam 97
57 Comparison of the D_s production asymmetry as a function of x_F from a Σ^- beam. The acceptance corrected data are integrated over the x_F interval (0.15 - 0.6) for SELEX data and (0.2 - 0.7) for WA89 data . . . 98
58 Mass distributions of $D_s^- \to K^+K^-\pi^-$ for different x_F ranges from Σ^- beam. y and x axis's show number of events(10 MeV/c^2) and invariant mass(GeV/c^2) respectively 101
59 Mass distributions of $D_s^+ \to K^+K^-\pi^+$ for different x_F ranges from Σ^- beam. y and x axis's show number of events(10 MeV/c^2) and invariant mass(GeV/c^2) respectively 102
60 Mass distributions of $D_s^- \to K^*K^-$ for different x_F ranges from Σ^- beam. y and x axis's show number of events(10 MeV/c^2) and invariant mass(GeV/c^2) respectively 103
61 Mass distributions of $D_s^+ \to K^*K^+$ for different x_F ranges from Σ^- beam.y and x axis's show number of events(10 MeV/c^2) and invariant mass(GeV/c^2) respectively 104
62 Mass distributions of $D_s^- \to \phi\pi^-$ for different x_F ranges from Σ^- beam. y and x axis's show number of events(10 MeV/c^2) and invariant mass(GeV/c^2) respectively 105

63 Mass distributions of $D_s^+ \to \phi\pi^+$ for different x_F ranges from Σ^- beam. y and x axis's show number of events(10 MeV/c^2) and invariant mass(GeV/c^2) respectively 106

64 Mass distributions of $D_s^- \to K^-K^+\pi^-$ for different x_F ranges from π^- beam. y and x axis's show number of events(10 MeV/c^2) and invariant mass(GeV/c^2) respectively 107

65 Mass distributions of $D_s^+ \to K^-K^+\pi^+$ for different x_F ranges from π^- beam. y and x axis's show number of events(10 MeV/c^2) and invariant mass(GeV/c^2) respectively 108

66 Mass distributions of $D_s^- \to K^-K^+\pi^-$ for different p_t^2 ranges from Σ^- beam. y and x axis's show number of events(10 MeV/c^2) and invariant mass(GeV/c^2) respectively 109

67 Mass distributions of $D_s^+ \to K^-K^+\pi^+$ for different p_t^2 ranges from Σ^- beam. y and x axis's show number of events(10 MeV/c^2) and invariant mass(GeV/c^2) respectively 110

CHAPTER I
INTRODUCTION

The Leading particle effect is an enhancement of a production process that occurs when the produced particle shares a quark with the beam particle. This effect has been tested for charm hadroproduction using a number of different beams at different energies. Prior to this measurement only one experiment [1] has used a Σ^- beam to test the Leading Particle model on the $D_s^\pm$ production, but the statistics were insufficient for a detailed study. Other experiments have used pions [2, 3], kaons [3], and photons[3] as the beam to study the leading particle effect. In this work we report a study of the the production asymmetry of D_s charmed strange mesons produced by a Σ^- and π^- beams.

The purpose of this study is to test the "Leading Particle" model for the charm strange mesons, $D_s^\pm$, using hyperon beams. D_s^- is a leading particle for the Σ^- beam, because they both have one strange quark, s, in common. On the other hand, neither of the D_s mesons is a leading particle for the π^- beam. We determine the dependence of the asymmetry on x_F, the Feynman-X parameter and p_t^2, the transverse momentum squared and compare with theoretical models.

This study was done with data from Fermilab experiment E781, (SELEX), a fixed target experiment that uses a multi-stage spectrometer designed for large acceptance of x_F values >0.1.

The overall purpose of the SELEX experiment is to understand charm production in the forward hemisphere and to increase the statistics of charm physics events

in order to study charm baryon decays better. SELEX used both negative(50%Σ^- and 50%π^-) beam at 600 GeV/c and positive beam (92% p and 8% π^+) at 540 GeV/c during the 1996-1997 fixed target run at Fermilab.

The theory of leading particle effect will be discussed in Chapter Two. Chapter three describes the setup of the experiment and detector systems. Trigger and Data Acquisition System are in Chapter four. Chapter five explains the analysis for extracting the asymmetry and doing the error analysis. Chapter Six will include results and conclusions about the present study and last chapter will be the general discussion of the results.

CHAPTER II
LEADING PARTICLE EFFECT

The production mechanism of charmed particles with hyperon beams is being studied both experimentally [1] and theoretically [4]. The leading particle effect has been proposed to address the issue of asymmetric production of different charged states of the hadrons. The asymmetry observed in the production of particles between those sharing a quark with the beam and those that do not is sometimes called the leading particle effect.

Previous studies of charm particle production show large enhancements in the forward production of charmed particles(leading particles) that share one or two quarks with the beam particle relative to those(non-leading particles) that do not share any quark[1, 2, 3, 5].

D_s mesons were produced using Σ^- and π^- hyperon beams. Since D_s^- consists of one $\overline{c}$ and one s quark, it shares one quark with the Σ^- beam (leading particle). However, D_s^+, which has one c and $\overline{s}$, does not share any quark with the neither Σ^- nor π^-beam (non-leading particle). The valence quark content of the beam particles

Table 1: Quark contents

Beam Type	$D_s^-(\overline{c}s)$	$D_s^+(c\overline{s})$
Σ^- (sdd)	leading	non-leading
π^- $(\overline{u}d)$	non-leading	non-leading

and charm mesons are given in the Table 1

Leading particle effect can be quantified by measuring a production asymmetry of two charge conjugate states. The asymmetry for D_s production is defined as

$$A \equiv \frac{N_{D_s^-} - N_{D_s^+}}{N_{D_s^-} + N_{D_s^+}}$$

where $N_{D_s^-}$ is the number of negatively charged D_s^-(Leading) mesons and $N_{D_s^+}$ is the number of positively charged D_s^+(non-leading) mesons produced in a particular bin of x_F or p_t^2.

The production of a charm hadron can be described in two steps: a "hard" process of $c\bar{c}$ production and a "soft" process of hadronization of $c/\bar{c}$ quarks to real hadrons. Many aspects of the hard process(Figure 1) are adequately described by next-to-leading order (NLO) Perturbative Quantum Chromodynamics (PQCD) calculations [6],[7]. However, PQCD predicts only very small $\approx 1\%$ asymmetry between c and $\bar{c}$ produced[8]. One must look to the hadronization (soft process), to explain the large asymmetries that have been observed in charm hadroproduction[1, 2]. This asymmetry has been accounted for by recombination of charm quarks/anti-quarks with the valance quarks from the beam particle.

Even though no theories exist for the leading particle effect, there are some phenomenological models that explain this effect in the framework of Quantum Chromodynamics(QCD). The most frequently used models are the string fragmentation model implemented in the Lund Model Monte Carlo program PYTHIA [4, 9, 10, 11, 12] and intrinsic charm (coalescence of charm and valence quarks when both originate in the

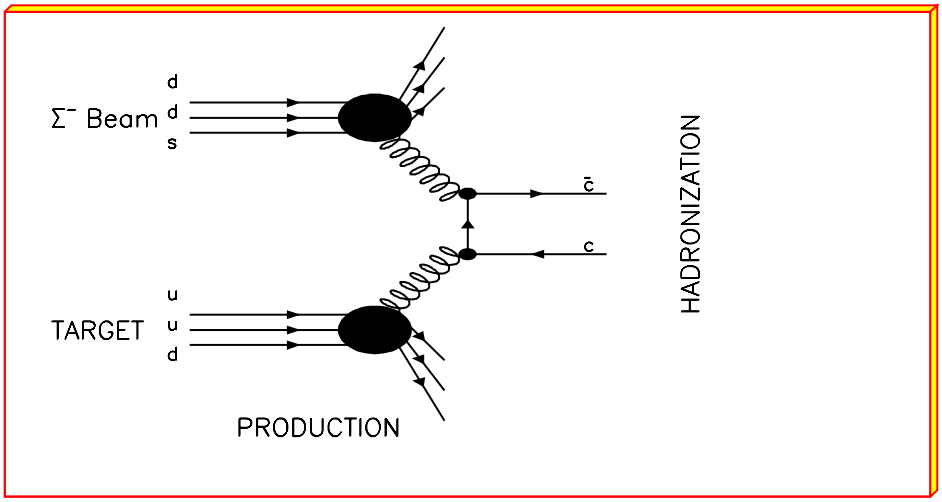

Figure 1: Production process

beam particle[13], [14],[15]).

2.1 Lund String Fragmentation Model

The Lund String fragmentation model, also known as a "Beam Dragging" model, indicates a strong dependence on the valence quark composition of the beam particle. According to this model when the produced heavy quark combines with a remnant light quark from the beam particle the produced heavy quark gains momentum. This causes leading charm particles to have a harder x_F spectrum than non-leading particles.

For instance(see Figure 2), in the inclusive reaction $\Sigma^- A \rightarrow D_s X$, charmed meson, $D_s^-(s\overline{c})$ is produced by recombination of the s valance quark from Σ^- with the $c\overline{c}$ pair from fission of a string. The D_s^- in this reaction produced more copiously than the D_s^+.

Basically in this model incoming beam remnants and the partons of the hard

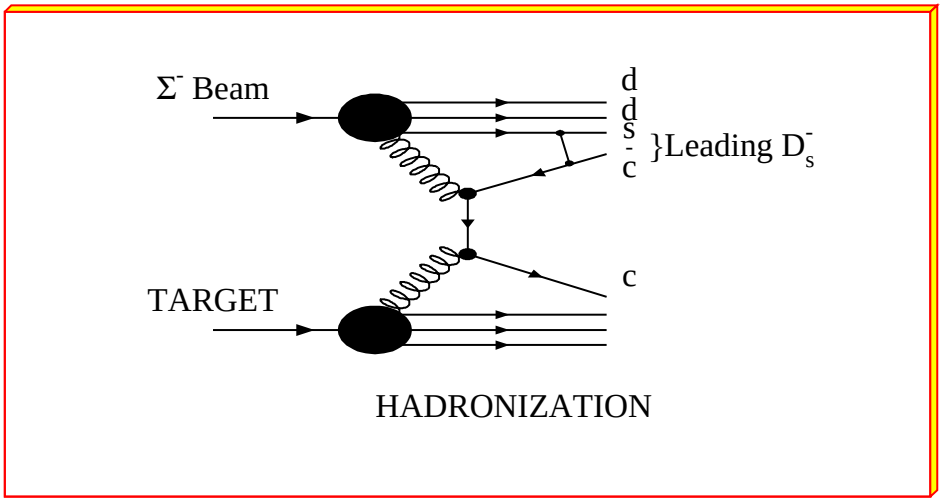

Figure 2: Example of string configuration

interaction are connected by strings. Each string piece has a color charge at one end and its anticolor at the other. The double color charge of the gluons is attached to two string pieces, while a quark is only attached to one. A diquark is considered as being in a color antitriplet and it acts like an antiquark. Then each string contains a color triplet end point, a number of intermediate gluons and a color antitriplet end. The string topology can be derived from the color flow of the hard process. Because of the color flow in an event, the produced charm quarks normally are color connected to the beam remnants of the incoming particles. This results in the possibility of a charmed hadron gaining energy and momentum from the beam remnant in the fragmentation process and thus to be produced at larger rapidity than the initial charm quark. In the extreme case the color singlet containing the charm quark and the beam remnant has a small invariant mass. Then the color singlet, called a cluster, will be forced to collapse into a meson, giving a hard leading particle. The corresponding production mechanism for non-leading particles involves sea-quarks and is therefore suppressed.

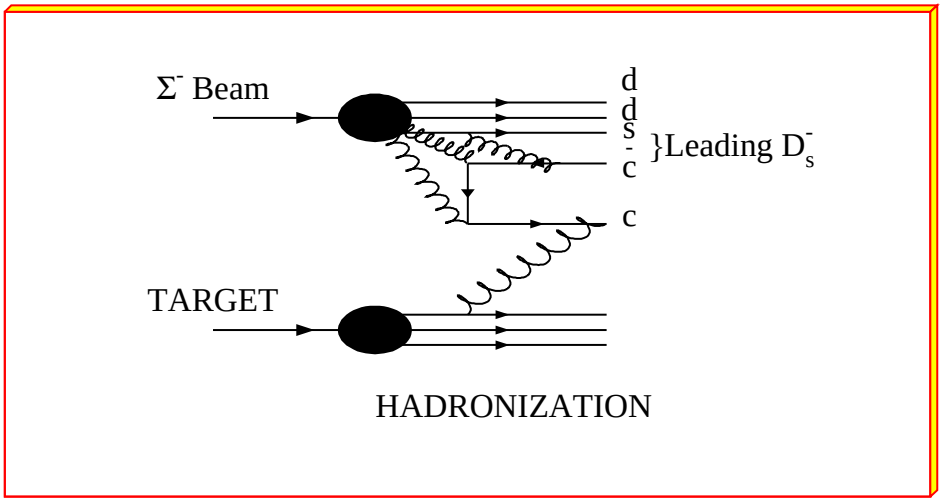

Figure 3: Example of intrinsic charm configuration

The qualitative nature of the asymmetry can thus be understood within the "string model".

2.2 Intrinsic Charm Model

The $c\bar{c}$ pair produced by the sea quarks coalesces with valance quarks of a beam due to their similar rapidity, forming a leading particle(Figure 3). This is the basic assumption of the intrinsic charm model [13].

The coalescence of charmed quarks with projectile valance quarks may occur in the initial state. A beam particle wave function may fluctuate into Fock states. For instance $\Sigma^-(dds)$ can fluctuate into $|ddsc\bar{c}>$ and produce $D_s^-(s\bar{c})$ and $D_s^+(c\bar{s})$. This kind of fluctuation occurs in QCD when two or more gluons are attached to the charm quarks. The highest fluctuation occurs when the partons have equal velocities. Since the charm and valance quarks have the same rapidity, the heavy quarks carry a fraction of the projectile momentum, and this heavy and light quarks coalesce to

produce leading charm correlations at large longitudinal momentum(x_F)[16],[17] so that the production asymmetry is expected to increase at large x_F and decrease at large p_t^2.

2.3 Results from the previous experiments

WA89[1] was the first experiment to study charmed particles produced by a $\Sigma^-(dds)$ beam on nuclear targets. They found considerable production asymmetries between $D^-(\overline{c}d)$ (leading) and $D^+(\overline{d}c)$ (nonleading), $D_s^-((\overline{c}s)$ (leading) and $D_s^+(\overline{s}c)$ (nonleading) and $\Lambda_c(udc)$ (leading) and $\overline{\Lambda}_c(\overline{u}\overline{d}\overline{c})$ (nonleading) (Figure 4). The production asymmetry of D_s (middle plot) measured by the WA89 is favored D_s^- (leading) for Σ^- beam.

On the other hand E791[2] experiment which used π^- beam at 500 GeV/c momentum found no asymmetry between $D_s^\pm$ production. In this case $D_s^\pm(\bar{c}s, \bar{s}c)$ is not a leading particle for $\pi^-(\bar{u}d)$ beam. On the contrary they have found a huge asymmetry in favor of D^-(leading) and D^+(nonleading) for the π^- beam[8]. Figure 5 shows the comparisons of the production asymmetry of D_s and D from π^- beam. The solid line shows the asymmetry predicted by the PYTHIA Monte Carlo program (improved by E791)[8].

An intrinsic charm model predicts zero asymmetry for D_s production at all x_F and p_t^2. E791 concluded that asymmetry is coming from the hadronization process and not from the production of the charm quarks themselves.

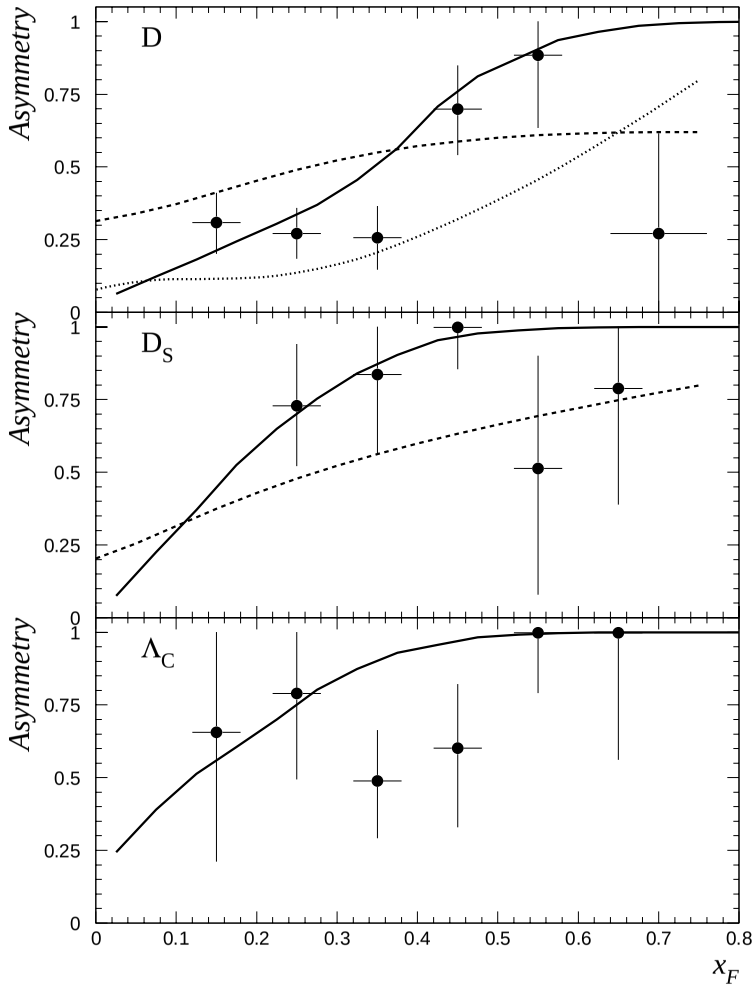

Figure 4: Asymmetries for D, D_s and Λ_c. The solid and dashed lines show results of calculations [1] and references therein. The dotted curve shows the results of tuned PYTHIA for π^- beam obtained by experiment E791 at FNAL [2]

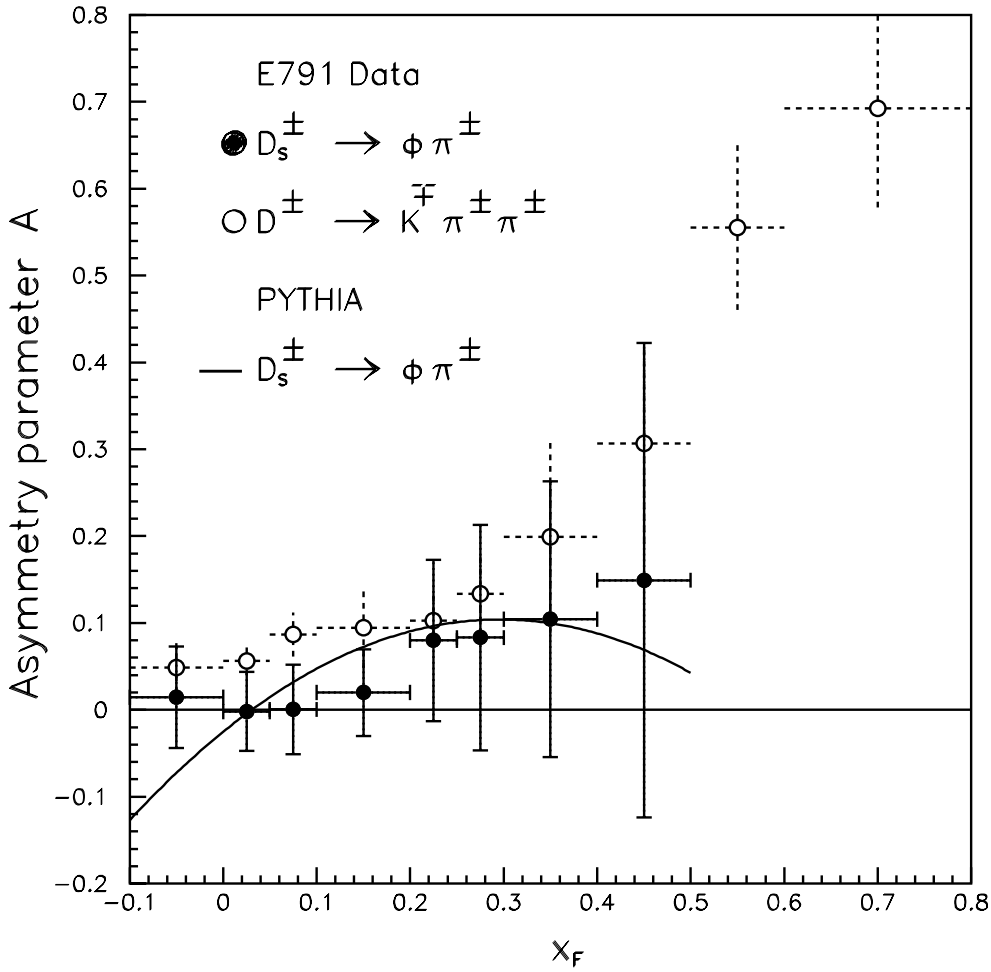

Figure 5: Comparison of production asymmetry of D_s(solid circles) and D(open circles) from π^- beam obtained by experiment E791[8]

CHAPTER III
SEGMENTED LARGE-X SPECTROMETER(SELEX)

The E781 (SELEX) experiment was commissioned and ran during a seven month period in 1996 and 1997. The experiment collected 15.2 billion interaction events. The collaboration is composed of about 115 physicists from 20 institutions worldwide(see Appendix A).

The layout of the experiment is shown in Figure 6 and details of the spectrometer can be seen in Figure 7.

One of its main function is a 3-stage charged particle spectrometer that has been designed and implemented to detect the charm particles. Each stage includes a bending magnet and a detector system. The detector has an acceptance of 0.1< x_F <1.0, where x_F is the Feynman-X parameter. One of the reasons for choosing this type of geometry is because in the high x_F region the particles have higher momentum and lower multiple scattering. This improves the vertex resolution and allows us to trigger on tracks with large miss distance.

The Fermilab Tevatron delivered a 800 GeV/c primary proton beam, 5x$10^{10} p/s$, to Proton Center (PC) per 20 second burst per minute. The proton beam spot size was on the order of 1 mm full width at half-maximum. E781-SELEX experiment was located at the proton center 4(PC4). The 800 GeV/c protons were steered onto a beryllium target which has dimensions of 1x2x400 mm^3 corresponding to one interaction length. The beryllium production target is located at the entrance to the hyperon magnet. For the remainder of this chapter we describe the portion of the

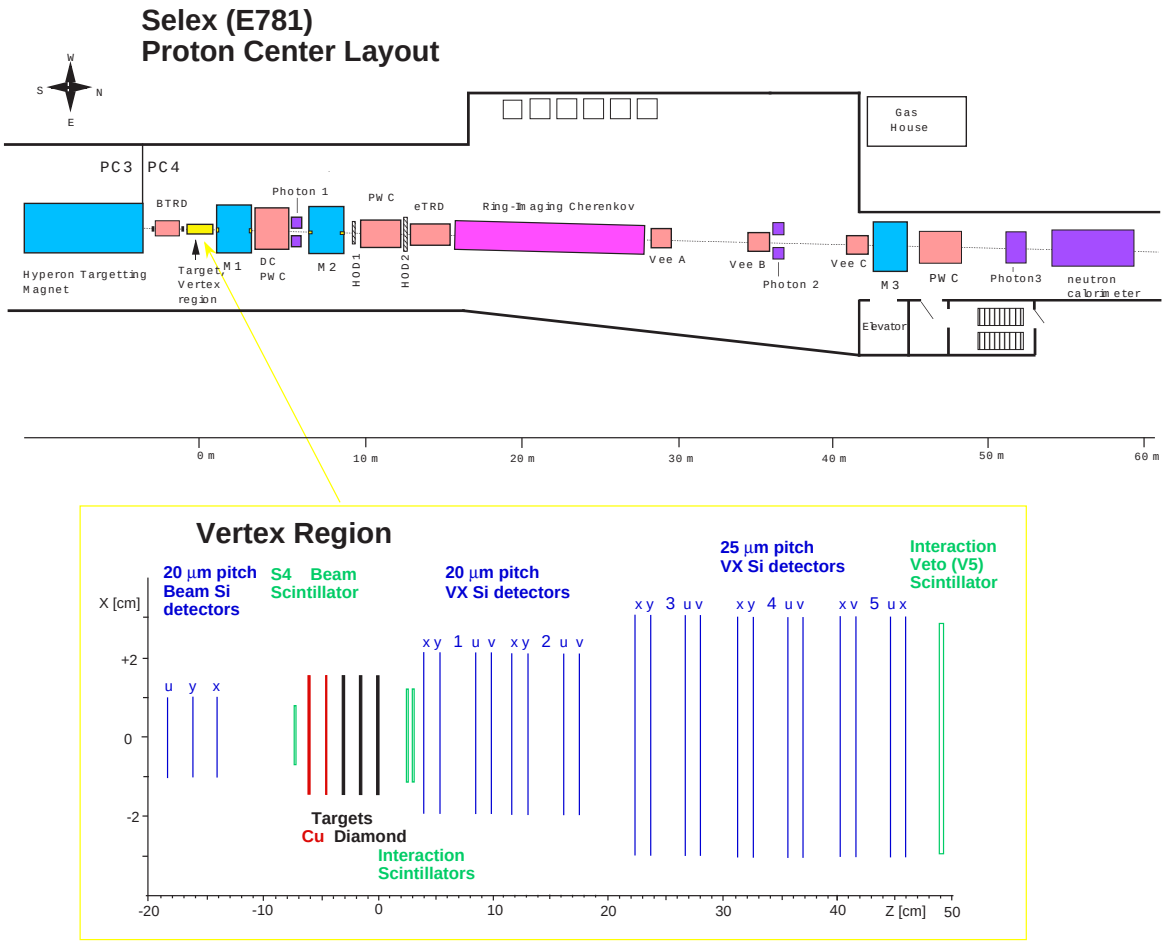

Figure 6: The SELEX experimental Layout.

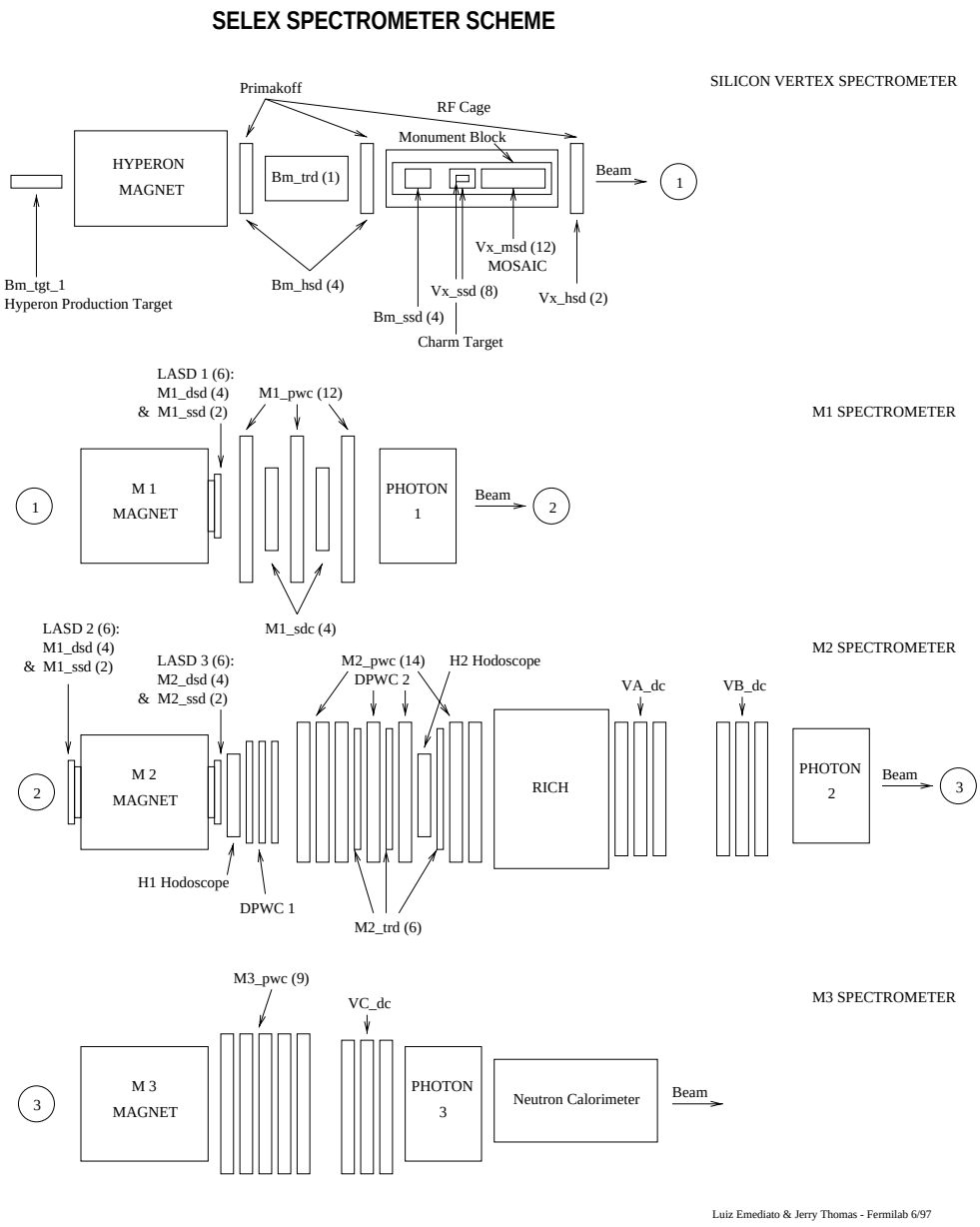

Figure 7: Schematic view of the SELEX Spectrometer

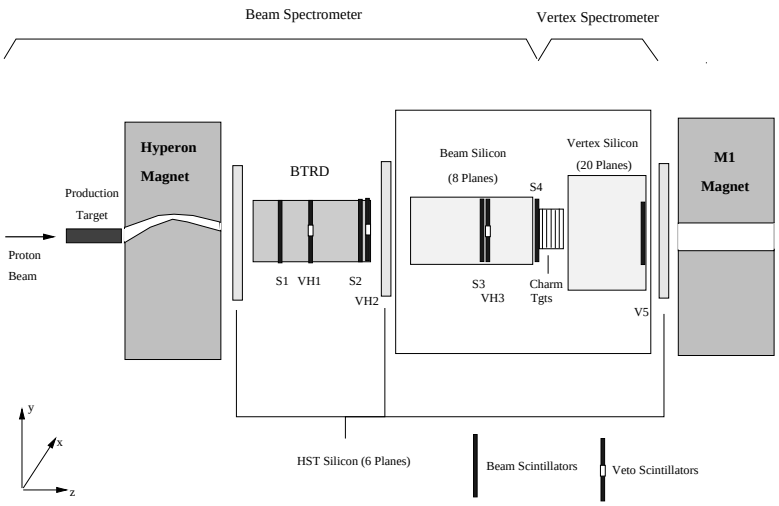

Figure 8: The E781-SELEX Beam Spectrometer Layout

apparatus which were used in this analysis.

3.1 Beam Spectrometer

The Beam Spectrometer (Figure 8) consists of the hyperon production target, Hyperon Magnet, Beam Transition Radiation Detectors (BTRDs), Hardware Scatter Trigger (HST) Silicon and Beam Silicon detectors. The Hyperon Magnet (Figure 9) was 7.3 m long and was operated at a field strength of 3.5 Tesla. The radius of curvature of the hyperon channel, which was made of tungsten, is 6.19 m [18]. The "hyperon" beam produced actually includes approximately 50% Σ^- and 50% π^- at the interaction target region. After emerging from the hyperon magnet, the secondary beam particles pass through the BTRDs.

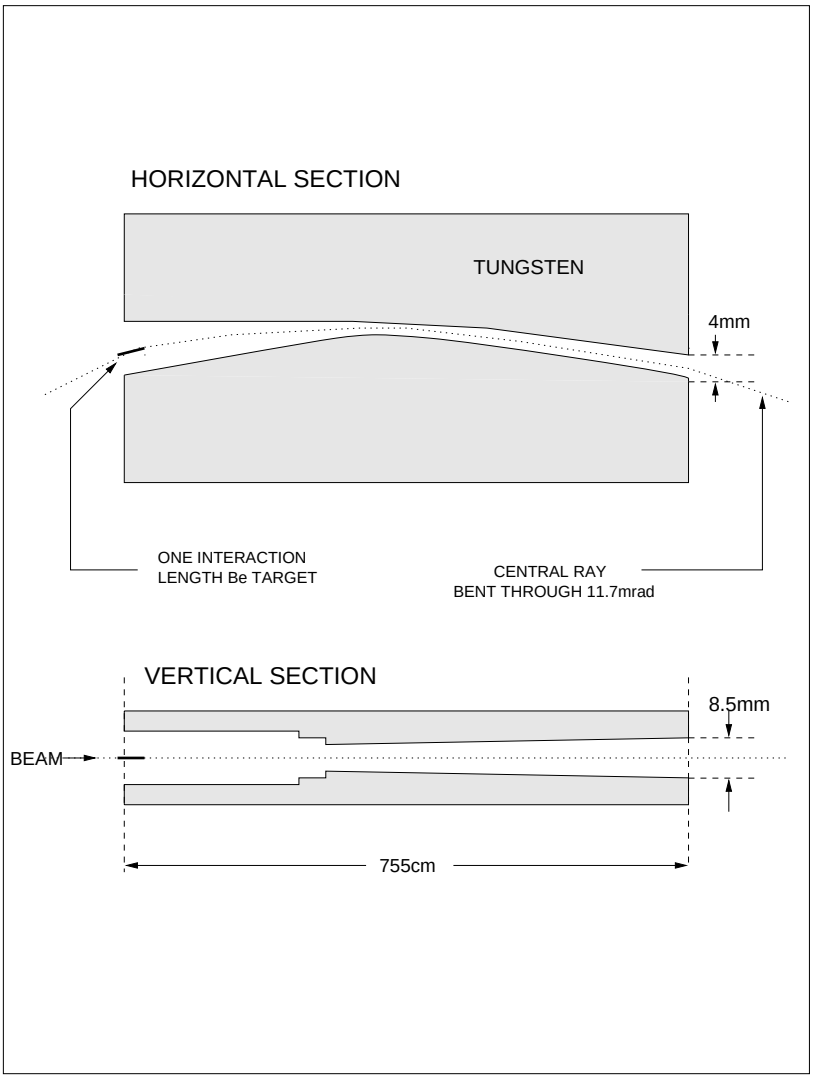

Figure 9: The Hyperon Magnet

3.1.1 Beam Transition Radiation Detector

The BTRD distinguishes between Σ^- and π^- in the beam and tags them for the 1-st level trigger. The BTRD is highly efficient and has a fast response time. Typical dead times of 70-80 nsec allows the BTRD to be used in the first level trigger. It consists of 10 identical modules. Each module contains 200 polypropylene foils, 17 μm thick, separated by 0.5 mm gap and 3 multi-wire proportional chambers. The gas flowing through the chambers is the mixture, Xe+30%CH_4. All three chambers are located in the same frame, which has a geometric acceptance of 3x3 cm^2 and a sensitive area of 2.2x2.2 cm^2. The proportional chambers contain aluminized mylar cathode planes and anode planes made of 15 μm thick gold plated tungsten wires with 1.0 mm wire separation. The separation between the anode and the cathode planes is 1 mm. The BTRD was placed between the hyperon magnet and vertex detector. The BTRD detects electromagnetic radiation (x-rays) radiated when a particle crosses the boundary between media with different dielectric properties.

Figure 10 displays a distribution of number of planes activated by the Σ^- and π^- beams when they pass through the detector.

3.1.2 HST Silicon

The hardware Scatter Trigger (HST) six (3x, 3y view) 50 μm pitch silicon detector planes located before the RF shielding (RF cage). These detectors are used for distinguishing beam scattered at small angles($> 150\mu$ rad) from non-interacting beam.

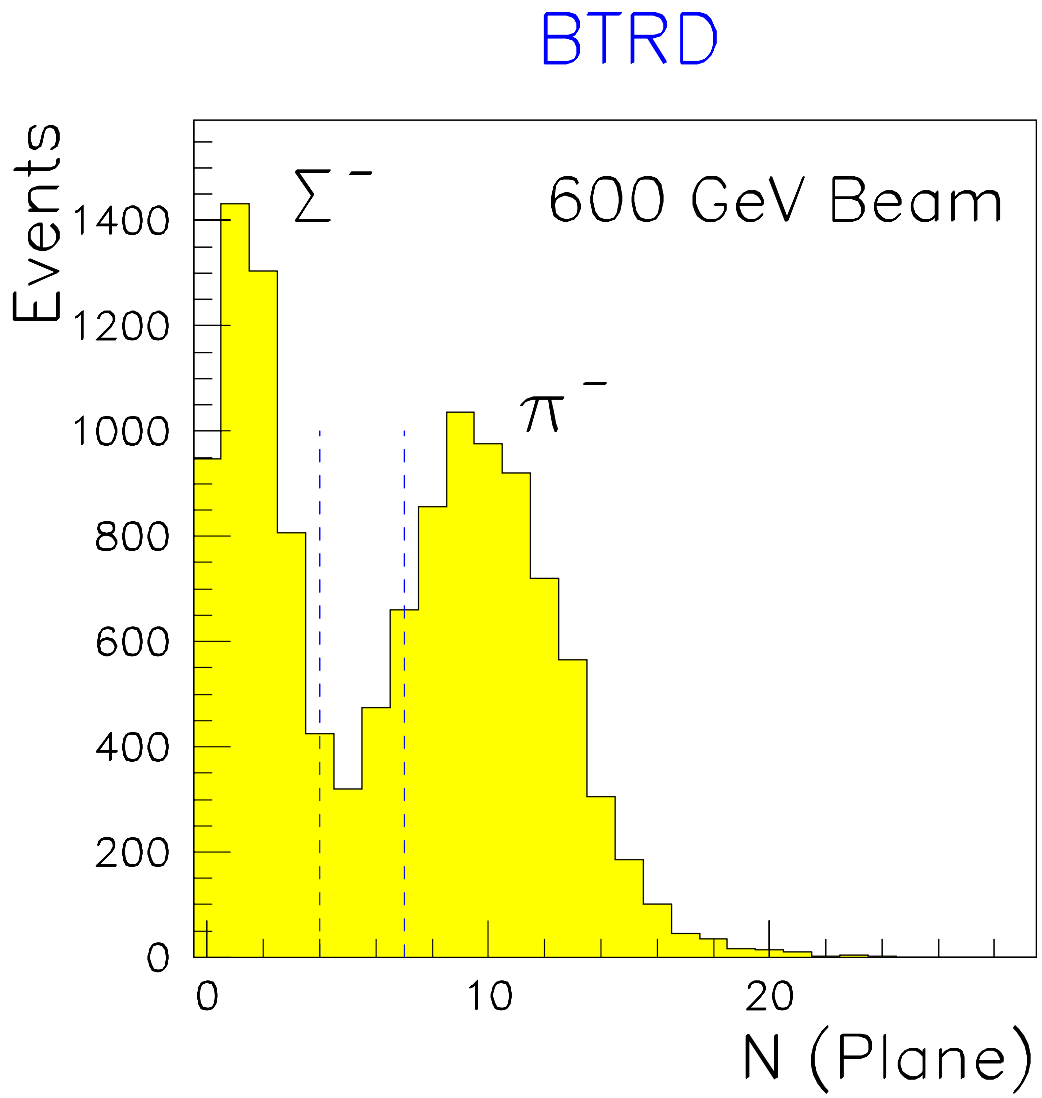

Figure 10: BTRD planes active for beam particles

3.1.3 Beam Silicon

The Beam silicon strip detectors (BSSD) provide precision tracking for high momentum small angle tracks including the beam particles. Reconstructed track efficiency and single hit efficiency are approximately 95 % and 99 %, respectively . It consists of 8 planes with 1024 strips with 20 μm pitch. The beam track measured in the silicon detectors is extrapolated upstream to the known position of the hyperon production target in order to determine the beam track momentum. Readout of these detectors were made possible by silicon vertex readout chip(SVX) with a variable integration gate period of up to 10 μsec. On the average four beam tracks were stored in the SVX between readouts.

3.2 The Vertex Spectrometer(Vertex Region)

The vertex region consists of charm targets and vertex silicon detectors. The detectors on this region have high resolution for interaction vertex and secondary vertices formed by the decay of the charmed particles. The targets and the vertex silicon detector systems are located in an aluminum box for RF shielding.

3.2.1 Charm Targets

There are five charm production targets: 2 copper blocks, which are 1.5 mm and 1.0 mm thick, and three diamond blocks, each 2.2 mm thick. Table 2 shows properties of the targets and Figure 11 shows their placement.

3.2.2 Vertex Silicon Detectors

The vertex silicon detector system (Figure 12) consists of 20 planes of 300 μm thick, single-sided silicon detectors. The planes are configured as 6 x-, 4 y-, 5 u-, and

Table 2: Specifications of the charm targets

Target Type	Z dist.(cm)	dim.(cm)	Int. Length(%)	Density (g/cm^3)
Copper	-6.08	2.54x2.54	1.06	8.96
Copper	-4.55	2.54x2.54	0.67	8.96
Diamond	-3.11	3.0x2.0	0.82	3.23
Diamond	-1.61	3.0x2.0	0.82	3.23
Diamond	-0.11	3.0x2.0	0.82	3.23

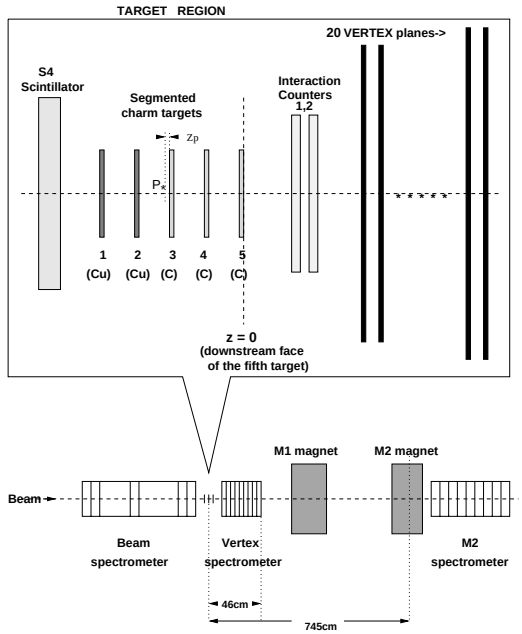

Figure 11: General layout of the apparatus and details of the charm production targets(figure is not scaled)

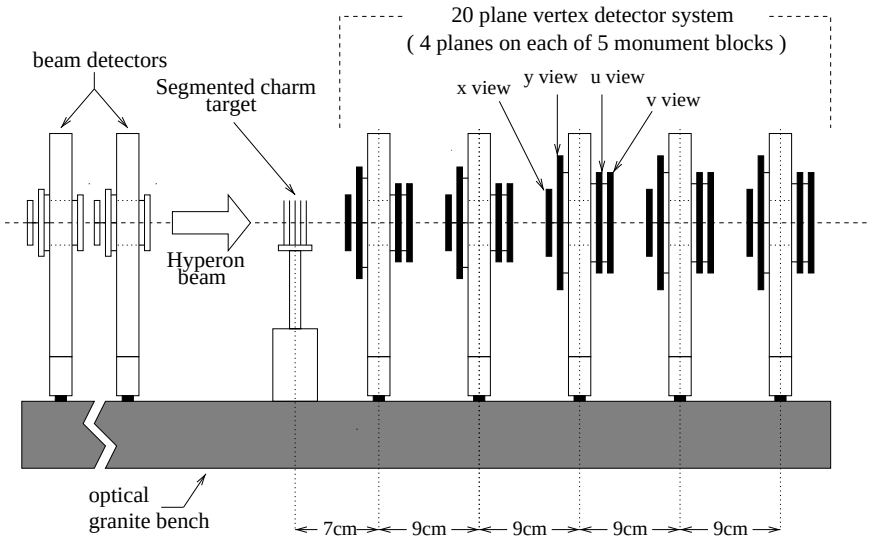

Figure 12: The Vertex silicon detectors

5 v-view detectors. The first two stations of these detectors have a sensitive region of 5.12x5.00 cm^2 with 2560 strips with a pitch of 20 μm. The last three detectors are the mosaic detectors each with a 25 μm pitch. These detectors provide high resolution (4 μm) tracking and vertex reconstruction.

3.3 M1 Spectrometer

The M1 spectrometer (Figure 13) is designed to measure the soft (low momentum) particles. It has a large angular acceptance to provide a low-momentum cut-off (2.5 GeV/c). This spectrometer has one bending magnet, three Multi-Wire Proportional Chambers (MWPCs) and two Drift Chambers (DCs). Each drift chamber is located between two MWPCs. The M1 magnet was operated at a field strength of 1.3 Tesla giving a p_t kick of 0.74 GeV/c.

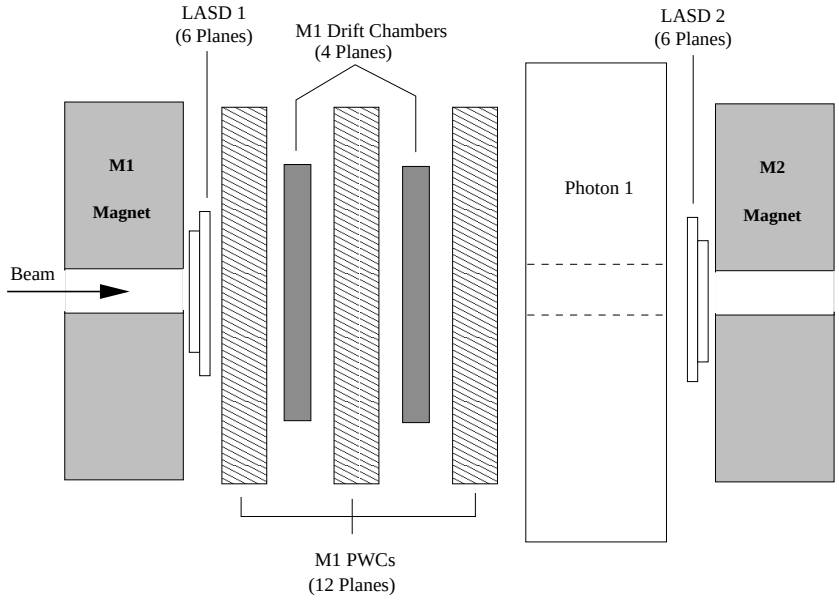

Figure 13: General view of M1 Spectrometer

The first sets of Large Angle Silicon Detectors (LASDs) are mounted on the downstream end plates of the M1 magnet. These consist of two single sided and two double-sided silicon detectors. The second and third sets of LASDs are mounted before and after the M2 magnet respectively. The detectors have active area 63.5x63.5 mm^2, and a thickness of 300 μm. The purpose of the LASDs is to cover the high momentum region of the wire and drift chambers to improve track resolution and separation in this regime and to allow a precise momentum measurement[19].

3.3.1 M1 Multi-wire Proportional Chambers

There are three large proportional chambers installed downstream of the M1 magnet as part of the M1 spectrometer.

The MWPCs are used to determine the position of charged particles. The external dimensions of each chamber are 2.390x2.390 m^2 and the internal dimensions

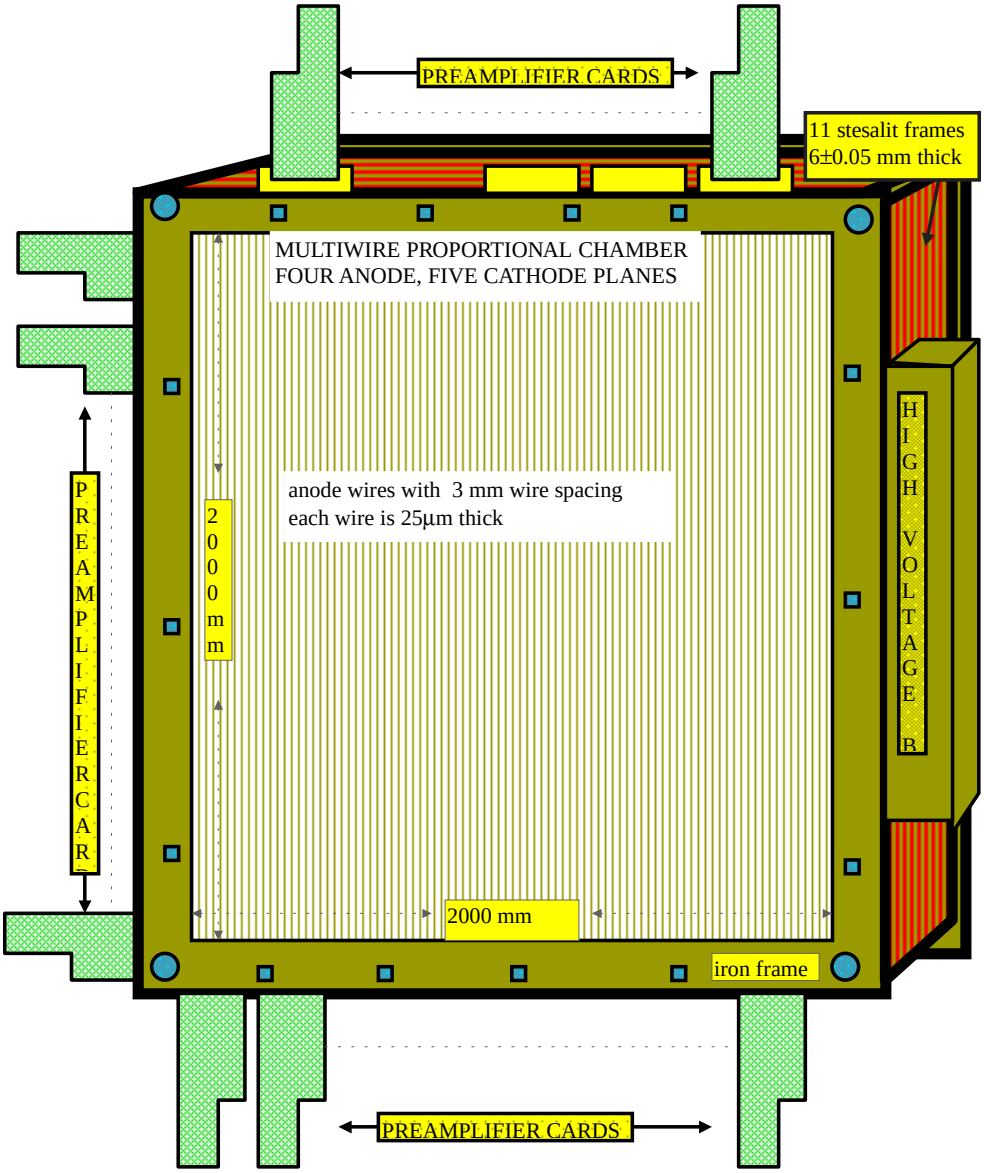

Figure 14: Schematics of one of the MWPC

are 2.0x2.0 m^2. Each chamber consists of 11 stesalit frames which are 6±0.05 mm thick, Figure 14 displays one of the MWPCs.

Each MWPC consists of a set of thin, parallel, equally spaced anode wires located between two cathode planes. For chambers with a sensitive area of 2x2 m^2, each plane is made of 640 gold plated tungsten wires, spaced 3 mm apart. There are four different anode plane orientations (X, Y, V and U)(in each MWPC), vertical, horizontal and slanted planes with an angle of $\pm$ 28.070 with respect to the vertical direction. The separation between two anode wire planes is 12$\pm$0.05 mm. Figure 15 shows the plate orientation of M1WPCs and M3WPCs.

Each chamber has two zigzag shaped Mylar strips (garlands), 5 mm wide, located between the cathode foils and the anode wires (top end not shown)(Figure 16). They reduce the mechanical free wire length to about 0.7 m. In case of unbalanced electrostatic force the garlands suppress the bending of the cathode foils. The garlands are 0.3 mm thick and they are attached to a supporting nylon wire at three points. The nylon wires are connected at both ends to the stesalit frames with a tension of 9.81 N (1 kg). There are also insulated field wires, 0.9 mm diameter, stretched along the garlands in the 1 mm space between the garlands and the anode wires. These field wires are used to restore the local chamber efficiency reduced by the garlands. The voltage on the wires is set to 1500 V.

Iron frames hold the 11 stesalit frames and cathode-anode planes together. The frames are made of iron because the thermal expansion coefficients of iron and stesalit are nearly the same. The MWPCs are assembled with pins and screws through the frames. The gas tightness is secured by O-rings placed in grooves in the chamber frames. There are four gas inlets and outlets distributed along two opposite sides of the frame to provide a uniform gas flow.

The signals from each wire are too weak to be transferred to the readout system directly. Preamplifiers are connected directly on the detector frame amplify the weak

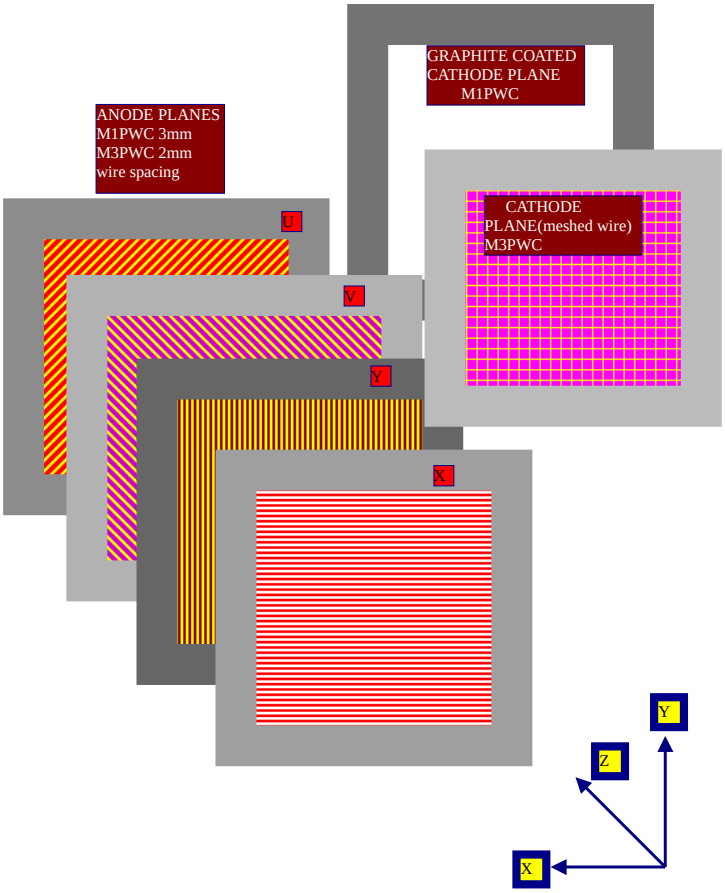

Figure 15: Orientation of M1PWC and M3PWCs planes

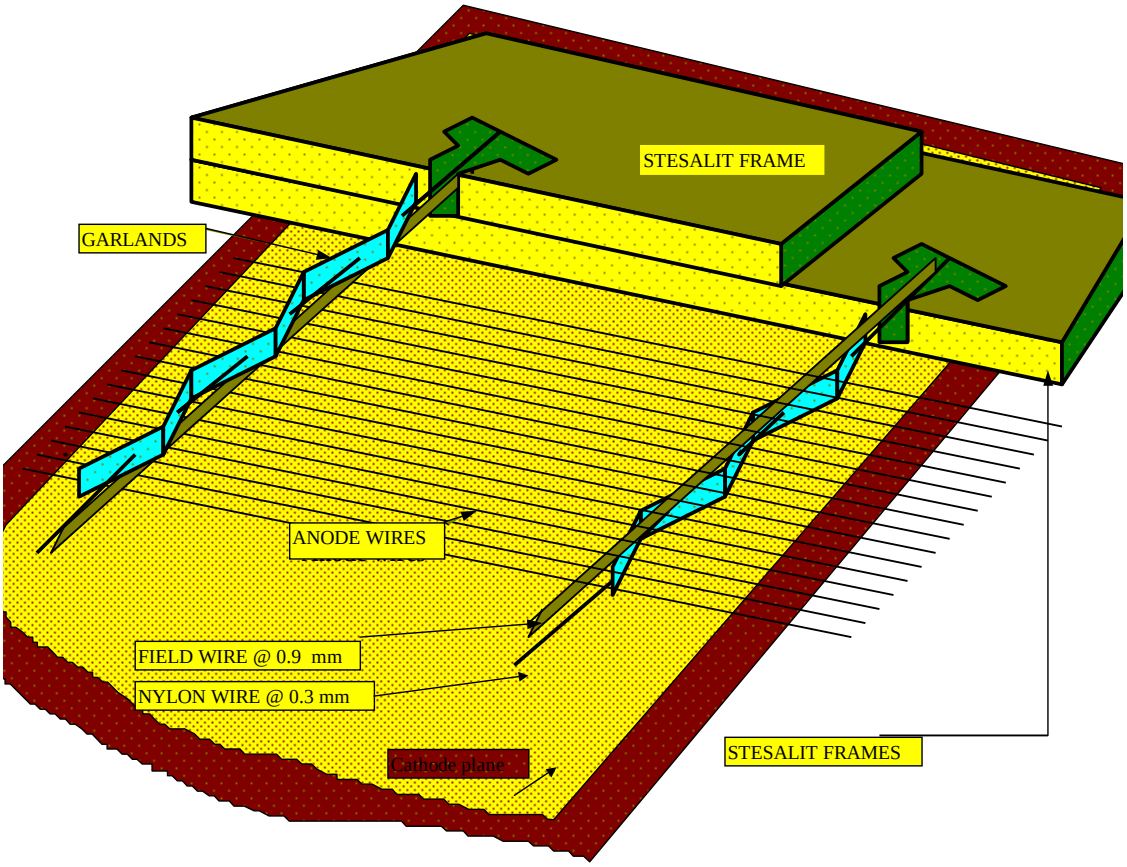

Figure 16: Mylar strips(garlands) in Multiwire Proportional chamber

signals and drive them through twisted pair cables from the preamplifiers to the readout system. Each preamplifier card contains 32 individual amplifiers with a differential gain of 7±1 for each channel. Preamp cards are supplied with -5.2 V.

3.3.1.1 Readout System

The RMH [20] (Receiver-Memory Hybrid) (Figure 17) readout system, developed at CERN, is used for the purpose of processing the PWC signals, encoding the resulting hit pattern, and transferring the encoded data to the main data acquisition system. Each RMH crate contains 22 RMH modules, 1 Crate Controller (CC), 1 Crate Encoder (CE). The overall RMH system is read out with 1 system Encoder (SE), Branch Receiver (BR), and Interface (IF). The RMH modules discriminate the received detector signals and strobe them into memory. The signals from the individual wires amplified by the preamplifier cards installed on the chambers come to the RMH modules via a special 32 pair twisted cable. The length of this cable is chosen so as to delay the chamber signals to allow enough time for the trigger to be formed. In the E781 experiment this cable length is 80 m long and it gives us 400 ns (1m=5ns) delay in the chamber signals. Each RMH module has inputs and outputs on the front panel and on the back. The front panel inputs consist of 32 signal wire inputs (push-pull via edge connector), a flag switch to indicate the beginning of a different detector in a specific unit, one fast strobe (NIM lemo connector) and a threshold control which can be screwdriver adjusted through a front panel trimpot in the Crate Controller (CC) unit. The threshold level measured at the monitor posts can be from -1.4 V to -5.2 V corresponding to -5mV to -25 mV in the signal. The threshold has to be set to such a voltage that all valid signals will be accepted and noise will be rejected. The outputs include a monitor giving real time signals for each

channel that has a nonzero input.

The rear connector inputs consist of a fast strobe (crate), a read, a reset, and a threshold control. Outputs consist of data (16x2 pins), a flag (1x2 pins), memory OR of upper 16 channels (2 pins), memory OR of lower 16 channels (2 pins), memory OR of 32 channels (2 pins) and a monitor (2 pins) [21].

The RMH modules are located in a special RMH crate that contains at most 22 RMH modules. Each crate should have a crate encoder (CE). Up to 16 CEs can be connected to the branch highway. All the CEs communicate with a system encoder (SE), which is mounted in a regular CAMAC crate.

Abbreviations in the Figure 17: DYC (Damn Yankee Controller:used for data buffer), INTF (Interface), EOE (End of Event), EOR (End of Read), ST/R (Strobe), DAQ (Data Acquisition), REN (Read Enable), REQ (Request), DISC (Discriminator), WST (Write strobe)

3.3.1.2 Efficiency Of The MWPC

Basically, the chamber efficiency depends on the number of electron-ion pairs produced and collected in the chamber. There are several aspects that affect the measured efficiency of the chambers. These are the composition of the gas mixture, high voltage applied, the threshold setting in the discriminators, and the gate width on the readout electronics that selects the correct signals. The MWPC efficiencies were over 90% during the run time. This number was determined by two different methods: source and beam method. In the source method, the chamber efficiency is calculated by locating the chamber between two beam-defining scintillation counters. Using the coincidence between the counters as a trigger, the number of signals coincident with this trigger divided by the number of triggers yields the efficiency [22]. Several

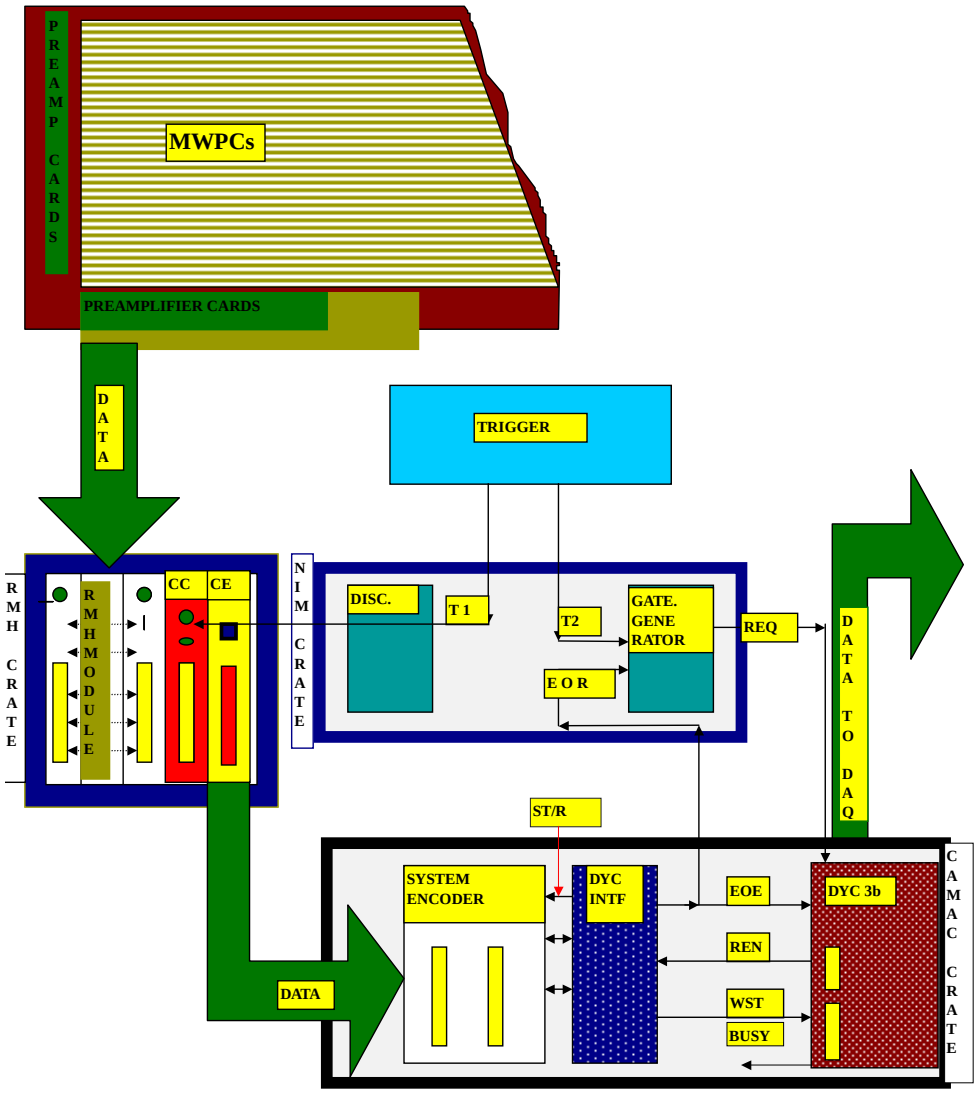

Figure 17: The block diagram of the readout control logic

tests have been done for the MWPCs. A Sr^{90} source that emits electrons with sufficient energy was placed in front of the chamber and a small scintillation counter was placed behind the chamber. Signals coming from the counter behind the chamber were assumed to be produced by the electrons that passed through the chamber. The efficiency in this case is obtained by dividing the number of chamber signals in coincidence with the scintillation counter signals divided by the number of scintillation counter signals. Several plateaus were obtained under different conditions (Figure 18). The first plateau curve is from a previous experiment (8/14/83). The other plateau measurements were done with a source with different gas mixtures (Figure 18) in the E781 experiment.

In the beam method, negative pions from the hyperon beam are used. The efficiency is calculated by using the pions whose tracks are determined by different detectors. For instance, for M1PWCs, beam, vertex, and M2 detectors are used to select a well defined pion-track that passes through the chambers. In this method, the entire track segments for such a pion from other detectors are combined to give a single full track. Then this track is either interpolated or extrapolated to a specific chamber plane position depending on the type of the track segments selected. The efficiency is then simply the ratio of the number of tracks that are accompanied with a nearby hit to the total number of tracks used. This way of measuring the efficiency is more realistic since it is done under actual running conditions. The efficiency of the M1PWCs is very high, with values of 97-99%.

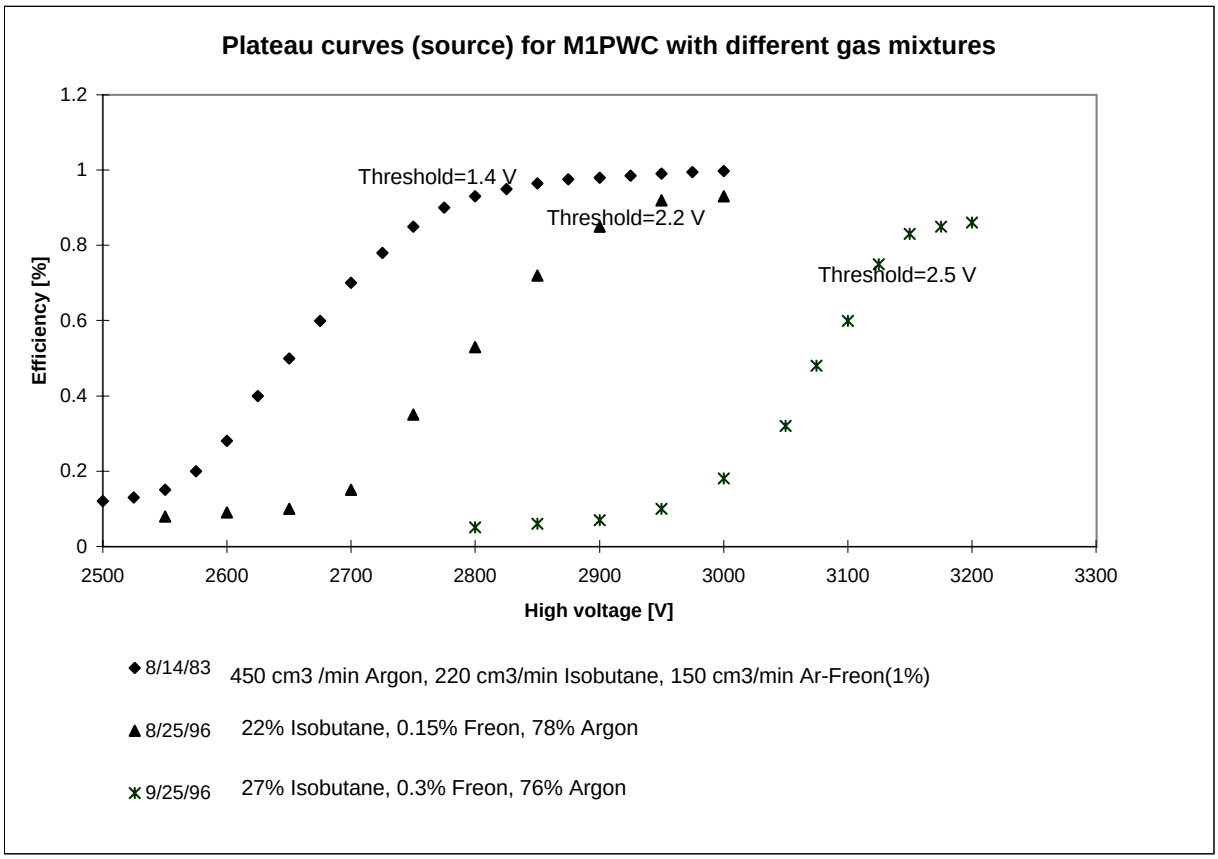

Figure 18: Plateau curves obtained with a Sr^{90} source for M1PWC with different gas mixtures

3.3.1.3 Gas Mixture

The most commonly used gas mixture is isobutane(24.5 %), argon(75 %), and freon-13B1(CF3Br)(0.5 %), which is the so-called magic gas. The exact concentrations may vary according to the chamber specifications. Various gas mixtures were tested for MWPCs. The highest efficiency is obtained with a gas mixture having 24.0 % isobutane, 0.15 % freon, and 75.85 % argon plus a small amount of isopropyl alcohol. The operating voltages were around 3.0 kV during the run period.

3.3.2 Drift Chambers of the M1 Spectrometer

The drift chambers of the M1 spectrometer were designed to improve the horizontal angular resolution of tracking in the M1 spectrometer in the horizontal bend plane of the M1 magnet. This is needed to enhance the momentum resolution of the M1 spectrometer for low momentum particles. Each drift chamber consists of a set of sensitive wires placed in uniform electric field created by a set of field-shaping wires. The electrons, created in the gas present in the chamber by high energy particles passing through the chamber, drift in the constant electric field to the sensitive wire and produce an electric pulse on it. These electric signals are amplified, digitized and transmitted to the time-to-digital converters. The principle of operation of drift chamber is the measurement of time interval between the passage of the particle through the chamber, as determined by some other detector having a good time resolution, and the electric signal from the sensitive wire. If the field is uniform, the drift velocity is constant and the drift time is proportional to the distance between the sensitive wire and the nearest track. Hence measuring the drift time of the electrons provides spatial information for a track.

3.3.2.1 Mechanical construction

Each detector consists of four drift chamber planes housed in two rectangular metal frames. The first and second planes of each sub chamber has 82 and 83 wires, respectively. Each plane has cells of 3 sizes: 3.2 cm coarse cells, 2.8 cm transitional cell and 2.4 cm fine cell. The center portion of a plane includes fine cells, the outer portion - coarse cells. Coarse and fine cells are separated from each other by 2 transitional cells, one on each side of the chamber. The operating voltage was 5900 V for each drift chamber.

3.4 M2 Spectrometer

The M2 Spectrometer is designed to detect high-momentum($>$ 15 GeV/c) decay products of charmed baryons,*i.e.* those with $x_F > 0.1$. The field strength and p_t kick of M2 magnet is 1.5 T and 0.845 GeV/c, respectively. In addition to the magnet the M2 spectrometer consists of 6 planes of LASD 6 planes of Drift Proportional Wire Chambers(M2 DPWC), 6 planes of electron Transition Radiation Detector(M2 eTRD), H1, H2 Hodoscopes, Ring Imaging Cherenkov Detector(RICH)[23], two stations of Vector Drift Chambers (Vee A, Vee B), and Photon 2 Detector. The general view of these detectors is shown in Figure 19. This part of the setup is important for tracking and particle identification purposes.

3.4.1 Hodoscopes

Downstream of LASD3 station, there are two scintillation counter hodoscopes located in the M2 spectrometer to provide multiplicity, charge, and momentum information for the trigger. Both hodoscopes cover the positive, negative, and neutral charge regions of the M2 spectrometer. The area covered by hodoscope 1 is

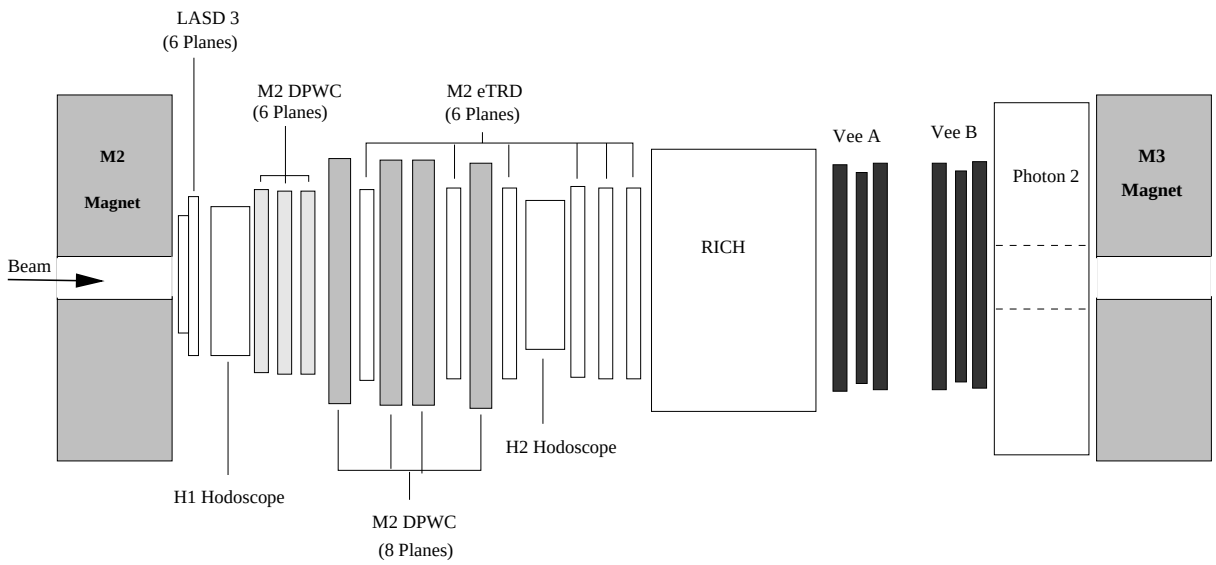

Figure 19: General view of M2 Spectrometer

60x30.5cm^2 and hodoscope 2 is 119x40.6cm^2.

3.4.2 M2 wire chambers

M2 spectrometer consists of 14 planes of Dual Proportional Wire Chambers in 7 modules which have x, y, u, and v view. These detectors have an active region of 60x60 cm^2 and 100x60 cm^2 and use magic gas. Most of the tracking in the M2 spectrometer is done using these detectors.

3.4.3 Ring Imaging Cherenkov(RICH)

Cherenkov radiation is emitted when the velocity of the charged particles, $v = \beta c$, exceeds the speed of light c/n in that medium which has a refractive index n(the $radiator$).

$v = >c/n$

The charged particles polarize the molecules, which then turn back rapidly to their ground state, emitting prompt radiation. The emitted light forms a coherent wavefront that is a conical shape. The opening angle θ_c of this cone is related to the particle's velocity by

$$cos\theta_c = \frac{1}{\beta n(w)} = \frac{1}{n(w)\sqrt{1-\frac{1}{\gamma^2}}}$$

where $\gamma = E/mc^2$ is the relativistic Lorentz factor and w is the frequency of the emitted radiation. This angle corresponds to the radius of the light-cone as seen by the phototubes in the detector.

A spherical mirror of radius of curvature r centered on the origin of the particle trajectory will focus the Cherenkov light cone into a ringlike image on the surface of a spherical detector of radius of curvature $r/2$ (Figure 20). The Cherenkov angle θ_c and γ can be calculated from the radius of this ring and matched to different particle hypotheses.

The Ring Imaging Cherenkov Detector is used for particle identification. It consists of 16 hexagonally shaped spherical mirrors with a total area of 2.4x1.2 m^2 and a focal length of 10 m and 2848 photo multiplier tubes. The RICH cylindrical vessel is 11 m long and 2.42 m in diameter; it is filled with neon gas. It is located about 16 m downstream of the charm production target, with the two analysis magnets, M1 and M2, with 800 MeV/c p_t-kick each in between, and it is surrounded by the multi-wire proportional and drift chambers that provide particle tracking. For the particle identification a maximum likelihood analysis is used for each track in the event. The algorithm uses tracking information to determine the ring centers and then examines hypotheses for several different particle types for each track. The

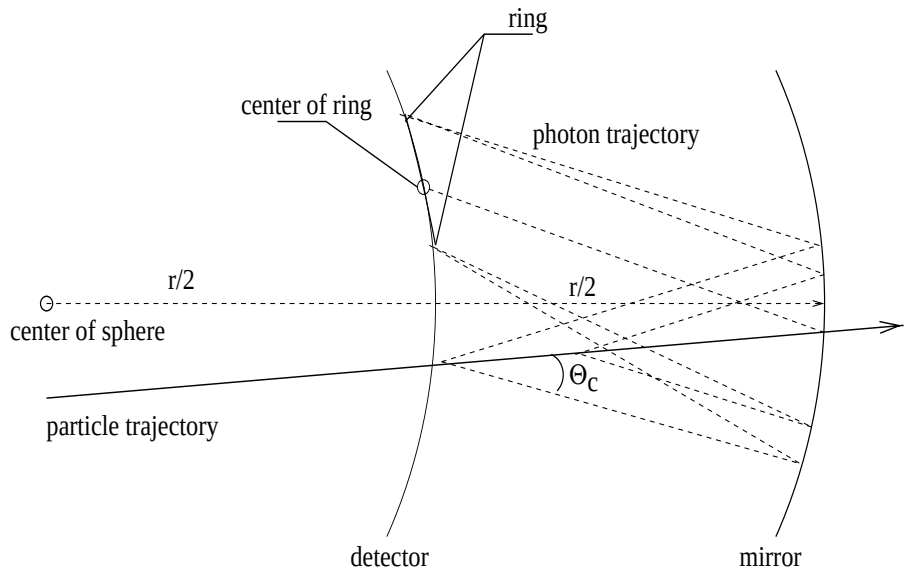

Figure 20: Display of a Cherenkov light path in the RICH

expected background is calculated for every track separately counting hits in a band outside the radius for a β=1 particle(*i.e.* particles which can not produce a ring). This method is used because it automatically takes into account overlapping rings. Figure 21 shows the single event display which demonstrates the low noise of the detector and its clear multi-track capability. Each ring corresponds to a maximum likelihood fit to the activated phototube. This event has identified a 600 GeV/c proton (track 17), a 152 GeV/c K^- (track 19), and a 74 GeV/c π^+(track 18). A cut is used on the ratio of the likelihood for different hypotheses to discriminate between different particles. For instance $\mathcal{L}(\mathcal{K})/\mathcal{L}(\pi)\geq 1$ is used for kaon, pion separations. The RICH can separate pions from kaons up to 165 GeV/c and kaons from protons up to 320 GeV/c. Figure 22 shows the expected ring radii at the photo detector and separation between different ring radii for various particle types as a function of momentum. A single-track resolution of σ_r=1.5 mm gives a $2\sigma_r$ $\pi - K$ separation of 165 GeV/c.

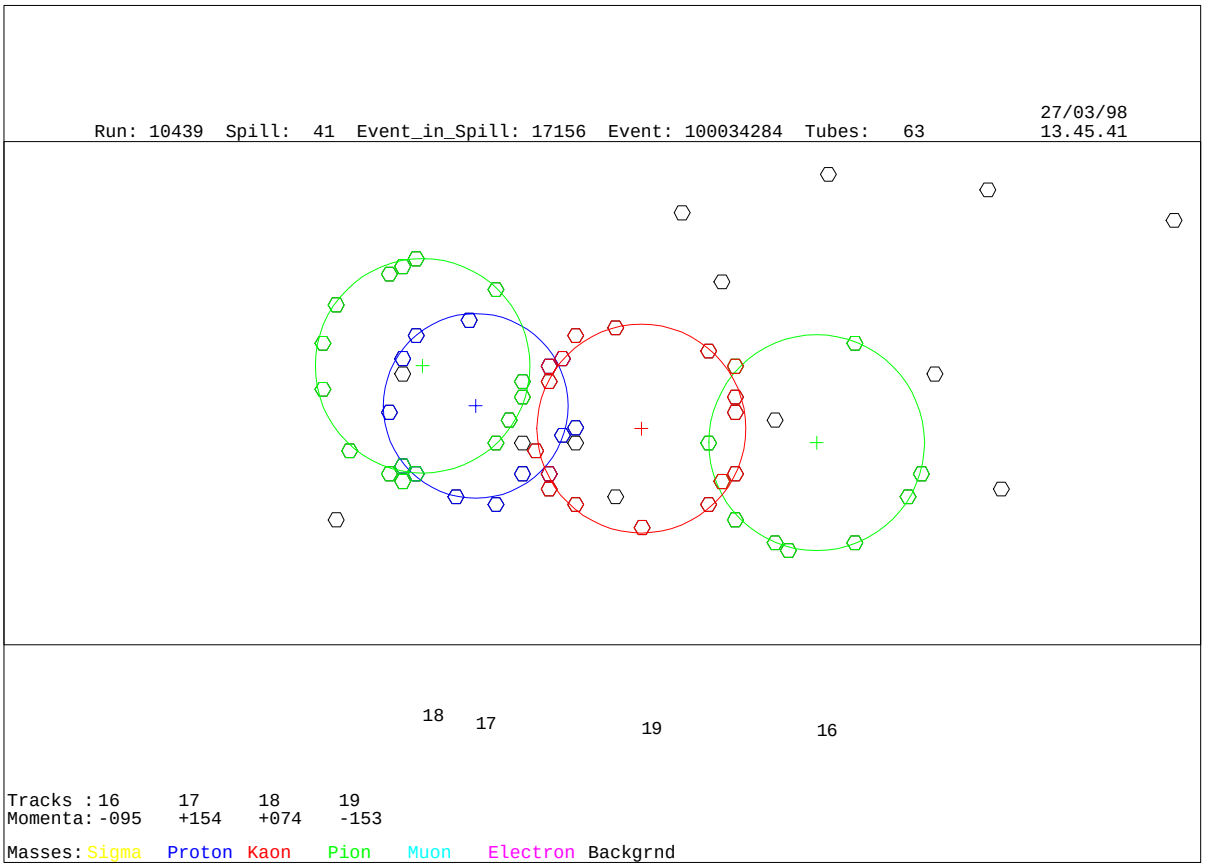

Figure 21: Single event Display

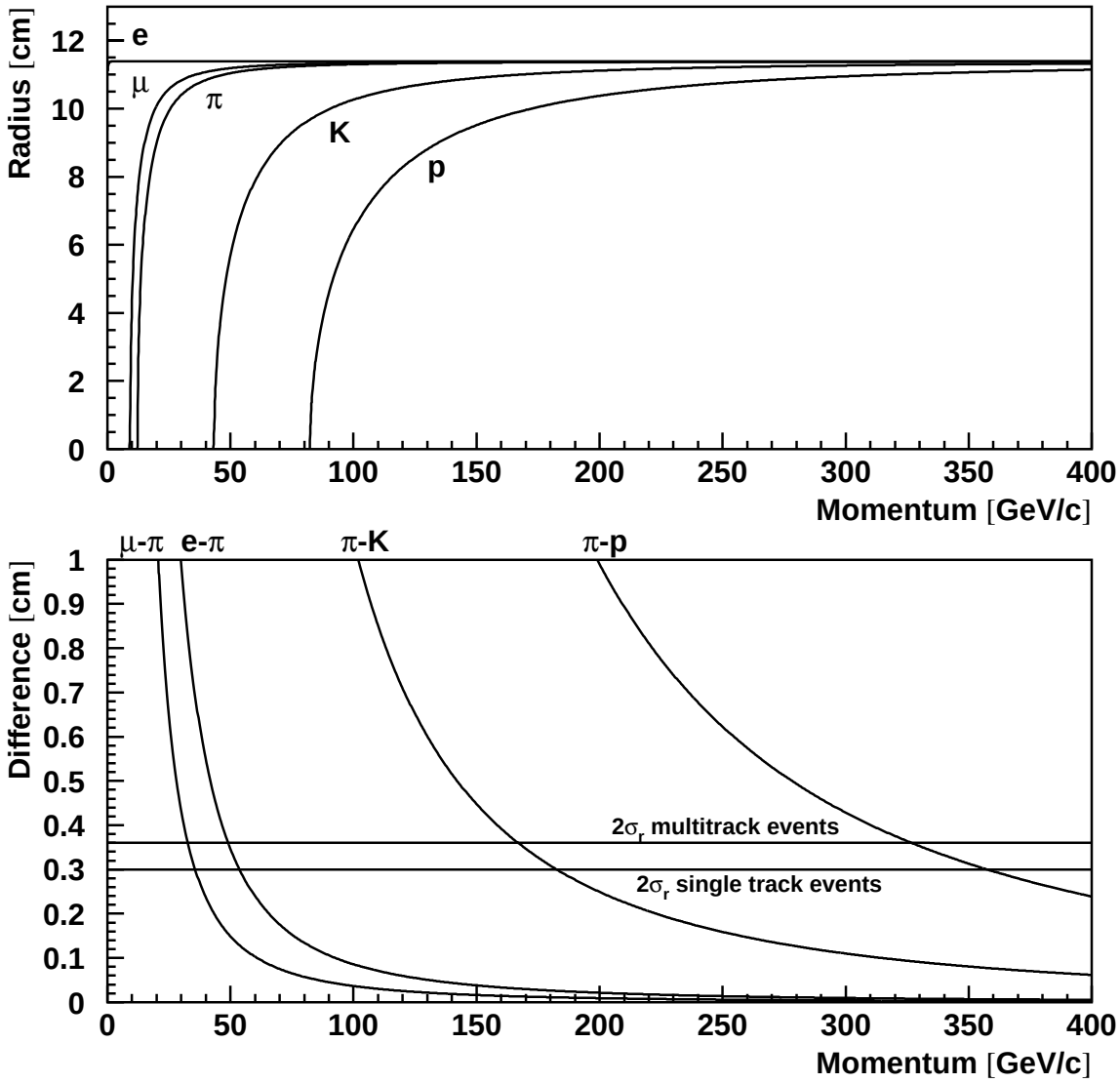

Figure 22: Ring Radius(top) and separation(bottom) vs momentum distributions for interaction data for tracks with 95-105 GeV/c momentums. The two horizontal lines on the lower plot show the achieved resolutions for single track and multitrack events, respectively

3.4.4 Detectors Involved in my Measurement

For this analysis partial of the detector systems is used. Negative(Σ^-, π^-) and positive(p, π^+) secondary beams are tagged by the BTRD. Silicon strip detectors are used to measure the beam and outgoing tracks, giving precision primary and secondary vertex reconstruction. Track momenta are measured after magnetic deflection by a system of PWCs, drift chambers and silicon strip detectors. The RICH detector is used for the particle identification. Kaons and pions are identified by the RICH for the D_s analysis. Hodoscopes are used for the trigger purpose. The remaining detectors, ETRDs, Lead class, Neutron Calorimeter, Vector Drift Chambers and M3MWPCs in Figure 6 are not used for this analysis.

CHAPTER IV
TRIGGER AND DATA ACQUISITION SYSTEM

The main goal of the SELEX is to study the production and decay of charmed baryons at high x_F. For this purpose SELEX implemented a "charm trigger" [24] which is set up to trigger on charm events while rejecting most of the non-charm background interactions. The charmed trigger has three levels of the hardware trigger, referred to as T_0, T_1 and T_2 and one level of software trigger. A schematic layout of the trigger is shown in Figure 23.

The first level trigger T_0 signals a valid incident beam particle and an interaction in the target (beam primitives) by using the Beam Scintillators and the Interaction Counters combined in the following trigger logic:

$T_0 = S_1 \cdot \overline{VH1} \cdot S_2 \cdot \overline{VH2} \cdot S_4 \cdot V_5$

The existence of T_0 signal starts T_1 decision circuits and provides a synchronization for the next stage. The T_0 stage reduces the gated beam trigger rate of 10^7/spill (500 kHz) to 1.5x10^6(75 kHz)

The second level trigger T_1 required a Beam TRD tag to select the beam type along with a T_0 output. It also used inputs from the interaction counters and H_1, H_2, and Primakoff hodoscopes. This trigger required more than 2 positive particles in the hodoscopes behind the second magnet(M2) which has an implicit momentum cut of 15 GeV/c. These hodoscopes, H_1 and H_2, determine the charged particle multiplicity.

The third level trigger T_2 is formed by a coincidence of T_0, and some signals from slower detectors like Vee Scintillators, Photon-III, and downstream TRD. At the

normal operation conditions T_2 is $T_1 - T_0$ coincidence, with a typical rate of 80,000 events/spill (4 kHz). A valid T_2 trigger sends a signal to the Data Acquisition system(DAQ) to start reading out the detectors . When the data readout process is complete, trigger levels are released in inverse order. Each level performs its own event processing termination and when finished sends a reset to the previous level until the level one trigger is released and the system becomes ready for the next event. In the case of a negative result at any level, it does not trigger the next level but just performs a system wide reset and releases previous levels.

The fourth level trigger is the software trigger which is an online computational filter based on downstream tracking and particle identification information. The software trigger selects events that made a full vertex reconstruction of the beam track and all tracks in the M2 spectrometer(high momentum tracks) to test the hypothesis that they all came from a single primary vertex. This trigger reduces the data size by a factor of nearly 8.

The charm trigger is also called impact parameter trigger: The perpendicular distance from a target(primary vertex) to the point-back of the track, called the impact parameter or miss distance, is required to be larger than 20μm for at least two high momentum tracks. These are taken as indicative of a secondary vertex necessary for charm. This keeps the non-charm background trigger rate below 1%.

4.1 Trigger Level Synchronization

The interlevel synchronization ($T_0/T_1, T_1/T_2, T_2/DAQ$) was performed by gate and delay generator units. Each gate and delay generator started with a previous level decision and maintained a busy output until the current event processing was finished. In the case of a negative decision the gate and delay generator terminated

the Busy signal and reset the previous level. In the case of a positive decision, each level of trigger latched and, after a delay fired the next level until the event was read by the DAQ.

4.2 Data Acquisition System

The Data acquisition system(DAQ) (Figure 23) is part of the DART project [25] developed by the collaboration of 6 experiments(E781, E811, E815, E831, KteV, and E835) and FNAL On-line Systems(OLS) group. The beam is delivered to the experiment during a 20 second spill(cycle time is 60 seconds). During this time 100-140K events (average event size $\approx$ 5KByte) are accumulated and stored in VME dual ported memories. The stored data are written to 8mm Exabyte tapes. Then these tapes are transferred in the Fermilab Mass Storage System(FMSS) where they can be retrieved over the network for further processing.

There are 10 parallel streams to readout different detector systems. Fastbus SVX Data Accumulators (FSDA) are used for the silicon microstrip detectors, Fastbus TDCs for the Drift chambers and Fastbus ADCs for the photon detectors and Neutron Calorimeter(NCAL). All the Fastbus crates were controlled via Fastbus Smart Crate Controllers (FSCCs) The Chamber Readout System(CROS) is used for the proportional wire chambers(M2PWCs) TRDs and RICH. The Receiver Memory Hybrid(RMH) system is used for the proportional wire chambers(M1 and M3PWCs). A CAMAC system is used for the scalars and latches.

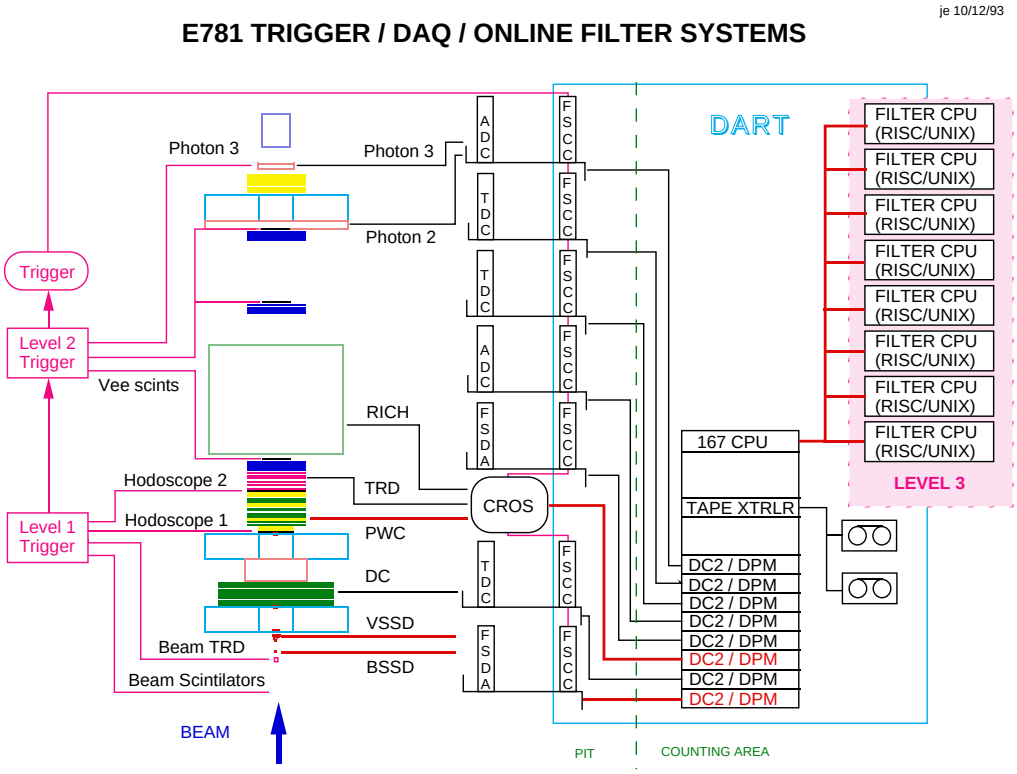

Figure 23: Schematic view of SELEX Trigger Logic and Data Acquisition system

CHAPTER V
DATA ANALYSIS

The purpose of this study is to compare the corrected yields for the charge conjugate pair: D_s^+ and D_s^-. Three-body decays are considered for this analysis, $D_s \rightarrow KK\pi$. In the SELEX experiment, the raw data were collected and stored on 8 mm tapes and placed in the Fermilab Mass Storage System (FMSS). SELEX took a total of 15.2 billion interactions and a total of 1 billion of them were processed and written to the tapes. Percentages of data distribution is displayed on the following Figure 24 for different beam types.

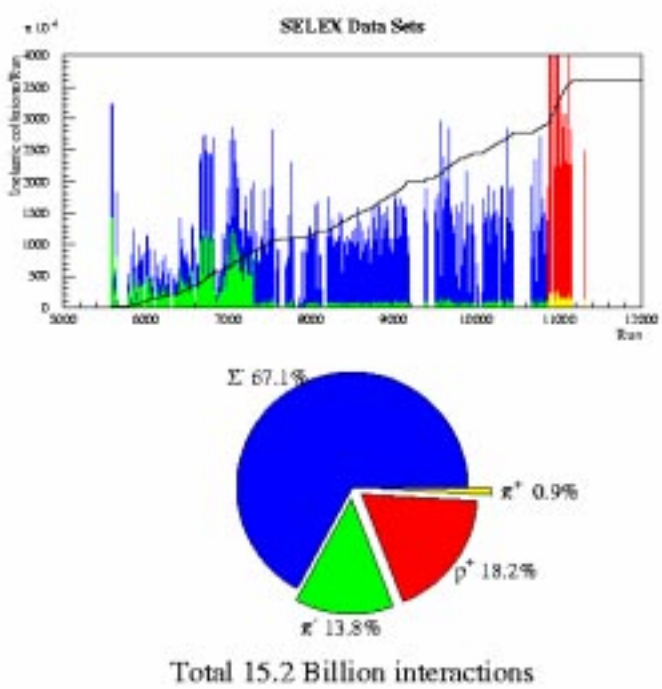

Figure 24: Upper graph shows the data taken with different beams at different runs (x axis run numbers) Lower picture is a percentage of different beams

The SELEX Off-line Analysis Program (SOAP) was used to process the raw data. The SOAP includes several programs: unpacker (UNPACK), track finder (TRACK), vertex finder (VERTEX), particle id (PID), and reconstruction (RECON). The individual programs are controlled by a user defined file. A sample control file can be seen in Table 3.

The unpacker decodes the raw data into a format that can be used by further programs. After unpacking the raw data, the track finding program looks for the tracks. Basically it looks for track segments in each spectrometer and these segments are combined to form a track. Tracking is controlled by a "TSEG" (track segment) file, a sample of TSEG file is shown in Table 4.

The vertex finder package looks for interaction and decay vertices. Particle id (PID) is activated after finding the tracks and vertices. After PID, all the information about tracking, vertex finding, etc. is stored in a table to be used by RECON. RECON is a reconstruction package, which uses the results from TRACK, VERTEX, and PID to reconstruct the event. The output of the RECON is written out in the form of ftuple (file ntuple). The ftuples consist of a set of physical quantities, such as momenta, energies, particle identities, and so on, for each event. The RECON package is also controlled by a RECON file that specifies the form of the reconstruction. This file contains PID cuts and some constraints on the reconstruction. A sample RECON file is shown in Table 5.

The ftuples are converted into the ntuple form that can be read by Physics Analysis Workstation (PAW). PAW is an interactive utility for visualizing experimental data on a computer graphic display. PAW combines various CERN High Energy Physics Library programs. Ntuples are read and manipulated directly from

Table 3: A sample control file for SOAP

```
! PASS11

noexec   filter
set  on  driver    wrt_savebk save_all
execute  unpack
set  on  unpack    adc cros rmh svx ! hist
execute  tracking
set  on  tracking  segment link fit0 silmatch silm3d guided fit ! hist
set  on  tracking  vx_radial m1_guide
set  cut tracking  lasd_wid       2.   ! inflate LASD res by factor 2
set  cut tracking  max_bmsi     250.
set  cut tracking  max_vxsi    1000.
set  cut tracking  max_pwc      260.
set  cut tracking  max_svx     1000.
set  cut tracking  segment    0   ! all spectrometers on in track_segment
set  cut tracking  ptm1       0.7279   ! use fixed spectrometer pt_kicks
set  cut tracking  ptm2       0.8391   ! use fixed spectrometer pt_kicks
prog     tracking  pass11.tseg

ocs  class main anal
ocs  sets out ncal_ vdc_

exec     photon
set  on  photon    full m1_pht m2_pht m3_pht
set  cut photon    min_count  5.
set  cut photon    min_energy 2.

exec     partid
set  on  partid rich btr etr etr_track  ! etr_hist

execute  user
set  cut user   report        1000

exec     vertex
set  on  vertex vtx2   err2 secint   prim  sec
set  cut vertex prong            5
set  cut vertex vtxd           4.0

exec     recon
set  on  recon  hist  ntuple ! ftuple  strip
set  cut recon  tgt_rec       0.05
set  cut recon  pscale        1.0020
set  cut recon  cand_csec     5.0
set  cut recon  cand_cpri     5.0

exec mcmatch
set on mcmatch embed smear mctseg match

disk embed /anal01/production/ds/embed/sigma/hbook/ds_kki+.dat
disk in  reset
! in   disk_files
disk in /spool8/data/unspooled/charm/charm_run010783_001
disk in /spool8/data/unspooled/charm/charm_run010783_003
disk in /spool8/data/unspooled/charm/charm_run010783_005
disk in /spool8/data/unspooled/charm/charm_run010783_007
disk in /spool8/data/unspooled/charm/charm_run010783_009
ana 100000
exit
```

Table 4: Sample TSEG file

```
comb: bm_comb1
planelist:  bm_ssd_ 1x1y1u2x2y3x3y3u
planeinit:  bm_ssd_1y bm_ssd_3y bm_ssd_1x bm_ssd_3u
!     cut names   xl   xh   txl   txh   yl  yh   tyl   tyh  xs  ytgt  chi2
npl
cuts:       0.,  0.,-.0012,.0012, 0., 0.,-.0012,.0012,0.0, 0.2, 4.0,  7
*end

comb: vx_comb1
planelist:  vx_ssd_ 1x1y1u1v2x2y2u2v
planelist:  vx_msd_ 1x1y1u1v2x2y2u2v3x3u3v4x
planeinit:  vx_ssd_1u vx_ssd_1v vx_msd_2x vx_msd_2y
!cut names   xl   xh   txl   txh   yl  yh   tyl   tyh   xs  ytgt chi2 npl
cuts:       0.,  0.,-.025, .025,  0., 0.,-.025, .025,    ,    , 5.0, 12
*end

comb: m1_sp1+
planelist:  m1_pwc_ 1x1y2x2y3x3y
planelist:  m1_pwc_ 1u1v2u2v3u3v      3
planelist:  m1_dsd_ 1x1y2x2y
planelist:  m1_ssd_ 1v2u              1
planeinit:  m1_dsd_2y m1_pwc_3y m1_dsd_1x m1_pwc_3x
!cut names   xl  xh   txl  txh  yl  yh  tyl   tyh  xs  ytgt chi2  npl nhit
cuts:       0., 0., .001, .1,  0., 0., -.05, .05,  0., 1.,  2.0, 13, 450
*end
comb: m2_forceuv3
planeinit:  m2_pwc_1y m2_pwc_6y m2_pwc_1x m2_pwc_6x
*end

comb: m2_3-3uv5uv
planeinit:  m2_pwc_3u m2_pwc_3v m2_pwc_4x m2_pwc_5v
!     cut names   xl    xh   yl      chi2
cuts:      -0,   0.,,,0.,,,,0.,0.,,,150
*end
!
comb: m3_comb1
planelist:  m3_pwc_ 1v1y1x1u2y2x3x3v
planeinit:  m3_pwc_1v m3_pwc_1y m3_pwc_2y m3_pwc_3x
!cut names   xl    xh   txl   txh    yl    yh   tyl   tyh  chi2   npl
cuts:       0.,   0., -0.5,  0.5,   0.,   0.,-0.05, 0.05,,,2.0,    6
*end

link   prog bmdown
link   copy bm                       ! convert beam tseg into track

link   prog m2down
link   add  m2 to m1  10.0           ! add  M2 segments
link   add  m2 to vx   5.0
link   copy m2                       ! copy M2 segments
! tracking program
tracking  findcl     all             ! clusterize all planes
tracking  fbk_guide                  ! find tracks in filter block
tracking  segment    bmm2            ! find segments in all spects but vx
tracking  link       bmdown          ! prepare bm Tsegs for silmatch
tracking  guided     bm>vx_comb1     ! find old beam tracks in vx
!
```

Table 5: Sample RECON file

```
#recdf 0 0 fill anal v02.01 nov 14 1999 15:00 !modified by(M.K.) ! pass11
recon list
! pass11 production - add x1 baryon modes by J. Russ
id  name       from pr q  pid   ls_min ls_max mass_min mass_max
out!   frac
! Strange states
1  kshort       v2  2  0  i-i+       5.  800.   0.470  0.530$100008!011.41
2  lambda       v2  2  0  p+i-       5.  800.   1.090  1.140$200008!020.33
3  alambda      v2  2  0  p-i+       5.  800.   1.090  1.140$200008!030.07
4  phi          c   2  0  k+k1-      0.    0.   0.995  1.045$400000!048.21
4  phi          c   2  0  k2+k-      0.    0.   0.995  1.045$400000!054.36!
52  i2i         v2  3 +1  i-i+i+     5.  800.   0.400  1.300$002002!1617.6
61  ki          v2  2  0  k-i+       5.  800.   0.600  1.700$002002!170.91
62  k-2i        v2  3 +1  k-i+i+     5.  800.   0.750  1.500$002002!180.20
!
! D0
100  d0_kpi      v2  2  0  k-i+       0.  800.   1.664 2.064$000041!240.19
101  d0b_kpi     v2  2  0  k+i-       0.  800.   1.664 2.064$000041!250.28
! D+
200  d+_k2pi     v2  3 +1  k-i+i+     3.  800.   1.769 1.969$000081!350.16
201  d-_k2pi     v2  3 -1  k+i-i-     3.  800.   1.769 1.969$000081!360.26
!
! D_s+
300  ds+_kkpi    v2  3 +1  k-k+i+     0.  800.   1.765 2.165$000101!470.35
301  ds-_kkpi    v2  3 -1  k-k+i-     0.  800.   1.765 2.165$000101!480.43
!
! Lambda_c+
400  lc+_pkpi    v2  3 +1  p+k-i+     0.  800.   2.085 2.485$000202!550.41
401  lc-_pkpi    v2  3 -1  p-k+i-     0.  800.   2.085 2.485$000202!560.38
!
! Cascade_c+
500  xc+_pkkpipi c   5 +1  p+k-k-i+i+ 0.  800.   2.300 2.800$001002!730.32
501  xc-_pkkpipi c   5 -1  p-k+k+i-i- 0.  800.   2.300 2.800$001002!740.37
! Exotic States
900  u_part      c   3 +1  p1-i+i+   -4.    4.   1.000 2.500$000000!938.28
901  u_part1     ar  3 +2  p2+u_part -4.    4.   1.000 2.500$010000!944.61
!                        meson    baryon    exotic    strange semilpttotal
!    recdf_19    [%]    b1=3.38  b2=4.96   b4=1.33   b8=3.40 b10=0.93!  13.99
!    recdf_20    [%]    b1=3.12  b2=4.20   b4=1.46   b8=3.41 b10=1.06!  13.25

#recpid     0     0 fill anal v01.21 07-May-1998 12:23 syj ! Particle idlist
! pass11 production - m1_kink pmin set to >3% decay prob in 5-12m region
! Efficiency test for one kaon in the rich 14 july 1999 M.K.
name system cut   pmin pmax mdistmin mdistmax ptmin ptmax spectro logic
e   etrd  e>0.5    0. 120.  0.       0.      0.    0.    m2  none! default electron
i   rich  i<0.1    0.   0.  0.       0.      0.    0.    any not! notnon-pi if in rich
k   rich  k/i>=1   0.   0.  0.       0.      0.    0.    m2  none! default Kaon
k4  rich  k/i>=0.01   0.   0.  0.     0.      0.    0.    m2  none! default Kaon
p   rich  p/i>=1   0.   0.  0.       0.      0.    0.    m2  none! default proton
e1  etrd  e>0.5    0. 120.  0.0020   0.0500  0.300 2.000 vxm2 none! non-pvtx electron
k1  none  none     0.   0.  0.       0.      0.    0.    any none! anytrack
k2  rich  k/i>=1   0.   0.  0.       0.      0.    0.    any not! anytrack not a K
p1  rich  p/i>2. 100. 600.  0.       0.      0.    0.    any     none !
p2  rich  p/i>2.   0.   0.  0.       0.      0.    0.    m1m2 none! lambda daughter proton
s   none  none    40. 600.  0.       0.      0.    0.    vxm1nm2 none! m1_kink
x   none  none    40. 600.  0.       0.      0.    0.    vxm1nm2 none! m1_kink
o   none  none   100. 600.  0.       0.      0.    0.    vxm1nm2 none! m1_kink
*end
```

PAW. PAW generates a KUMAC file to store the commands used in processing ntuples and histograms. A sample KUMAC file is shown in Table 6. More information about PAW can be found in the PAW manual [26].

While converting from ftuple to ntuple, several selection criteria are imposed.

5.1 Event Selection Criteria

It is necessary to adopt selection criteria in the form of a set of cuts. The cuts are selected so as to reject as many background events as possible without loosing too much signal. Event selection is started by requiring three-prong decay vertices with a total charge of ± 1 and 2 kaons in the RICH. The specific values of the cuts are identical for the charge conjugate modes. These cuts are the following:

i) l/σ cut: This quantity determines the distance between primary and secondary vertices in terms of the errors associated with them. The primary vertex is the interaction point where a number of charged tracks converge inside the target. The secondary vertex is the point where a charm particle is believed to decay. The secondary vertices are required to be located outside the target. If they are inside the target the event is rejected. The longitudinal separation between the primary and secondary vertices is required to be more than 9 times the combined error on the primary and the secondary vertices ($\frac{l}{\sigma} > 9$ and $\sigma^2 = \sigma_p^2 + \sigma_s^2$ where σ_p and σ_s are the errors on the primary and secondary vertices, respectively). A cartoon configuration of longitudinal separation between primary and secondary vertices and associated errors are shown in Figure 25. Figure 26a shows a l/σ cut distribution at the signal region after applying the cut.

ii) *pvtx* cut(Figure 26b): The impact parameter of the reconstructed momentum vector of a D_s candidate with respect to the primary vertex is required to be less

Table 6: Sample KUMAC file

```
opt date;set fit 1111;opt fit;set fcol 4;set ysiz 15.0
set xsiz 15.0;set *fon -60;set hcol 1001;set bwid 4;set bcol 2.5;
igset mtyp 2;set htyp -3;igset chhe .35;igset fais 2

***
for/file 24 mass4tez.ps
meta 24 -111
***

title '  Preliminary Results of D?s! Mass Distribution CHARM2 ntu. sample'

exec charm2

nt/cut $1 id=300     !DS+
nt/cut $2 id=301     !DS-
nt/cut $3 scut.for>=9.
nt/cut $4 pvtx<8.
nt/cut $5 sigma<.17
nt/cut $6 svx_z<3.5
nt/cut $7 tgt>=6.and.tgt<=10
nt/cut $8 btk_pid=9.and.btk_type<0.                  !Sigma beam
nt/cut $9 l/sigma>9
nt/cut $24 $4.and.$8.and.$9

1d 10 'D?s! sample  ' 80 1.77 1.965
nt/proj 10 111.mass $4.and.$9

1d 40 'D?s^-! sample  ' 80 1.765 2.165
nt/proj 40 111.mass $24.and.$2
1d 41 'D?s^+! sample  ' 80 1.765 2.165
nt/proj 41 111.mass $24.and.$1

zone 2 2
*max 40 175
*max 41 175

ve/cre p0(9) r  137. 1.872 0.008 530. 1.969 0.008 40. 0 0
ve/cre p1(9) r  110. 1.869 0.008 226. 1.970 0.008 47. 0 0

exec hifit2 40 dgauss.for ! 9 p0
atit 'Mass (GeV)' 'Events/5MeV'
hi/pl 40 * s
exec hifit2 41 dgauss.for ! 9 p1
atit 'Mass (GeV)' 'Events/5MeV'
hi/pl 41 * s
zone
exec hifit2 10 dgauss.for ! 9 p1
atit 'Mass (GeV)' 'Events/5MeV'
VE/DEL P1
CLOSE 0
HI/DEL 0
***$
```

Table 7: Default cuts

Cuts	l/σ	$pvtx$	$scut$	Svx_z	$Sigma$	tgt
Default	>8.	<12.	>=9	<3.5 cm	<.17 cm	all targets in

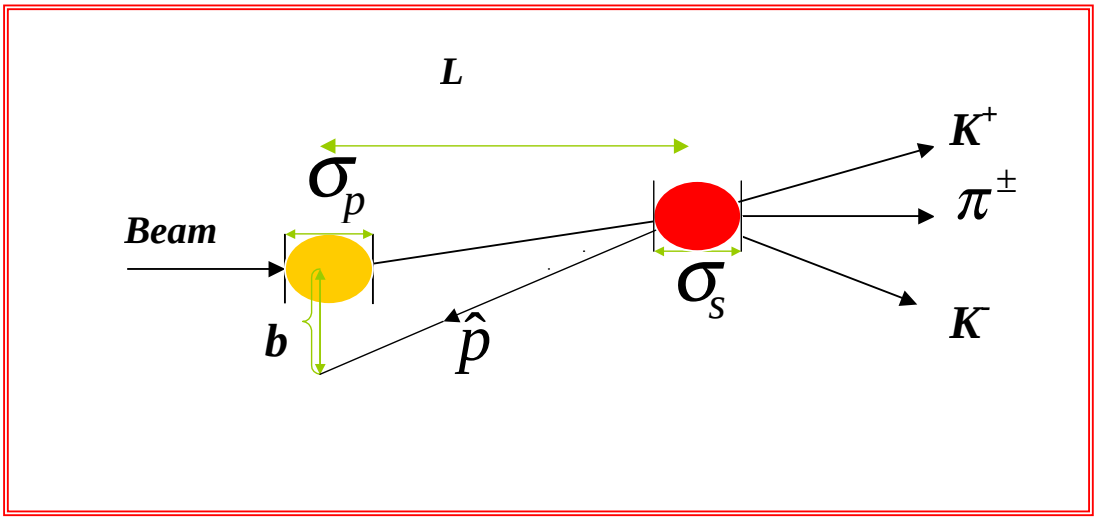

Figure 25: Primary and secondary vertices and errors associated with them

than 8σ. In other words, a charm track should project back to the primary vertex, with a pointback parameter ($pvtx$), $(\frac{b^2}{\sigma_b^2})$<8, where b is the impact parameter which is shown in Figure 25. Since the charm particle is produced in the primary vertex in the signal region this cut is expected to be very small. These two cuts defined are especially useful against combinatorial background.

iii) $scut$: Two tracks should miss the primary vertex by 3 sigma ($scut \geq 9$). $scut$ cut distributions are shown in Figure 26c.

iv) svx_z: z distance of secondary vertex from the edge of the last target should

be less than 3.5 cm($svx_z < 3.5cm$). This cut requires the secondary vertex to be outside of the vertex detectors, since vertex detectors are located 3.5 cm away from the edge of the last target. svx_z cut distributions are shown in Figure 26d.

v) $SIGMA$(Figure 26e): ($\sigma = \sqrt{{\sigma_p}^2 + {\sigma_s}^2}$) should be less than 0.17 cm.

vi) tgt: 2 Copper (Cu) and 3 diamond(C) targets have been used for this analysis. Target cut distributions are shown in Figure 26f.

Vii) Probability cut: This cut requires the probability of the first two tracks to be kaon tracks to be more than 70 %. This cut selects for the real phi data events. It reduced the signal by 35% and the background by a factor of 10 without changing the momentum spectrum. Figure 27 and 28 show the phi mass and momentum spectrum before and after the probability cut respectively. This cut is used for the $KK\pi$ events; it reduced the signal by 17% and the background by a factor of 2.

5.1.1 Statistical Significance

These sets of cuts are chosen to reject as many background events as possible without loosing signal events. A good selection criterium should give us the best statistical significance which is the best signal/error ratio.

The statistical error associated with the number of signal events is given by the possibility of signal and background fluctuation. This can be obtained by the square root of the sum of signal and background(under the signal) events(assuming a poisson distribution). Thus the best set of cuts is the one which maximizes the following relation:

$$Significance = \frac{N_s}{\sqrt{N_s + N_b}},$$

where N_s is the number of simulated events in the signal region and N_b is the number

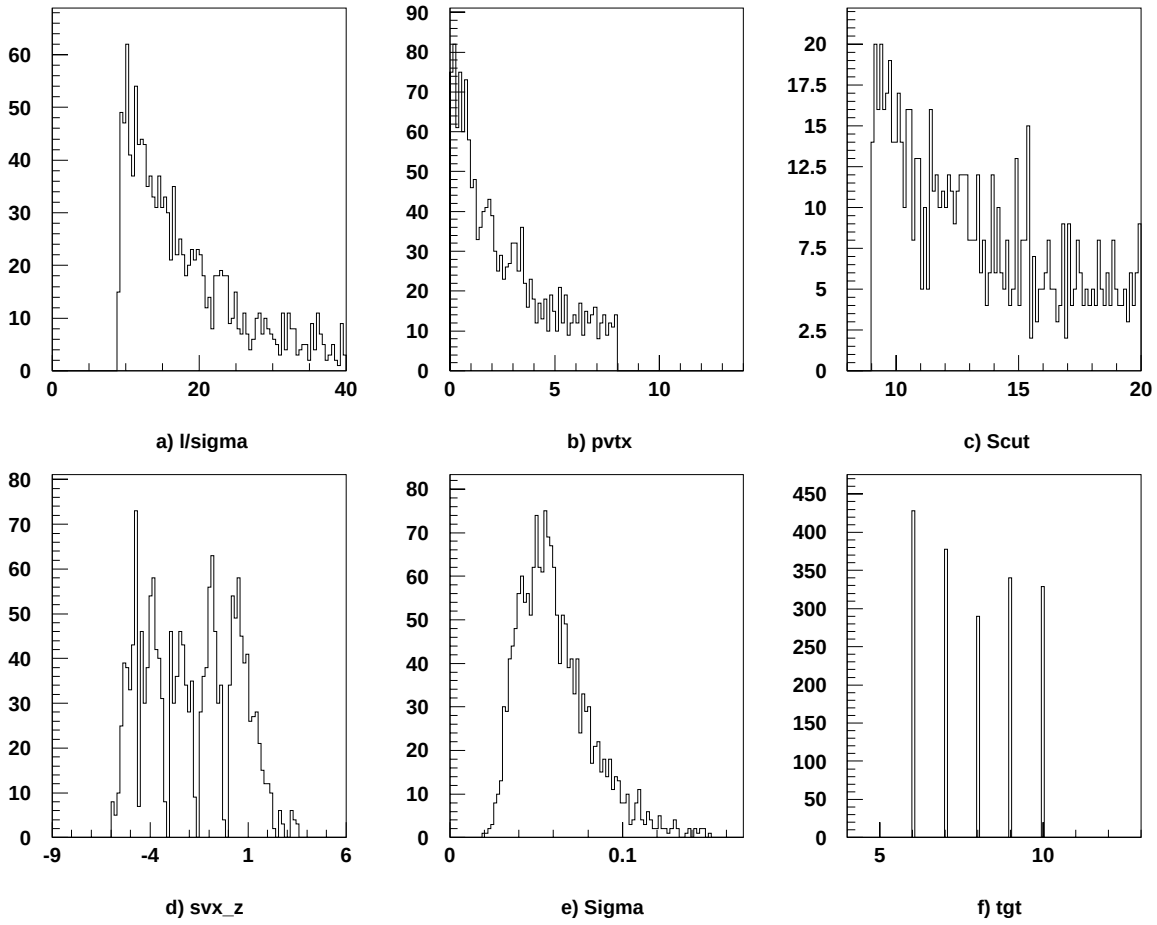

Figure 26: Selected optimized cuts

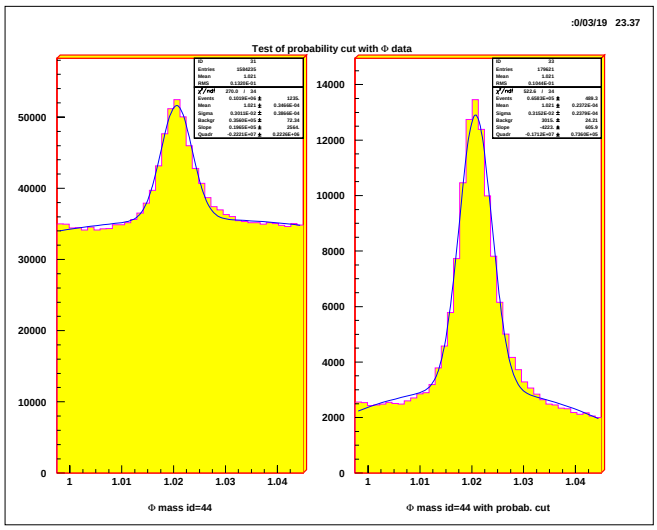

Figure 27: ϕ Mass Spectrum before and after the probability cut

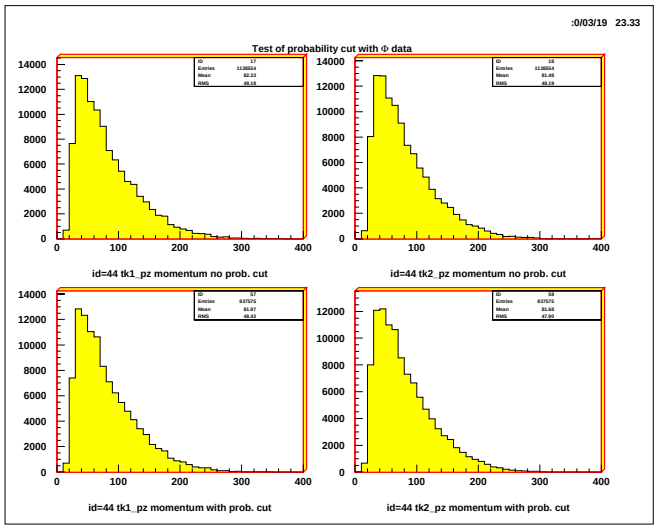

Figure 28: Momentum Spectrum of the first and second kaon of the ϕ before and after the probability cut

Table 8: Optimized cuts

Cuts	l/σ	$pvtx$	$scut$	Svx_z	$Sigma$	tgt
Optimized	>9	<8	>=9	<3.5 cm	<0.17 cm	all targets in

of events in the sideband region. Since we don't know how to separate signal and background we need to simulate the signal events to evaluate statistical significance.

For the medium and low statistics channels, the number of events in the signal region is small. In these cases it is difficult to perform an optimization of the cuts since possible fluctuations can change the results. So another optimization method is used for medium and low statistics channels. Simulated events are used for the signal region and data for the background under the signal or on the sideband region in order to maximize the statistical significance.

The cuts l/σ, $pvtx$, svx_z, $Sigma$, $scut$, and probability cut are optimized starting with the loose cuts like l/σ >8, $pvtx$ <5, svx_z <1, $Sigma$ <.1, $scut$ >9 and probability cut$(mod(tk1_pid/100, 10) > 1.and.mod(tk2_pid/100, 10) > 1$. These cuts are varied one by one always keeping the others fixed until the significance maximized for that particular cut. For example l/σ is varied while keeping the others at the same value. For each l/σ value the statistical significance is obtained using the above equation. This technique is repeated for the other cuts as well. The resulting curves are shown in Figure 29. Some of the cuts are not be able to maximized they reached the plateau, which was taken as an optimized value.

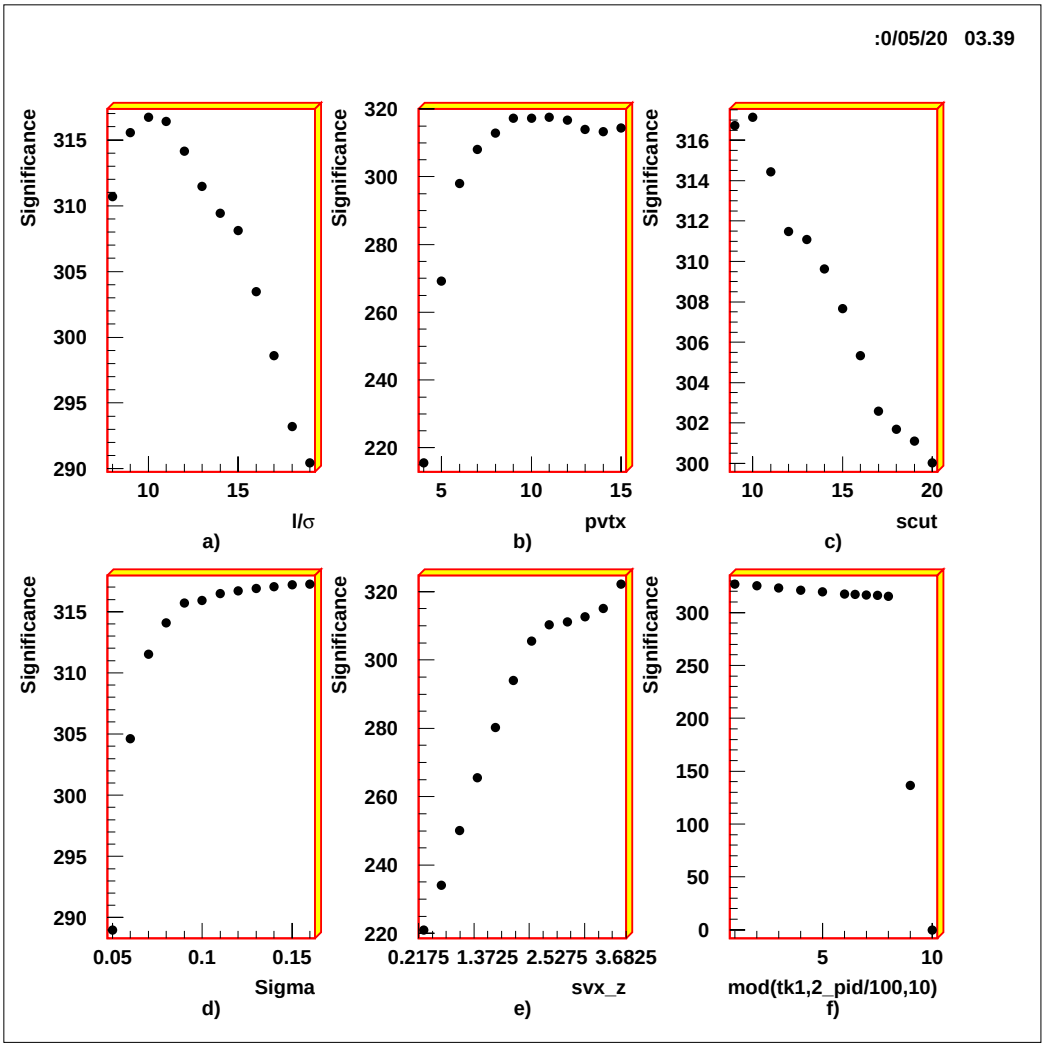

Figure 29: Statistical Significance

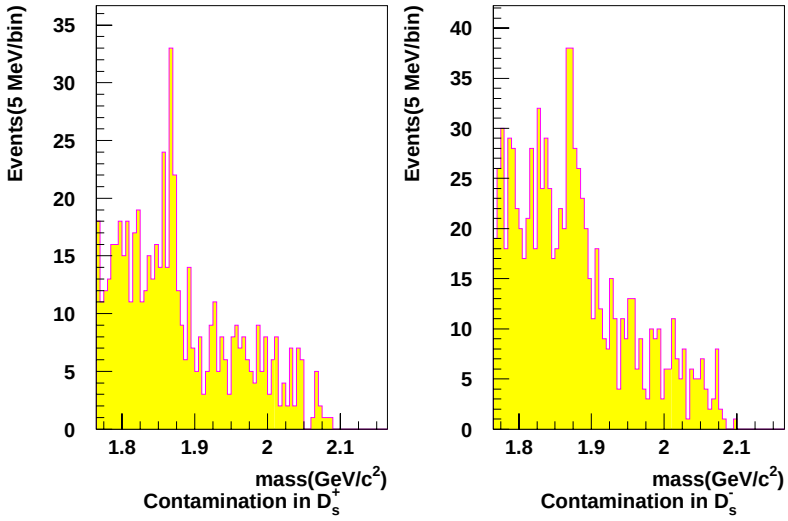

Figure 30: $K\pi\pi$ and $\pi K\pi$ Contamination

5.1.2 Contamination

Since the Ring Imaging Cherenkov detector is not perfect, it is possible to misidentify a pion as a kaon. We take the full $KK\pi$ sample(including contamination) and fit it to the $K\pi\pi$ hypothesis. A peak appears in the D meson region, as in Figure 30. This peak definitely shows some contamination due to misidentified kaons. This enhancement comes from those events in which a pion had been misidentified as a kaon in the $KK\pi$ spectrum. The number of $K\pi\pi$ events is estimated to be less than 7% of the total yield.

Since the contamination is small, it is left in the sample and the effects calculated as a systematic error, which is discussed later. Moreover, D^- and D^+ are both nonleading particles for the Σ^- beam, i.e. both are produced symmetrically, so their small contamination will not effect the production asymmetries between D_s^- and D_s^+.

5.2 Data Simulation

An Embedding simulator is used for this analysis. Event embedding is a package, which is incorporated with SOAP. It generates simulated signal events in the SELEX apparatus, which are then embedded into the raw data. The event generator used is the QQ package, which was produced and improved by the CLEO collaboration [27]. The QQ package consists of two parts: production and decay. In the production part, production parameters are specified in the input file that is shown in Table 9. Decays are specified in the decay.dec file that is shown in Table 10. A sample output file of the control file is given in Table 11.

The embedding package starts reading an event from the event generator. The generated events contain all the information about the coordinate system; angles between the track and z axis in the x or y plane, interaction point which the tracks originate, mass or particle id defined by SOAP, and total momentum, p, of the tracks. On the other hand the beam direction and primary vertex information were obtained from real data.

In the sample output file, the first three columns describe the x, y, z position of the particle, the next three columns are the directional cosines at the x, y, z position, and the following columns are the total momentum p and the mass of the particle.

Table 9: QQ Sample INPUT file

```
nevent          100000
decay_id        431    !Ds+
!decay_id        -431    !Ds-
beam_id         3112    !sigma beam
!beam_id                -211    !pion(-) beam
beam_momentum   600.0    !Sigma(-) or pion(-)
mean_pt         0.8
xf_power        0.0   !(1-x)^n n=0 flat distribution
data_out       datahbook/ds_kki+.dat
hist_out       datahbook/ds_kki+.hbook
decay_file      ds_kki+.dec
```

Table 10: QQ Sample DECAY file

```
*****for D_s-->KKPI*******
DECAY  DS-
CHANNEL 0 1.000 K+ K- PI-
ENDDECAY
*****for D_s-->PHIPI******
DECAY  DS-
CHANNEL 0 1.0000 PHI PI-
ENDDECAY
DECAY PHI
CHANNEL 0 1.0000 K-K+
ENDDECAY
```

Table 11: Sample of EMBEDDING output file.

```
3 +1 -1 +1          0          0          0
-0.0001  0.0010   1.010 -0.002555 -0.003828  0.999989   47.55   0.494
-0.0001  0.0010   1.010 -0.003469  0.012689  0.999913   55.08   0.494
-0.0001  0.0010   1.010  0.011494 -0.015158  0.999819   25.99   0.140
-0.0028 -0.0018   4.713 -0.002755 -0.004356  0.999987   95.54   0.494
-0.0028 -0.0018   4.713  0.000924  0.000742  0.999999  319.98   0.497
-0.0028 -0.0018   4.713 -0.002787 -0.000175  0.999996  124.87   0.141
-0.0160 -0.0043   1.183 -0.018990  0.009677  0.999773   26.75   0.494
-0.0160 -0.0043   1.183 -0.011130 -0.022743  0.999679   38.28   0.494
-0.0160 -0.0043   1.183 -0.011617  0.008769  0.999894   30.34   0.139
 0.0001  0.0002   0.157 -0.002021  0.005634  0.999982   88.18   0.493
 0.0001  0.0002   0.157  0.003331 -0.000649  0.999994  194.85   0.492
 0.0001  0.0002   0.157 -0.004191  0.001270  0.999990   83.03   0.139
-0.0004 -0.0002   0.076 -0.003383 -0.015537  0.999874   38.71   0.494
-0.0004 -0.0002   0.076 -0.013724 -0.003145  0.999901   33.09   0.494
-0.0004 -0.0002   0.076 -0.001951  0.007273  0.999972   59.86   0.142
 0.0000 -0.0009   0.146 -0.006460  0.020964  0.999759   18.74   0.494
 0.0000 -0.0009   0.146 -0.016750 -0.024991  0.999547   21.37   0.494
 0.0000 -0.0009   0.146  0.036535 -0.014254  0.999231   13.27   0.140
 0.0000  0.0001   1.311  0.000670  0.003571  0.999993   54.62   0.494
 0.0000  0.0001   1.311  0.003647  0.002708  0.999990   78.70   0.494
 0.0000  0.0001   1.311 -0.001459 -0.001828  0.999997  213.80   0.142
```

5.3 Acceptance

The embedded simulation events method is used to find the reconstruction efficiency. The combined acceptance (geometrical acceptance and reconstruction efficiency) for the D_s decay modes is estimated by generating a large number of events with a flat distribution in Feynman-X parameter between 0.0-1.0 with 100% decay

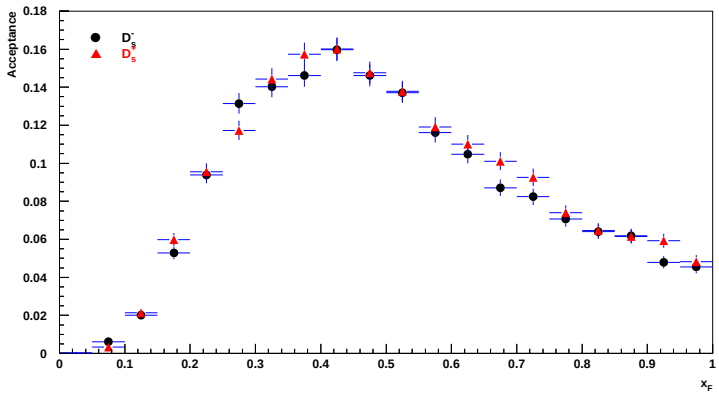

Figure 31: Reconstruction efficiency for $D_s^{\pm}$ vs x_F

to $KK\pi$ mode, 600 GeV/c beam momentum, and p_t^2=0.4. The embedded event was reconstructed and the reconstruction efficiency was measured using the ratio of the reconstructed events to the generated events.

$$\epsilon_{rec}(D_s^{\pm} \rightarrow K^+K^-\pi^{\pm}) = \frac{N_{rec}(D_s^{\pm} \rightarrow K^+K^-\pi^{\pm})}{N_{gen}(D_s^{\pm} \rightarrow K^+K^-\pi^{\pm})}$$

The reconstruction efficiency over the x_F range of 0.0 - 1.0 is given in Figure 31. The subset of values that is used to correct the data over x_F range 0.15 - 0.6 and their ratios as a function of x_F for $D_s^{\pm} \rightarrow K^+K^-\pi^{\pm}$ is shown in Figures 32 and 33 respectively. The reconstruction efficiency of $D_s^{\pm} \rightarrow K^*K^{\pm}(\phi\pi^{\pm})$ is the same within the error. As can can be seen from Figure 32 both efficiencies are about the same, the difference has been estimated less than 4% between D_s^- and D_s^+ . This result shows that SELEX apparatus is not charge dependent.

Figure 34 and 35 show reconstruction efficiency of D_s^- and D_s^+ and their ratios as a function of p_t^2 respectively. These figures show that SELEX acceptance does not

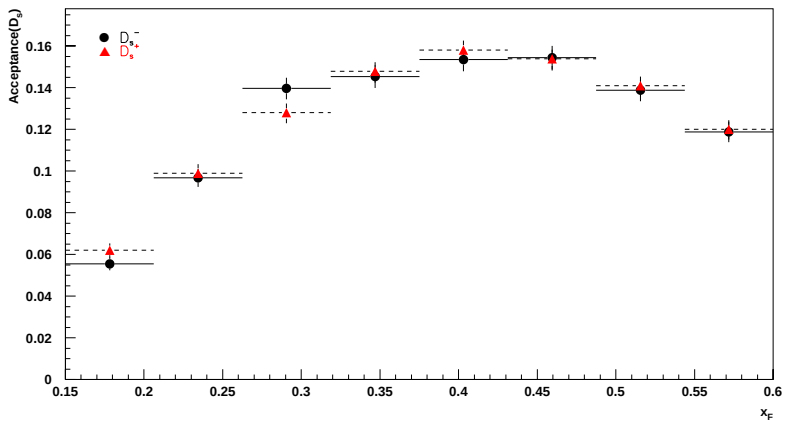

Figure 32: Reconstruction efficiency for $D_s^{\pm}$ from 0.15 to 0.6 x_F. This region is used to correct the raw data

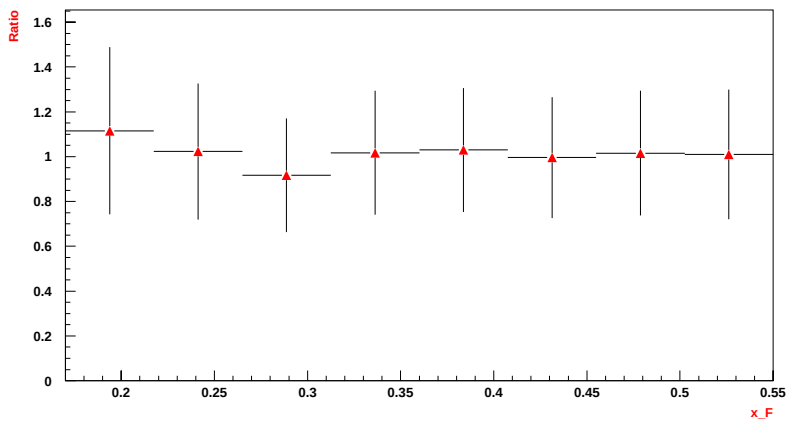

Figure 33: Ratio of reconstruction efficiency between D_s^- and D_s^+ from 0.15 to 0.6 x_F

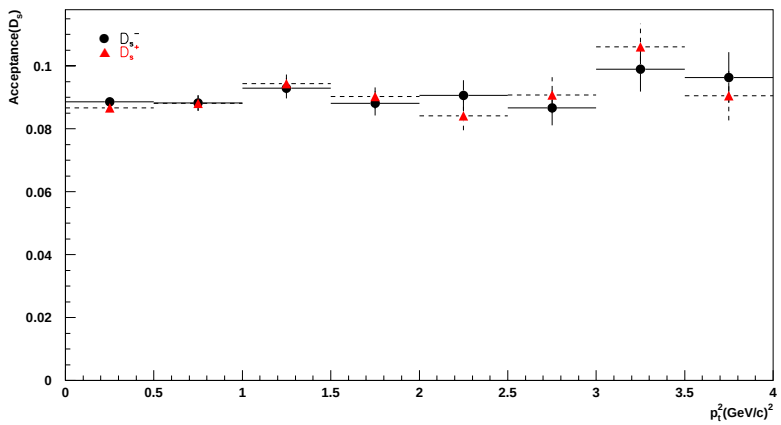

Figure 34: Reconstruction efficiency for D_s^- and D_s^+ mesons as a function of p_t^2

strongly depend on the p_t^2.

5.4 D_s Yields: Peak Fitting Method

Three body decay modes require consideration of the particle identification capability and branching ratios. As noted earlier SELEX uses the RICH detector to identify kaons, pions and protons. The RICH has a capability of separating K from the π up to 165 GeV/c. The most abundant D_s channel is D_s decaying to three charged particles: $D_s^+ \rightarrow K^+K^-\pi^+$. The resonant channels $D_s^+ \rightarrow \phi\pi^+$ and $D_s^+ \rightarrow K^+\bar{K}^*(892)^0$ are also considered. The branching ratios of these channels are [28]:

$$BR(D_s^+ \rightarrow K^+K^-\pi^+) = (4.4 \pm 1.2)\%$$

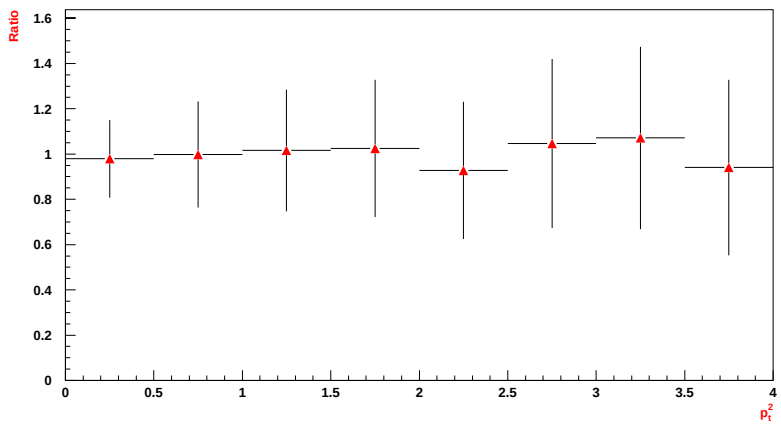

Figure 35: Ratio of reconstruction efficiency between D_s^- and D_s^+ measons as a function of p_t^2

$BR(\mathrm{D}_s^+ \to \phi\pi^+) = (3.6 \pm 0.9)\%$

$BR(\mathrm{D}_s^+ \to K^+\bar{K}^*(892)^0) = (3.4 \pm 0.9)\%$

Selection of the $K^-K^+\pi^\pm$ channel starts with the combination of two well-reconstructed oppositely charged tracks that are identified as kaons by the RICH and a third track which is assumed to be a pion. The invariant mass for the combination of these three tracks, assumed to be $KK\pi$, is within a mass window region of 1.765-2.165 GeV/c^2, which includes both Cabibbo-suppressed $D^\pm \to KK\pi^\pm$ charm mesons and cabibbo-favored $D_s^\pm \to KK\pi^\pm$ charm strange mesons.

The combined $D_s^\pm$ mass plot for $K^-K^+\pi^\pm$ channel after all selection criteria are applied is shown in Figure 36. A two Gaussian with a quadratic background fit is applied to the combined spectrum. The fit yields 792±37 $D_s^\pm$ mesons with a mean value of 1969±0.5 MeV(PDG value[29]:1968.6±0.6) and 332±27 $D^\pm$ mesons with a

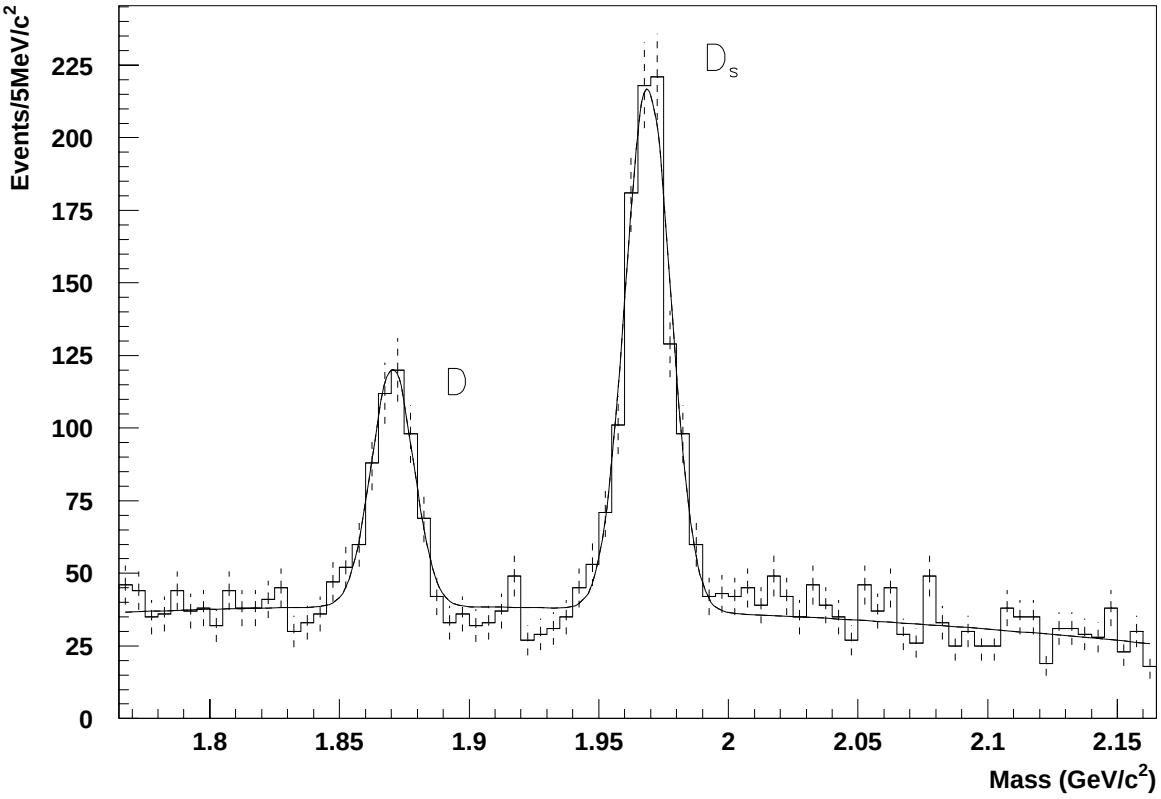

Figure 36: D_s and D mass distributions from all three beams(Σ^-, π^- and *proton*)

mean value of 1872±1.0 MeV(PDG value[29]:1869.3±0.5 MeV) from all three(Σ^-, π^- and *proton*) beams. The individual spectra yield 540±30 D_s^- mesons, 266±23 D_s^+ mesons, 186±23 D^- mesons, and 143±18 D^+ mesons from all three(Σ^-, π^-, and *proton*) beams which are shown in Figure 37. In Figure 38 the individual mass spectra of $D_s^\pm$ are shown from all three beam types separately. The details of these figures are given in Tables 12 and 13. Table 14 compares the number of D_s events with the other experiments [1] [2].

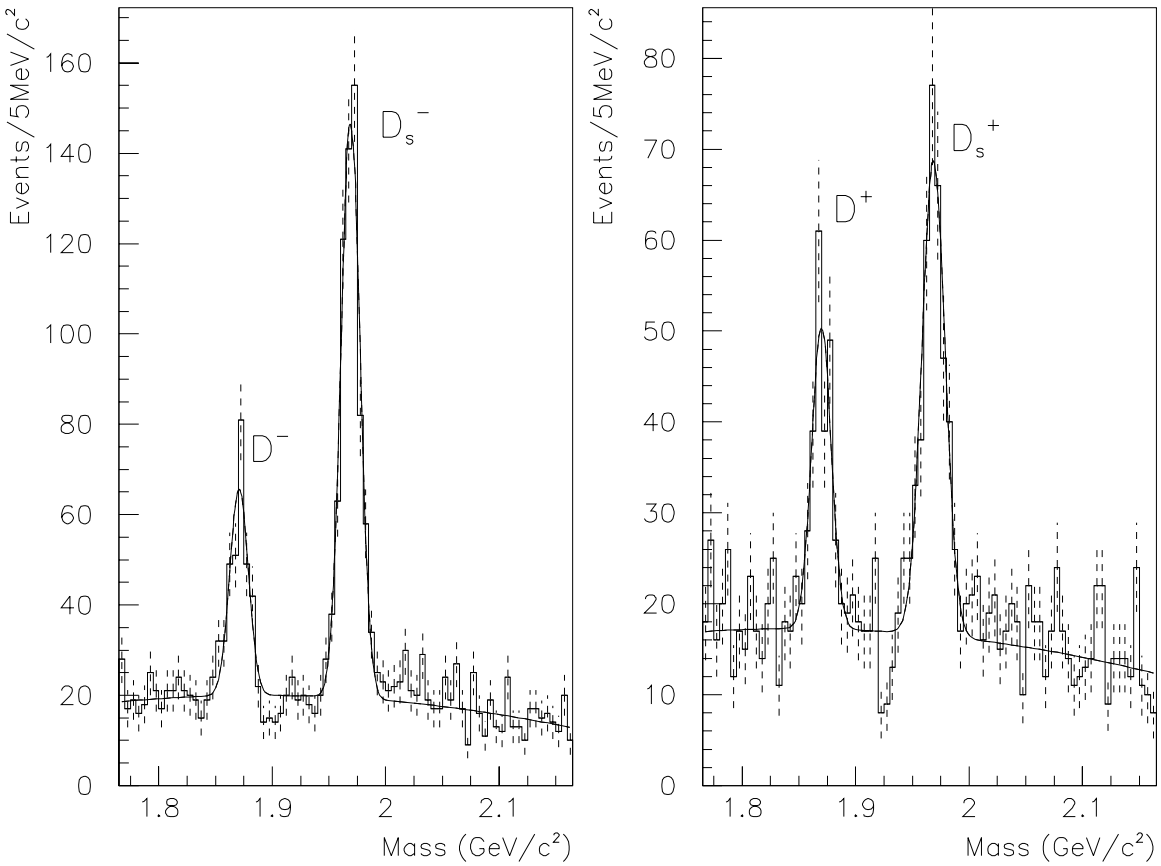

Figure 37: The left and right figures show the D_s^- and D_s^+ mass spectrum from all three beams(Σ^-, π^- and *proton*)

Table 12: D_s^- signal and background events from different beam types

Beam Type	Yield(D_s^-)/bck	Mean(MeV/c^2)	Sigma(MeV/c^2)	χ^2/dof
$\Sigma^- + \pi^- + p$	540±30/58±2	1969±0.5	8±0.5	1.1
Σ^-	502±31/58±2	1968±0.5	8±0.5	0.87
π^-	85±17/8±1	1973±4.0	14±4	0.97
$Proton$	12±2/6±1	1972±1.0	5±1	1.25

The mass resolution of D_s is reasonably stable for different x_F bins. Figure 39 and 40 show mass resolution for each x_F bin from data and embedding Monte Carlo simulation studies, respectively. These figures show that the variation of mass resolution with x_F is small.

For the resonant channels , charm meson decays to $\phi\pi$ were extracted by starting with candidate $\phi \rightarrow K^+K^-$ decays(Figure 41). The ϕ is the combination of two oppositely well-reconstructed charged tracks that are selected by the RICH. These two tracks, assumed to be kaons, were within 10 MeV/c^2 of the ϕ mass (1020 MeV/c^2). For each ϕ candidate, a third track, assumed to be a pion, was extracted for which the invariant mass of the three tracks, assumed to be $KK\pi$, was within a mass window 1765 - 2165 MeV/c^2, which includes both the D_s and Cabibbo-suppresed D masses. Similarly $D_s \rightarrow K*(892)^0K$ was within 70 MeV/c^2 of the K^* mass (892 MeV/c^2)(Figure 42) where K^* is required to be the combination of two oppositely charged tracks, K and π. K is also required to be in the RICH. The invariant mass distributions of both resonant channels are given in Figure 43 and 44 and number of events in the yields and backgrounds are summarized in Table 15 and 16.

These uncorrected data show that there is a clear excess of D_s^- mesons over D_s^+ mesons. In order to study $D_s^\pm$ production asymmetry in detail, $KK\pi$ invariant

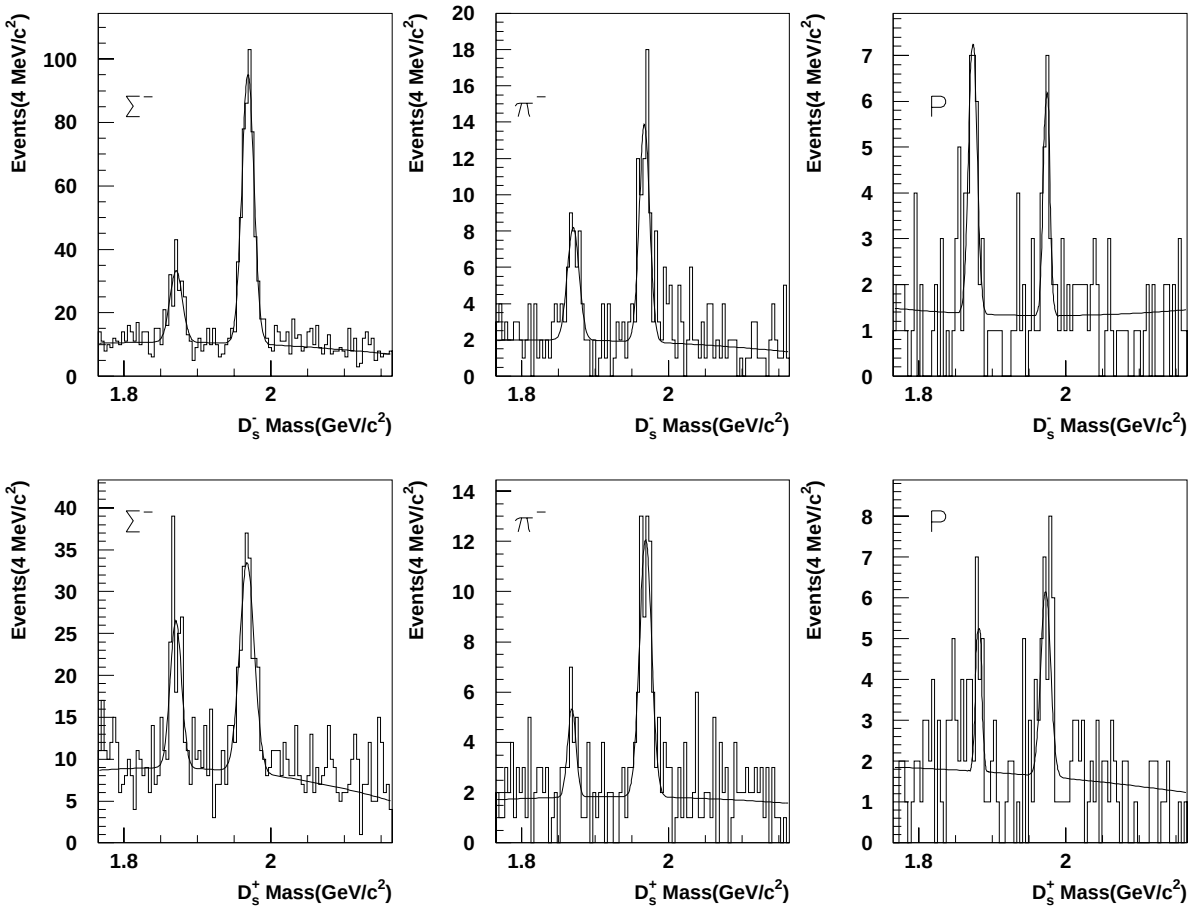

Figure 38: Mass spectrum of D_s^- and D_s^+ from the Σ^-, π^- and *proton* beam

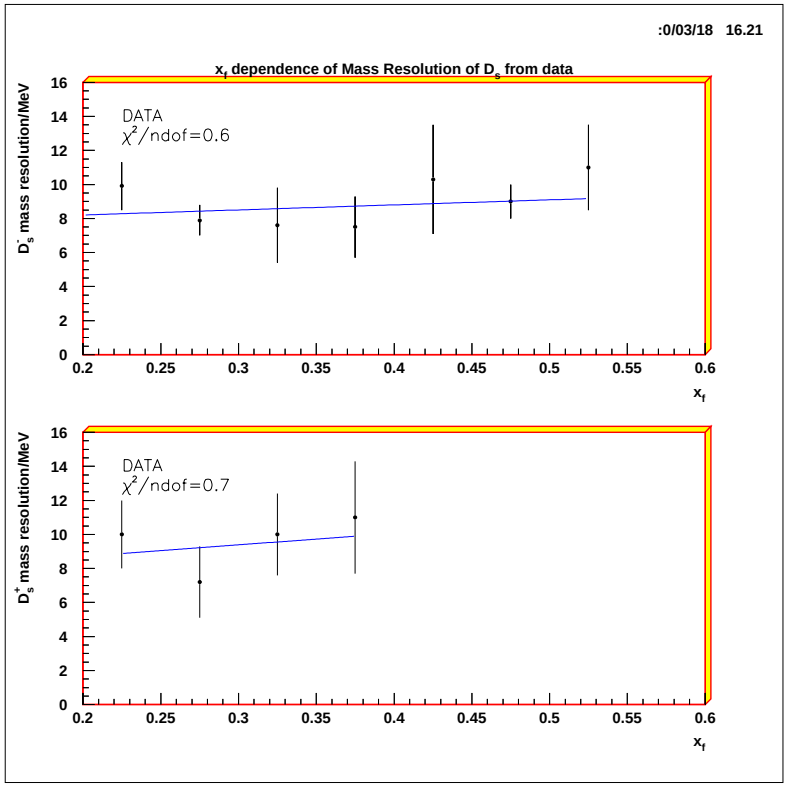

Figure 39: Mass Resolution from data

Table 13: D_s^- signal and background events from different beam types

Beam Type	Yield(D_s^+)/bck	Mean(MeV/c^2)	Sigma(MeV/c^2)	χ^2/dof
$\Sigma^- + \pi^- + p$	266±23/66±1	1969±0.9	9±0.9	1.1
Σ^-	191±19/56±1	1972±1.4	11±1	1.34
π^-	83 ±14/8±1	1968±2.0	11±2	0.97
$Proton$	36±10/10±2	1969±2.0	7±2	1.07

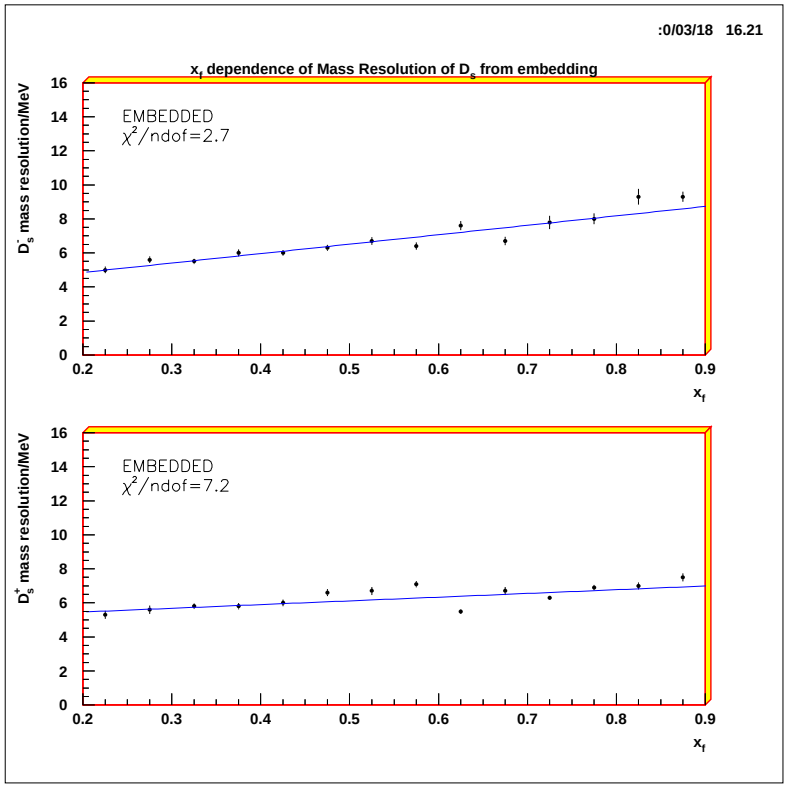

Figure 40: Mass Resolution from embedding monte carlo simulations

Table 14: D_s yield from different experiment

Exper.	Beam	D_s^-	D_s^+
WA89	Σ^- 340 Gev/c	76	<27 90%CL
E791	π^- 500 GeV/c	1257±42	1188±41
E781	Σ^- 600 GeV/c	502±31	191 ± 19

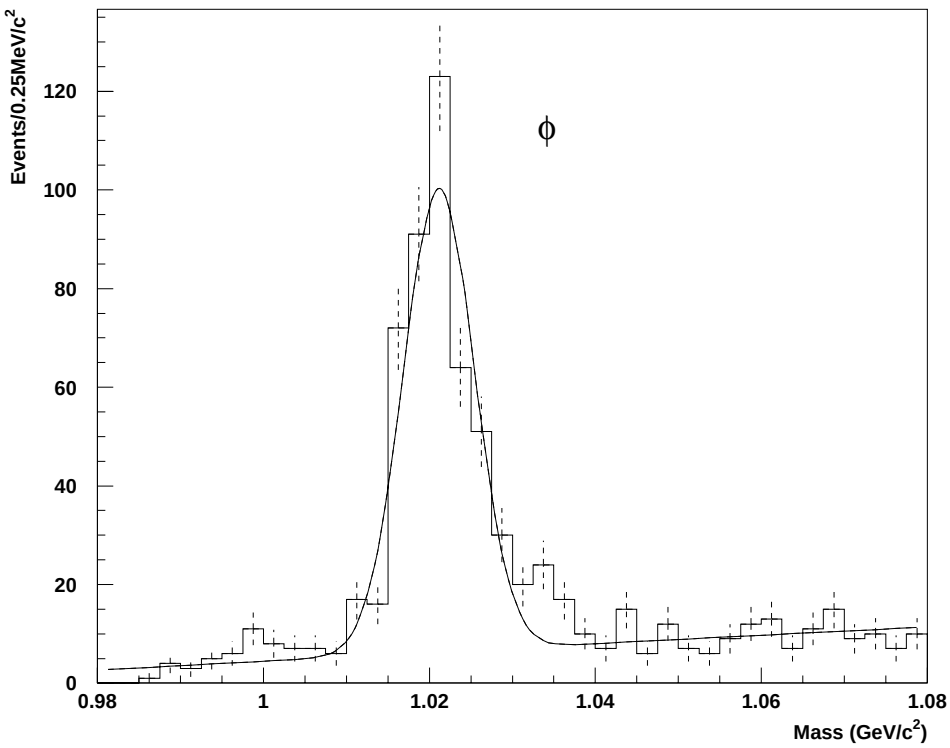

Figure 41: $\phi^0 \to K^- K^+$ invariant mass distribution

Table 15: $D_s \to \phi\pi$ events from different beam types

Beam Type	Yield(D_s)/bck	yield(D_s^-)/bck	yield(D_s^+)/bck
$\Sigma^- + \pi^- + p$	254±17/1±0.2	205±18/2±0.2	91±12/1±0.2
Σ^-	227±19/2±0.2	163±17/1±0.3	44±1/1±0.2

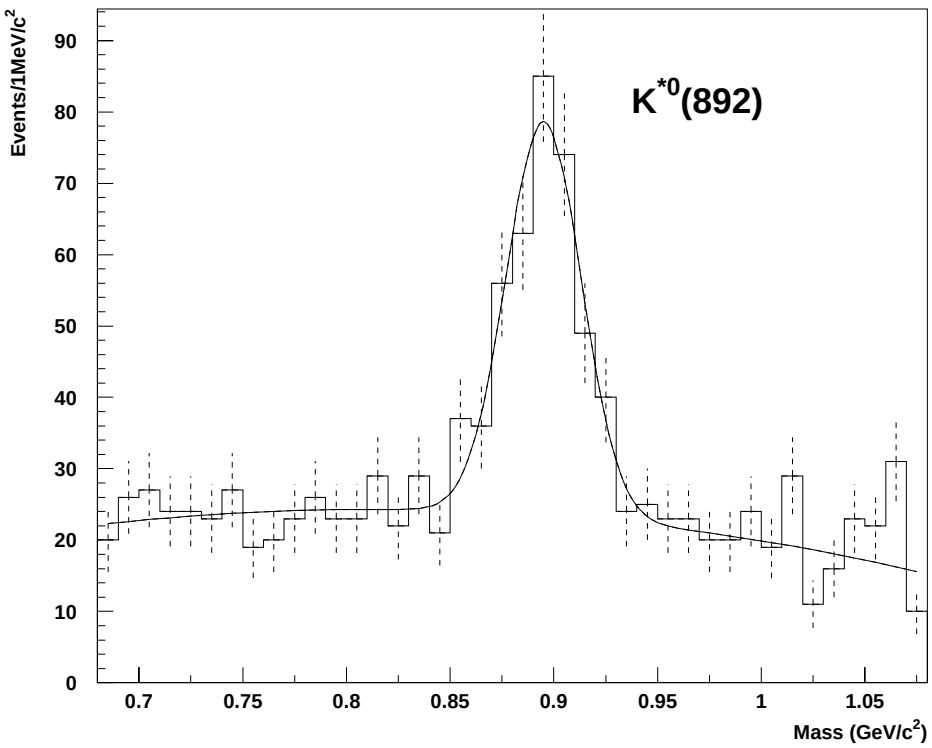

Figure 42: $K^{*0}(892) \to K^-\pi^+$ invariant mass distribution

Table 16: $D_s \to K^*K$ events from different beam types

Beam Type	Yield(D_s)/bck	yield(D_s^-)/bck	yield(D_s^+)/bck
$\Sigma^- + \pi^- + p$	330±19/6±0.3	279±19/6±0.5	154±17/10±0.5
Σ^-	298±24/13±0.5	207±17/5±0.3	80±13/7±0.4

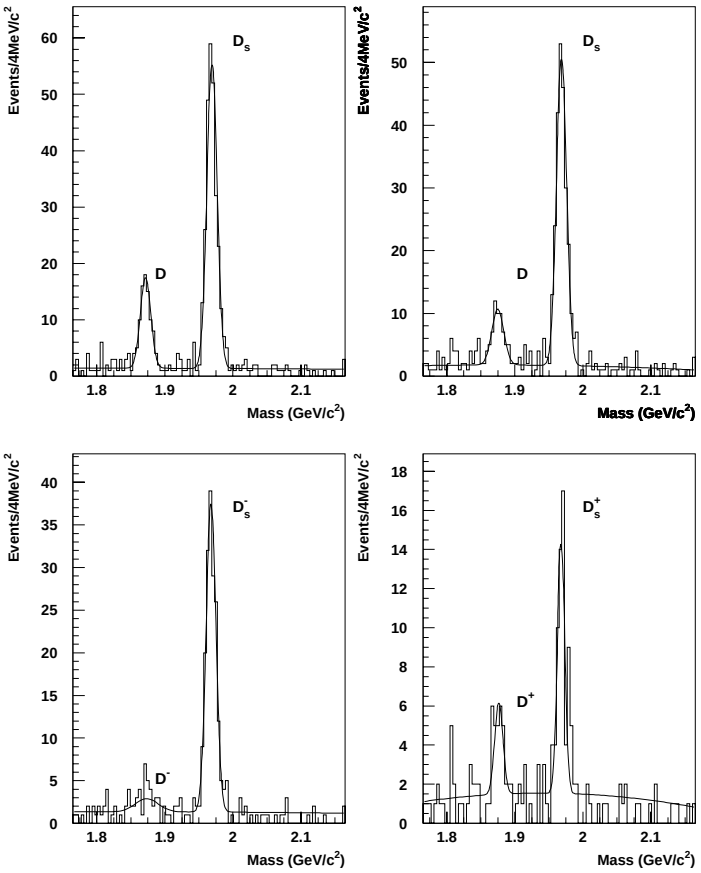

Figure 43: $D_s \to \phi\pi$ mass distributions. Top: Invariant mass distributions from the combined Σ^-, π^-, and *proton* beam(left) and Σ^- beam (right). Bottom: D_s^-(left) and D_s^+(right) from Σ^- beam only

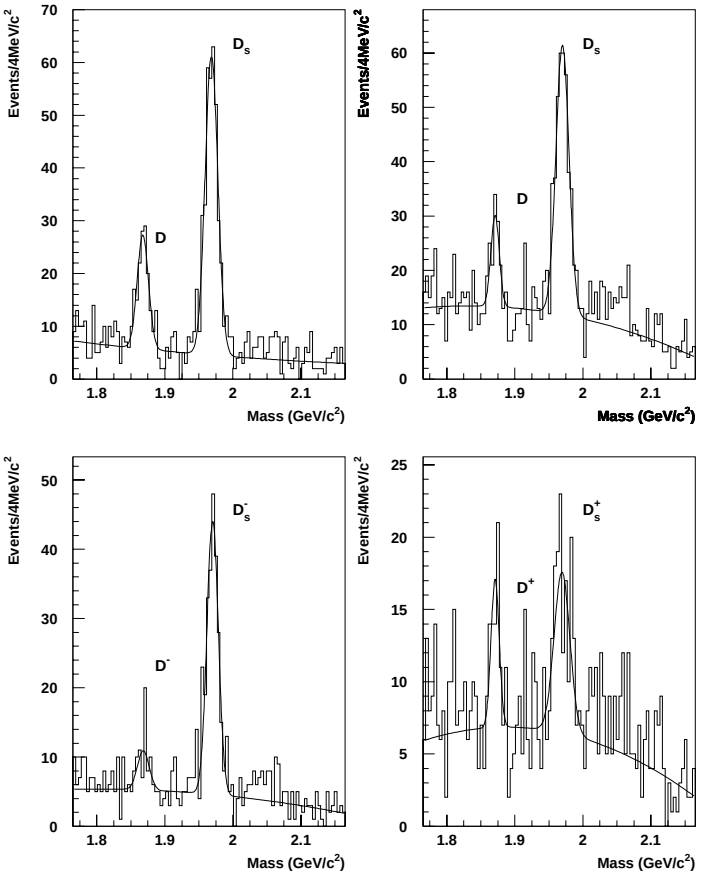

Figure 44: $D_s \to K^*K$ mass distributions. Top: Invariant mass distributions from the combined Σ^-, π^-, and *proton* beam(left) and Σ^- beam (right). Bottom: D_s^-(left) and D_s^+(right) from Σ^- beam only

mass plots need to be done in different possible x_F and p_t^2 ranges to obtain yields as a function of x_F and p_t^2.

So far the yields discussed are the yields obtained by fitting to two Gaussians with a quadratic background. For low statistic channels, this technique does not quite work. D_s mass spectrum has low statistics for higher x_F and p_t^2 ranges (see Figure 58 and 66(Appendix B)) and fitting to Gaussians with a quadratic background does not yield satisfactory results. Another technique is used to find the yields, which is the "sideband subtraction method". This method works equally well for all types of statistics; however, it brings in some systematic errors, which will be discussed in section 5.7. Similar yields are obtained from both techniques with the high statistics channels.

5.5 D_s Yields: Sideband Subtraction Method

The purpose of this method is to subtract the background under the signal. In order to find out the net yield a signal region of 50 $MeV/c^2(\sim \pm 3\sigma)$ is taken from 1945 to 1995 MeV/c^2 and a 40 MeV/c^2 left sideband region (1900-1940 MeV/c^2) and a 60 MeV/c^2 right sideband region (2045-2105 MeV/c^2). These regions are shown in Figure 45. Since D meson mass is on the left of the signal region and $D^*(2010)$ is on the right region, the left and right sidebands must avoid these regions. The left and right sideband regions are added and an average number of events for one bin is determined. Then this number is multiplied by the number of bins in the 50 MeV/c^2 signal region. The resulting number of events are subtracted from the total events in the signal region.

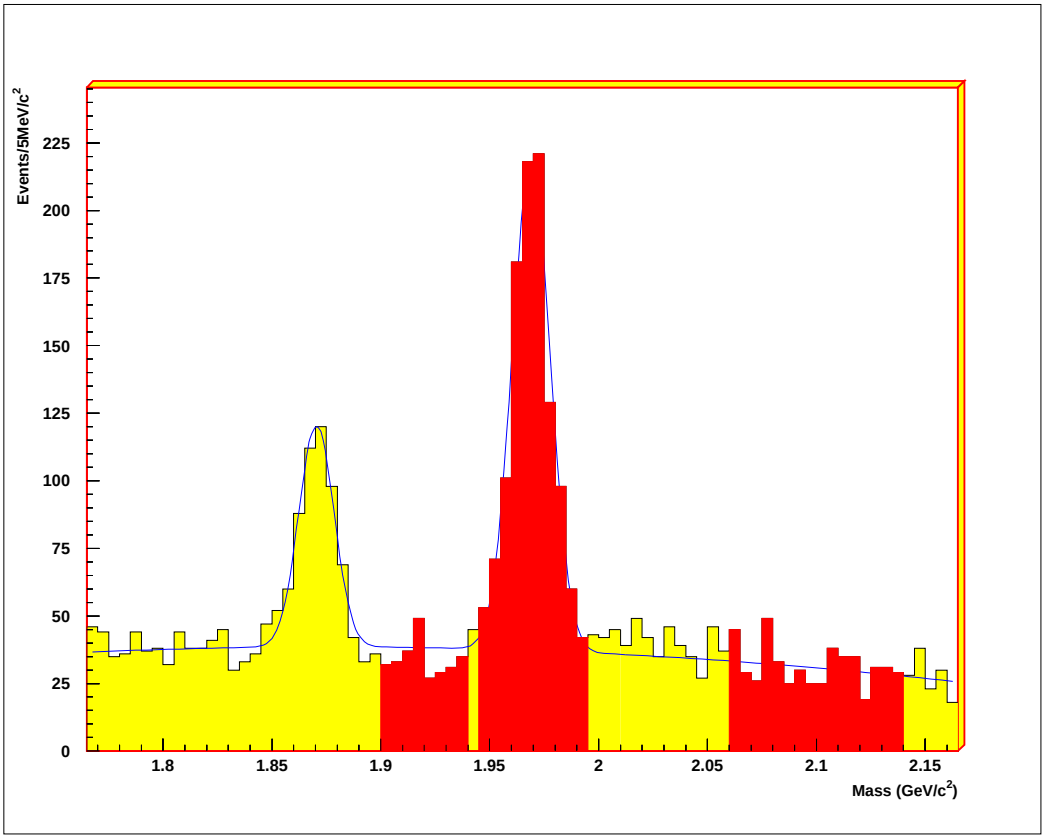

Figure 45: Left/right sideband and signal regions used for sideband subtraction method

5.6 Statistical Error Analysis

Contributions to the statistical error on the asymmetry come from individual yields and related corrections. Calculating the error on the asymmetry involves two steps:

- Statistical error for the background subtracted signal
- Statistical error due to the combined efficiency and acceptance corrections

5.6.1 Statistical error for the background subtracted signal

The yield is calculated as $y = s - f * b$, where s is the number of events in the signal region, f is a normalization constant, and b is the number of events in the sideband region. The error on the yield is:

$\sigma_y = \sqrt{s + b * f^2}$

5.6.2 Statistical error due to the combined efficiency and acceptance corrections

Since efficiency is the ratio of reconstructed embedded events to generated events as explained in the previous section, the error comes from the ratio of reconstructed embedded and generated events.

$\sigma_\epsilon = \sqrt{\frac{(1-\epsilon)\epsilon}{gen}}$

where ϵ and gen stand for efficiency and number of generated events, respectively.

Basically the total statistical error comes from the yield and efficiency measurements, since acceptance corrected data are $y_c = \frac{y}{\epsilon}$, where y is the yield and ϵ is the efficiency. Combination of these two errors gives the error on the acceptance corrected yield (σ_{y_c}).

$\sigma_{y_c} = \frac{1}{\epsilon}\sqrt{\sigma_y^2 + \frac{y^2}{\epsilon^2}\sigma_\epsilon^2}$

Error in the asymmetry calculation, which consists of both $D_s^\pm$ charge conjugate states becomes:

$\sigma_A = \frac{2}{(N_{D_s^-}+N_{D_s^+})^2}\sqrt{(N_{D_s^+})^2\sigma^2_{N_{D_s^-}} + (N_{D_s^-})^2\sigma^2_{N_{D_s^+}}}$

where N (=y_c) is the corrected yield.

5.7 Systematic Error Analysis

Possible systematic errors are:

- Systematic errors due to the sideband subtraction method
- Error in the efficiency and acceptance correction
- Error making the cuts(various cuts used for event selection)
- Systematic effect on asymmetries
- RICH efficiency effect
- $D^\pm$ contamination effect

5.7.1 Systematic errors due to the sideband subtraction method

Systematic error from the sideband subtraction method is not observed to be significant. Different signal and sideband regions and different binning methods are studied. The detailed of this work is given in Figure 46. The n parameters, which will be discussed later, are compared between D_s^- and D_s^+. In Figure 46 the first plot(Figure I), the bins are shifted with a 0.025 range while keeping the initial bin fixed. Since at the smaller and larger x_F regions, efficiency is increasing or decreasing rapidly, this plot will show the systematic errors coming from these regions. In Figure

II, the number of bins is varied from 4 bins to 9 bins in the x_F from 0.2 to 0.5. The n parameters that are in this region look stable. This contribution to the systematic error is small. In Figure III, the width of the signal region is varied from 30 MeV/c^2 to 60 MeV/c^2 at fixed x_F and bins. Here the systematic effect on the D_s^+ is not negligible. It is comparable with the statistical error and it is estimated to be 50% of the statistical error. In Figure IV, the left and right sideband regions are varied from 60 MeV/c^2 to 140 MeV/c^2 at fixed x_F and bins. This contribution also yields little systematic error. In Figure V, left sideband and signal regions are kept constant and only right sideband region is varied. The systematic effect on the n value of D_s^+ is comparable with the statistical error. The systematic error here is estimated 50% of statistical. In the last figure (Figure VI), 5 segmented charm targets(tgt #s:Cu(6, 7), C(8, 9, 10)) are considered separately. The last points in Figure VI are obtained from all five targets.

Generally the uncertainty in the n parameters are large compared to the variation due to different sidebands(See Figure 46). Systematic effects coming from the sideband subtraction method on the D_s^- is negligible. However it is not negligible for D_s^+. It is estimated to be 50% of the statistical error.

5.7.2 Error in the efficiency and acceptance correction

The difference of reconstruction efficiency between two-charge conjugate states is estimated $< 4\%$(Refer back Figure 32). The systematic effect from this is negligible.

5.7.3 Error making the cuts(various cuts used for event selection)

Since we apply the cuts equally to both charge states, we do not expect a significant effect on the asymmetry and n parameter.

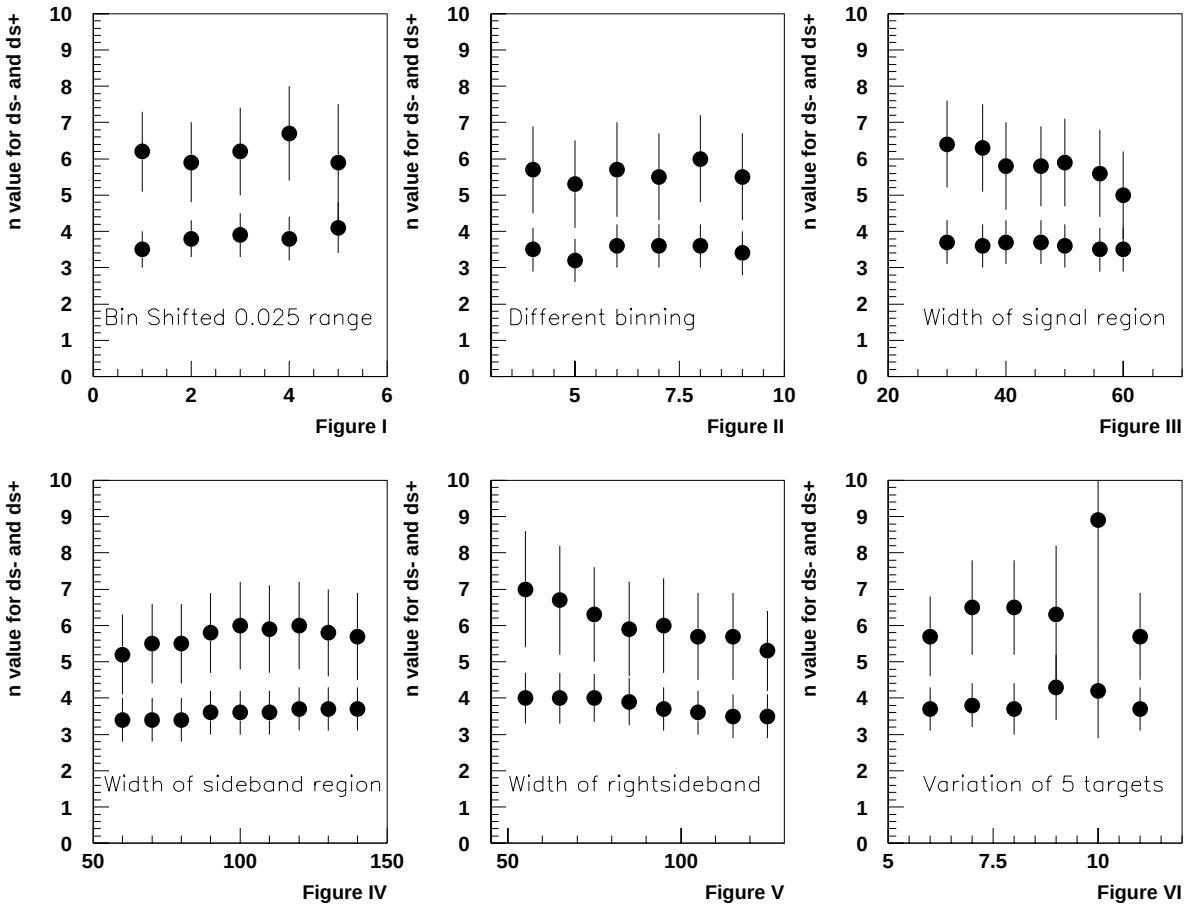

Figure 46: Systematic study on the sideband subtraction method. Upper and lower dots are the n parameter for D_s^+ and D_s^- respectively

5.7.4 Systematic effect on asymmetries.

Figure 32 shows that our detectors are charge symmetric so there should not be any false asymmetry. We are therefore justified in applying the cuts equally to both charge states. We do not expect a significant effect on the asymmetry and parameter n.

5.7.5 RICH efficiency effect:

Since both K^+ and K^- are detected by the RICH, even if there is an asymmetry in detecting $\pm$ kaons, the combined efficiency for detecting K^+ and K^- in D_s^- and D_s^+ would be the same. We do not expect any significant effect to first order.

5.7.6 $D^\pm$ contamination effect:

$D^\pm$ contamination in the $D_s^\pm$ peak is comparable to the uncertainty in the total number of events. It may not effect the n parameter since the statistical errors are large enough.

20 events are estimated as contamination of $K\pi\pi$ events(refer back to Figure 30) in the $K^-K^+\pi^+$ out of 267 events and 35 events are estimated as contamination of $K\pi\pi$ events in the $K^-K^+\pi^-$ out of 543 events.

The asymmetry is associated with contamination

(543-267)/(543+267)=0.365

and without contamination is

(508-247)/(508+247)=0.345

Thus the systematic effect from the contamination is estimated as

(0.365-0.345)/0.365=0.055 $\approx$ 5%.

CHAPTER VI
RESULTS AND CONCLUSIONS

6.1 x_F Distributions

The production of a particle that has one quark or anti-quark in common with the beam particle is expected to be enhanced at high momentum. This means that the particle which has the common quark with the beam (the leading particle) should have a harder x_F than a particle with no quark in common with the beam particle (non-leading particle). The difference in x_F spectra between leading and non-leading particles have been studied and explained successfully by several theoretical models[10, 30]. The WA89[1] experiment, which used Σ^- beam at 340 GeV/c momentum, described their production asymmetry measurement between leading and non-leading charmed mesons in the framework of the string model [31] that is discussed earlier.

The usual phenomenological parameterization of the inclusive double differential cross section used to describe the experimental data is given by [32]

$$\frac{d\sigma}{dx_F dp_t^2} = A(1 - x_F)^n e^{-bp_t^2}$$

where A, n and b are parameters used to fit the data and x_F is the Feynman-X parameter [33] which gives the fraction of available longitudinal momentum in the overall center of mass carried by an object divided by the maximum possible longitudinal

momentum in that frame or:

$x_F = \frac{2p_{zcm}}{\sqrt{s}}$

and p_t^2 is the transverse momentum squared or:

$p_t = \sqrt{p_x^2 + p_y^2}$

In fact kinematic considerations provide predictions for the power n at high x_F, and QCD calculations give average p_t parameters comparable to the charm quark mass.

It has been observed by WA89[1], E791[2], NA27[34], and [35] experiments that n is always larger for non-leading particle production than for leading particle production.

In this measurement the D_s yield as a function of x_F is obtained in the region, $0.15 < x_F < 0.6$. It is extracted from the background by the sideband subtraction method discussed in section 5.5. The subtraction is performed for both resonant and $KK\pi$ channels. Then the data are further corrected for reconstruction efficiency, which is discussed in the section 5.3. For the $D_s \to KK\pi$ the x_F distributions, corrected for the efficiencies, are shown in Figure 47.

The left histogram is the x_F distribution for D_s^- and the right one is for D_s^+ from the Σ^- beam only. As mentioned before, $D_s^-(s\bar{c})$ is a leading particle for the $\Sigma^-(dds)$ beam since it has a same quark, s, with the beam particle. On the other hand, $D_s^+(c\bar{s})$, which does not have any common quark with the beam, is a non-leading particle. Preliminary results yield a larger n value for D_s^+ than D_s^-, which supports the leading particle assumptions.

The total number of corrected events from the resonant states $D_s \to K^*K$ and $D_s \to \phi\pi$ are used for the x_F distributions, which are shown in Figure 48. The observed number of events after background subtraction(N), efficiency(ϵ), and the

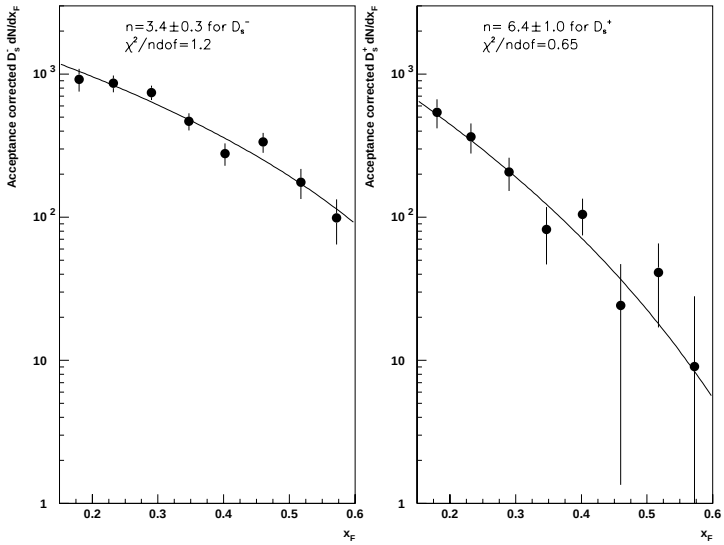

Figure 47: x_F distribution of $D_s^{\pm} \to KK\pi^{\pm}$ charm strange meson

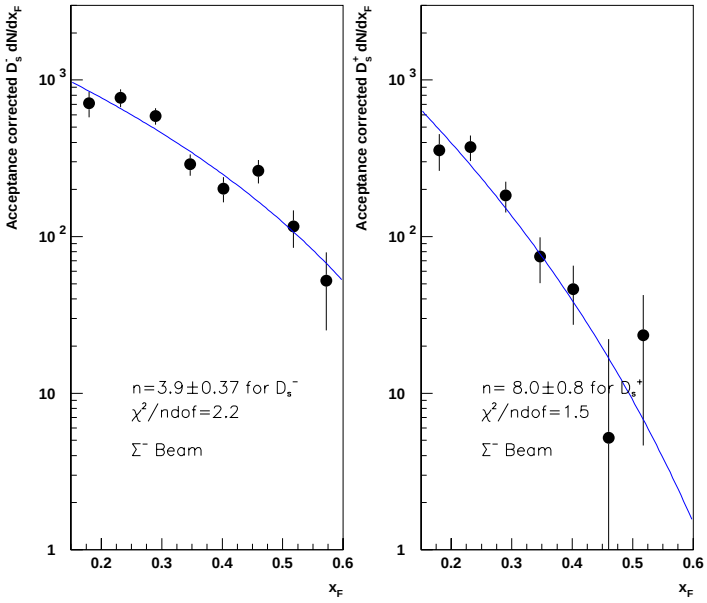

Figure 48: x_F distribution of $D_s^{\pm} \to K^*K + \phi\pi$ charm strange meson

Table 17: $D_s^{\pm} \to K^+K^-\pi^{\pm}$ from Σ^- beam

	$D_s^- \to K^+K^-\pi^-$			$D_s^+ \to K^+K^-\pi^+$		
x_F range	N	$\epsilon\%$	N_c	N	$\epsilon\%$	N_c
$0.15 < x_F < 0.21$	51 ±9	5.6 ±0.2	921±117	33±7	6.1±0.2	542±125
$0.21 < x_F < 0.26$	83±11	9.6±0.3	861±91	36±8	9.9±0.4	364±87
$0.26 < x_F < 0.32$	103±11	13.8±0.4	743±65	26±7	12.8±0.4	207±54
$0.32 < x_F < 0.37$	69±9	14.7±0.5	467±54	12±5	14.8±0.5	82±35
$0.37 < x_F < 0.43$	42±7	15.2±0.5	278±45	16±5	15.5±0.5	104±30
$0.43 < x_F < 0.48$	51±8	15.2±0.5	335±49	4±4	15.5±0.5	24±23
$0.48 < x_F < 0.54$	24±6	14.1±0.5	176±37	6±3	14.2±0.5	41±24
$0.54 < x_F < 0.60$	12±4	11.8±0.5	99±32	1±2	12.0±0.5	9±19

corrected number of events(N_c) for each specific x_F range are summarized in Tables 17, 18, 19 and 20.

Figure 49 show the acceptance corrected x_F distributions from the 600 GeV/c π^- beam. In this case both D_s^- and D_s^+ are non-leading ($\pi^- = d\overline{u}$). Accordingly we don't expect any significant asymmetry for the π^- beam. Since the statistics are low, only the $D_s \to KK\pi$ channel is used for the π^- beam.

Both x_F distributions indicate that there is no obvious difference between x_F behaviors of D_s^- and D_s^+. The n parameters from Σ^- and π^- beams are summarized in the Table 22 (systematic error from the sideband subtruction method for the D_s^+ is also added). The WA89 [1] experiment is the only previous experiment to use a Σ^- hyperon beam to measure the production asymmetry between D_s^- and D_s^+. Since they had low statistics, the number of events observed in a bin was low, especially at, high x_F. SELEX is the only experiment to be able to measure x_F distributions with high statistics from a 600 GeV/c Σ^- beam.

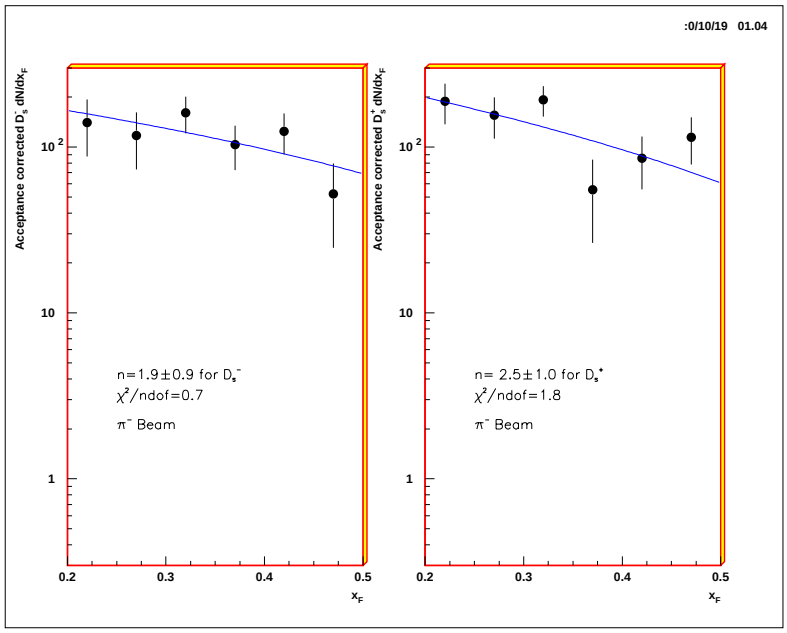

Figure 49: x_F distribution of D_s^-(left) and D_s^+(right) charm strange meson from π^- beam

Table 18: $D_s^\pm \to \phi\pi^\pm$ from Σ^- beam

	$D_s^- \to \phi\pi^-$			$D_s^+ \to \phi\pi^+$		
x_F range	N	$\epsilon\%$	N_c	N	$\epsilon\%$	N_c
$0.15 < x_F < 0.21$	21 ±5	5.6 ±0.4	377±87	9±3	5.2±0.4	168±63
$0.21 < x_F < 0.26$	35±6	9.3±0.5	374±67	18±4	9.5±0.5	184±45
$0.26 < x_F < 0.32$	38±6	12.7±0.6	296±50	12±4	12.1±0.5	100±30
$0.32 < x_F < 0.37$	18±4	14.3±0.6	126±30	4±2	14.2±0.6	28±14
$0.37 < x_F < 0.43$	11±3	14.6±0.6	72±23	2±1	13.1±0.5	12±11
$0.43 < x_F < 0.48$	16±4	13.2±0.6	118±31	1±2	13.1±0.5	6±12
$0.48 < x_F < 0.54$	7±3	11.8±0.5	56±23	3±2	12.3±0.5	21±15
$0.54 < x_F < 0.60$	3±2	12.1±0.5	25±14	0±0	11.6±0.5	0±0

Table 19: $D_s^{\pm} \to K^{\pm}\overline{K}^*(892)^0$ from Σ^- beam

x_F	$D_s^- \to K^-\overline{K}^*(892)^0$			$D_s^+ \to K^+\overline{K}^*(892)^0$		
x_F range	N	$\epsilon\%$	N_c	N	$\epsilon\%$	N_c
$0.15 < x_F < 0.21$	16±5	4.8±0.4	332±99	10±4	5.2±0.5	189±69
$0.21 < x_F < 0.26$	35±6	8.9±0.5	398±75	18±5	9.8±0.5	188±51
$0.26 < x_F < 0.32$	40±7	13.6±0.6	293 ±49	11±4	13.6±0.6	83±27
$0.32 < x_F < 0.37$	26±5	15.9±0.6	164±33	7±3	15.7±0.6	47±20
$0.37 < x_F < 0.43$	22±5	16.7±0.6	130±29	6±2	16.3±0.6	34±15
$0.43 < x_F < 0.48$	22±5	15.2±0.6	145±32	-0.08±2	14.4±0.6	-0.55 ±12
$0.48 < x_F < 0.54$	9±3	14.2±0.6	60±21	1±2	13.6±0.5	3 ±12
$0.54 < x_F < 0.60$	6±3	11.8±0.5	52±23	-0.4±1	11.9±0.5	-3 ±3

Table 20: $D_s^{\pm} \to \phi\pi^{\pm} + K^{\pm}\overline{K}^*(892)^0$

x_F	D_s^-	D_s^+
x_F range	N_c	N_c
$0.15 < x_F < 0.21$	709±132	357±94
$0.21 < x_F < 0.26$	772±100	372±69
$0.26 < x_F < 0.32$	589±70	183±41
$0.32 < x_F < 0.37$	290±45	75±24
$0.37 < x_F < 0.43$	202±37	46±19
$0.43 < x_F < 0.48$	263±44	5±17
$0.48 < x_F < 0.54$	116±31	23±19
$0.54 < x_F < 0.60$	52±27	-3.5±3

Table 21: $D_s^{\pm} \to K^+K^-\pi^{\pm}$ from π^- beam

x_F	D_s^-			D_s^+		
x_F range	N	$\epsilon\%$	N_c	N	$\epsilon\%$	N_c
$0.20 < x_F < 0.25$	4 ±2.6	10 ±0.4	38±26	8.7±3	11 ±0.4	79±29
$0.25 < x_F < 0.30$	8.8±3.8	13.8±0.5	63±28	6±3	14.4±0.4	43±24
$0.30 < x_F < 0.35$	8.9 ±3.4	15.8±0.5	59 ±23	10±4	17.4±0.5	58±22
$0.35 < x_F < 0.40$	10.7 ±3.5	18±0.5	59 ±20	2±2.5	17.6±0.5	12±14
$0.40 < x_F < 0.45$	14.7 ±4	14.9±0.5	88 ±24	5±3	17±0.5	30±18
$0.45 < x_F < 0.50$	3.3 ±2.4	13.9±0.5	20 ±15	7.5±3	16±0.5	47 ±21

Table 22: Summary of the n parameters

Meson	x_F	Beam	n value
$D_s^- \to K^+K^-\pi^-$	0.15 - 0.6	Σ^-	3.4±0.3
$D_s^+ \to K^+K^-\pi^+$	0.15 - 0.6		6.4±1.0±0.05
$D_s^- \to K^*K^- + \phi\pi^-$	0.15 - 0.6	Σ^-	3.9±0.4
$D_s^+ \to K^*K^- + \phi\pi^+$	0.15 - 0.6		8.0±0.8
$D_s^- \to K^+K^-\pi^-$	0.2 - 0.5	π^-	1.9±0.9
$D_s^+ \to K^+K^-\pi^+$	0.2 - 0.5		2.5±1.0

Table 23: $D_s^{\pm} \rightarrow K^+K^-\pi^{\pm}$ from Σ^- beam

$p_t^2 (GeV/c)^2$	D_s^-			D_s^+		
p_t^2 range	N	$\epsilon\%$	N_c	N	$\epsilon\%$	N_c
$0.0 < p_t^2 < 0.5$	176±16	8.8±0.1	1986±187	66±12	8.7±0.1	758±142
$0.5 < p_t^2 < 1.0$	105±12	8.8±0.2	1190±137	23±8	8.8±0.2	264±88
$1.0 < p_t^2 < 1.5$	61 ±9	9.3±0.3	655 ±99	29±6	9.4±0.3	308±68
$1.5 < p_t^2 < 2.0$	36 ±7	8.8±0.4	409 ±76	17±5	9.0±0.4	191±53
$2.0 < p_t^2 < 2.5$	29 ±6	9.1±0.5	323 ±67	10±4	8.4±0.5	113±43
$2.5 < p_t^2 < 3.0$	19 ±5	8.7±0.6	225 ±57	5±3	9.0±0.6	59 ±31
$3.0 < p_t^2 < 3.5$	8 ±3	9.9±0.7	84 ±33	4±2	10.6±0.7	34 ±19
$3.5 < p_t^2 < 4.0$	7 ±3	9.6±0.8	70 ±31	1±1	9.1±0.8	8 ±18

6.2 p_t^2 Distributions

An analysis of transverse momentum data is carried out using exponents which characterize the dependence of the cross sections on p_t^2. The results of this analysis allow any model to be critically compared to the data in a simple but meaningful way. Our results for the p_t^2 distribution of D_s charm strange mesons is shown in Figure 50. The solid line is a fit to the function

$$\frac{d\sigma}{dp_t^2} = Ce^{-bp_t^2}$$

This form fits well for all p_t^2 distributions over the range of 0.0 - 4.0 $(GeV/c)^2$.

The number of events for each p_t^2 bin is extracted using the sideband subtraction method and the data are corrected for the efficiencies that are calculated for each p_t^2 bin. Table 23 shows the summary of the data and the efficiencies for each specific p_t^2 bin. Measured b parameters are summarized in Table 24

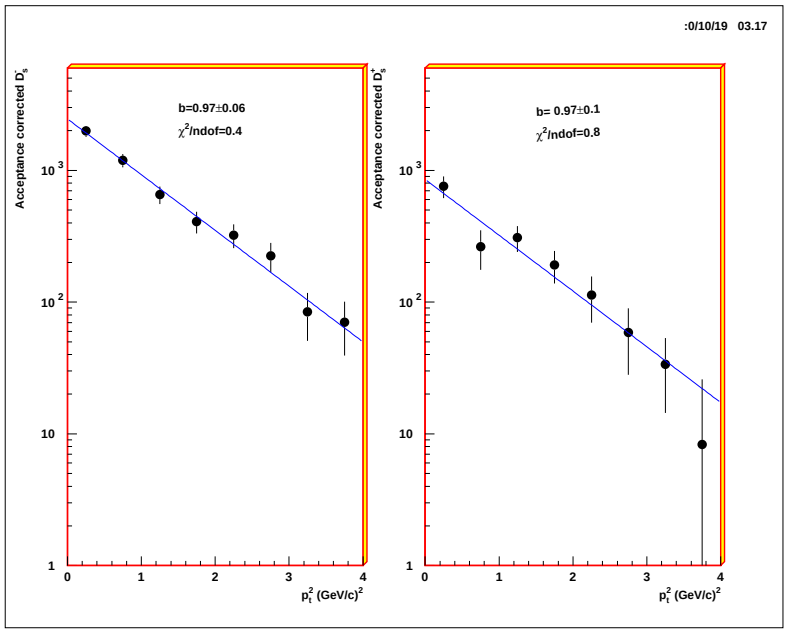

Figure 50: p_t^2 distribution of $D_s^{\pm}$ charm strange mesons

Table 24: Summary of the b parameters

Meson	$p_t^2(GeV/c)^2$	Beam	b value
D_s^-	0.0 - 4.0	Σ^-	0.97±0.06
D_s^+	0.0 - 4.0		0.97±0.1

6.3 Asymmetry

The difference between the production of leading and non-leading particles can be quantified by measuring the production asymmetry parameter defined as:

$$\mathrm{A}(x_F, p_t^2) \equiv \frac{N_{D_s^-} - N_{D_s^+}}{N_{D_s^-} + N_{D_s^+}},$$

where $N_{D_s^-}$ and $N_{D_s^+}$ are the yields (number of events in the signal region after sideband subtraction) for D_s^- and D_s^+, respectively.

6.3.1 x_F and p_t^2 Dependent Asymmetry

The Σ^- beam is used for the x_F and p_t^2 dependent asymmetry, however because of low statistics the π^- beam is used only for the x_F dependent asymmetry. The asymmetry is calculated for each bin over an x_F range of 0.15 to 0.6 for Σ^- and 0.2 - 0.5 for π^- beam and a p_t^2 range of 0.0 to 4.0 $(GeV/c)^2$ for Σ^- beam. Outside these ranges the statistics were too small to obtain meaningful results (see Figure 58,..., 67(Appendix B)).

The production asymmetry is measured as a function of x_f for both $KK\pi$ and resonant channels. There is a small difference between asymmetries obtained from the resonant and $KK\pi$ channels. This can be accounted for by contamination of the $KK\pi$ channel by misidentified beams, which is not corrected for (see previous section for the contamination). Figures 51 and 52 show the acceptance corrected asymmetry with bins of 0.063 in x_F. It can be seen that there is a big asymmetry in favor of D_s^-(leading). Note that the asymmetry is increasing gradually as x_F increases(statistical errors only shown here).

On the other hand the production asymmetry from the π^- beam(Figure 53)

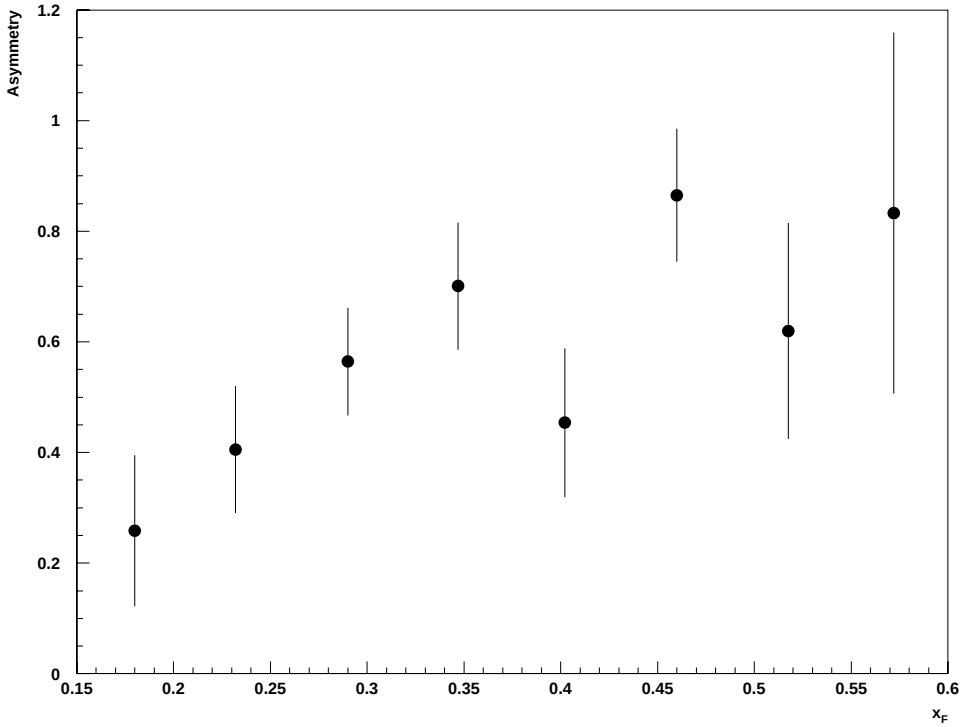

Figure 51: $D_s \to KK\pi$ production asymmetry as a function of x_F from Σ^- beam

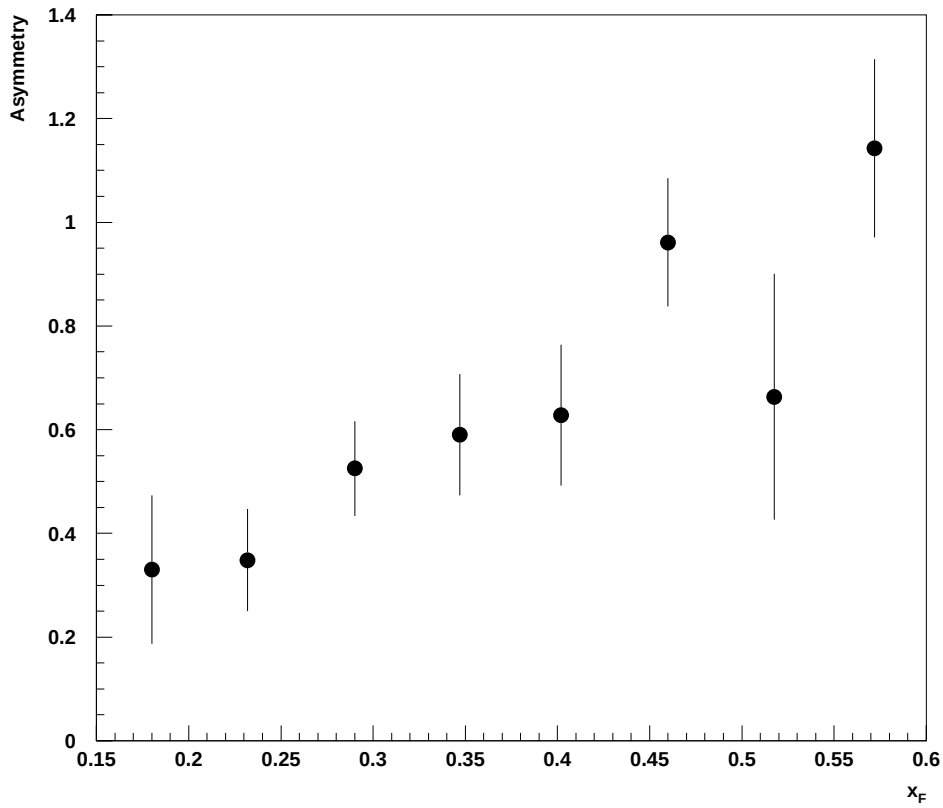

Figure 52: $D_s \to K^* K + \phi\pi$ charm strange meson production asymmetry as a function of x_F from Σ^- beam

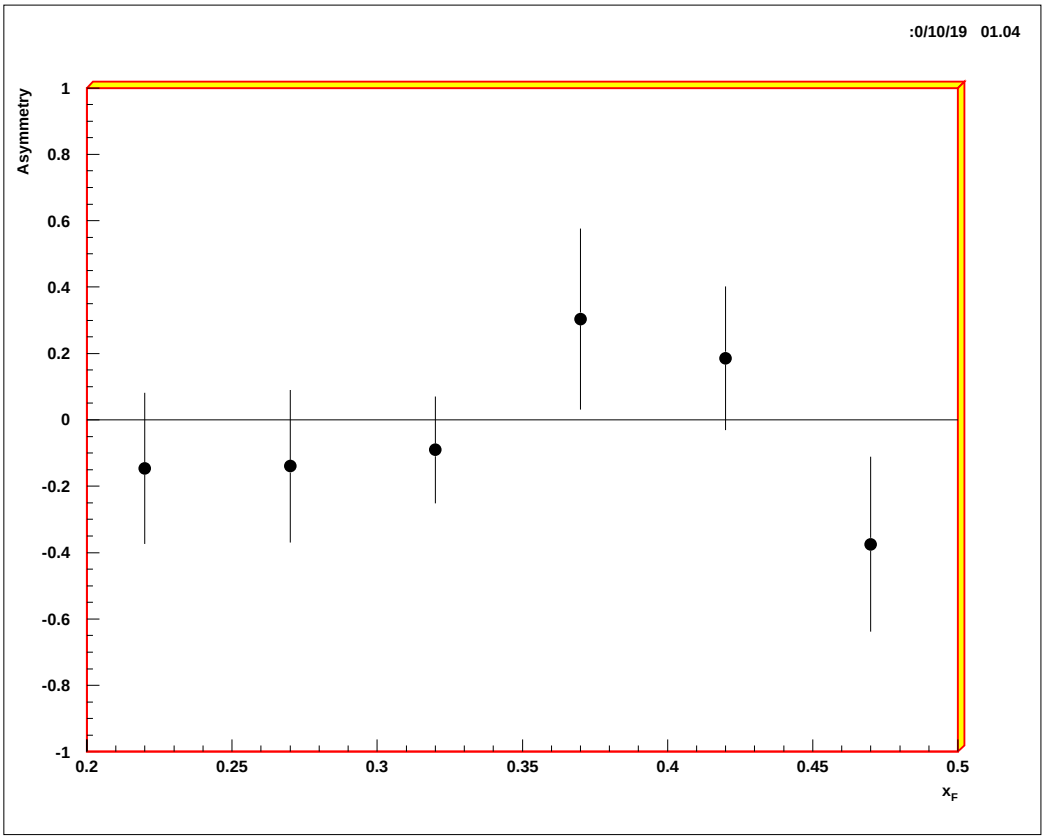

Figure 53: $D_s \to KK\pi$ production asymmetry as a function of x_F from π^- beam

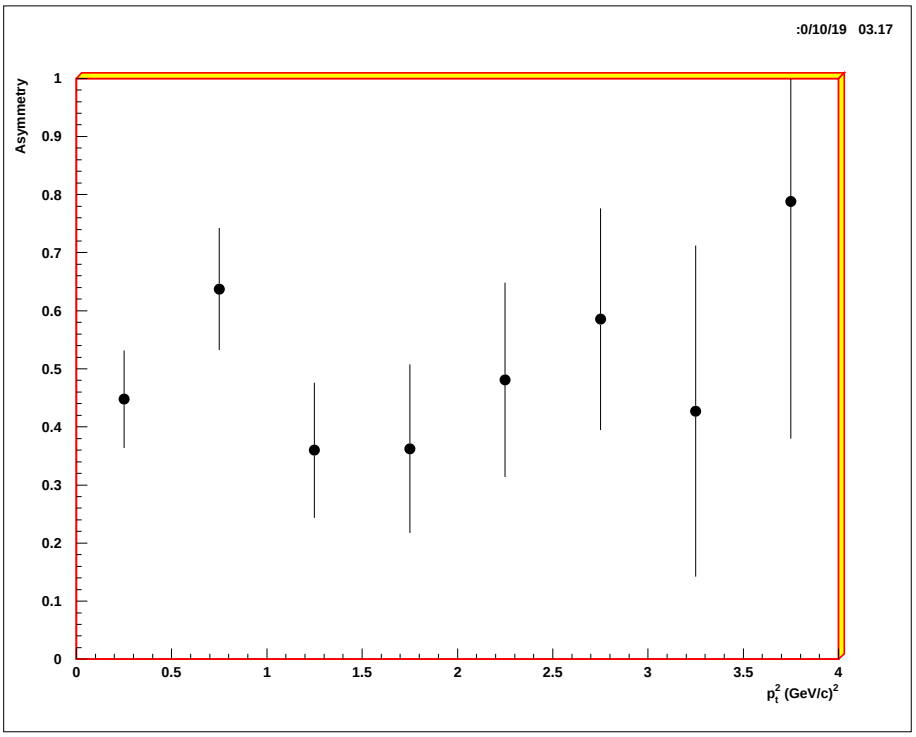

Figure 54: $D_s \to KK\pi$ production asymmetry as a function of p_t^2

is consistent with no net asymmetry. In this case both charge conjugate states are non leading, so we do not expect any asymmetry between production of D_s^- and D_s^+. The asymmetry values for both Σ^- and π^- beams are summarized in Table 25. For Comparison E791[2] obtained an asymmetry of 0.032±0.022 for D_s from a π^- beam in the x_F range -0.1 to 0.5.

The acceptance corrected production asymmetry as a function of p_t^2 is shown in Figure 54 and summarized in Table 26 respectively. The result is consistent with a flat asymmetry distribution. Statistical errors are only shown here.

Table 25: Summary of Asymmetry(x_F) from Σ^- and π^- beam

Σ^- *Beam*			π^- *Beam*	
x_F	$D_s \to K^*K + \phi\pi$	$D_s \to KK\pi$	x_F	$D_s \to KK\pi$
$0.15 - 0.21$	0.330 ±0.14	0.258 ±0.14	$0.20 - 0.25$	-0.15 ±0.23
$0.21 - 0.26$	0.348 ±0.10	0.405 ±0.11	$0.25 - 0.30$	-0.14±0.23
$0.26 - 0.32$	0.525 ±0.09	0.564 ±0.10	$0.30 - 0.35$	-0.09±0.16
$0.32 - 0.37$	0.590 ±0.11	0.701 ±0.12	$0.35 - 0.40$	0.30±0.27
$0.37 - 0.43$	0.628 ±0.13	0.453 ±0.13	$0.40 - 0.45$	0.18±0.22
$0.43 - 0.48$	0.961 ±0.12	0.865 ±0.12	$0.45 - 0.50$	-0.37±0.26
$0.48 - 0.54$	0.663 ±0.23	0.619 ±0.19		
$0.54 - 0.60$	1.14 ±0.17	0.832 ±0.32		

Table 26: Asymmetry(p_t^2) from Σ^-

$p_t^2 (GeV/c)^2$	D_s asymmetry A
$0.0 < p_t^2 < 0.5$	0.45±0.08
$0.5 < p_t^2 < 1.0$	0.64±0.10
$1.0 < p_t^2 < 1.5$	0.36±0.11
$1.5 < p_t^2 < 2.0$	0.36±0.15
$2.0 < p_t^2 < 2.5$	0.48±0.17
$2.5 < p_t^2 < 3.0$	0.58±0.19
$3.0 < p_t^2 < 3.5$	0.43±0.28
$3.5 < p_t^2 < 4.0$	0.79±0.41

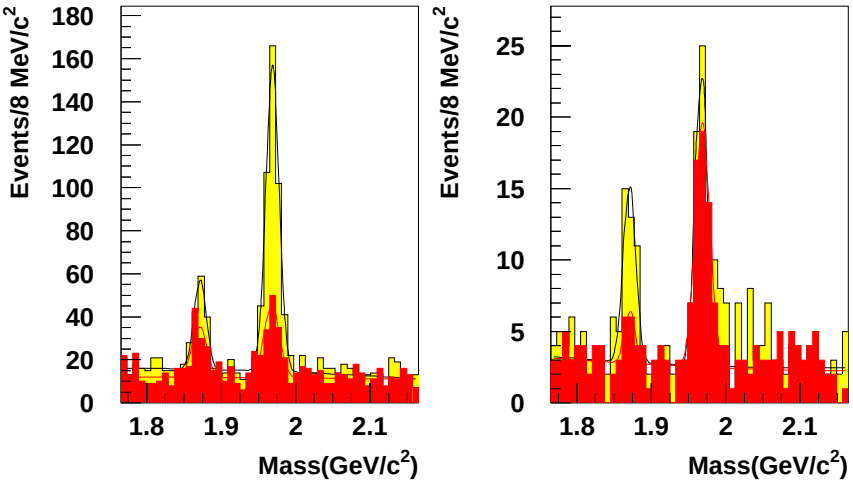

Figure 55: Integrated Asymmetry of D_s from Σ^- and π^- beam

6.4 Integrated Asymmetry

The overall asymmetry integrated over x_F can be calculated by fitting the signal for the charge conjugate states. In this analysis both D_s^- and D_s^+ total mass histograms are fitted to two Gaussians with a quadratic background. Figure 55. The yield for each charge state is calculated from the fit. Then the integral asymmetry is determined to be

Σ^- beam: $N_{D_s^-} = 396 \pm 21$, $N_{D_s^+} = 109 \pm 15$,

A($x_F > 0.2$)$\equiv$ 0.57 $\pm$ 0.07

π^- beam: $N_{D_s^-} = 52 \pm 26$, $N_{D_s^+} = 53 \pm 8$,

A($x_F > 0.2$)$\equiv$ -0.09 $\pm$ 0.08

This shows that there is a clear asymmetry in favor of D_s^- from the Σ^- beam where D_s^- is a leading particle. However there is no evidence of an asymmetry from the π^- beam where neither charge state is leading.

CHAPTER VII
DISCUSSION OF THE RESULTS

D_s charm meson hadroproduction has been studied in this thesis. Since D_s consists of one strange and one charm quark it is important to compare results with other mesons that do not contain a strange quark. We have studied a total of 792±37 $D_s^{\pm}$ events for this analysis. The raw data was corrected for the efficiencies and the yield was extracted using the sideband subtraction method. There is an obvious difference in the relative size of the production cross-sections between D_s^- and D_s^+. Our results clearly show that a charm meson which shares one quark with the beam particle is produced more copiously than one that does not. For the Σ^- beam D_s^- production is favored over D_s^+ at all x_F. Moreover, the difference is larger at large x_F (see Figure 56). We present this quantitatively for a range of x_F = 0.15 - 0.6. However we have found that both D_s^- and D_s^+ show the same behavior for the π^- beam which has no common quark with these particles. Our results agree with previous experimental results[1, 2]. Our results are compared with WA89 in Figure 57. We find they are consistent within statistical error.

E791[2] has high statistics for the D_s from the π^- beam. They have found almost zero asymmetry (0.032±0.022±0.022) in the x_F range of -0.1 to 0.5. Our statistics are much smaller, but still sufficient to study production asymmetry which we found also close to zero(-0.05±0.089 statistical error only). Production asymmetry as a function of p_t^2 shows an almost flat distribution over the range of 0.0 to 4.0 $(GeV/c)^2$

Two classes of phenomenological models exist for asymmetries. Color-drag or

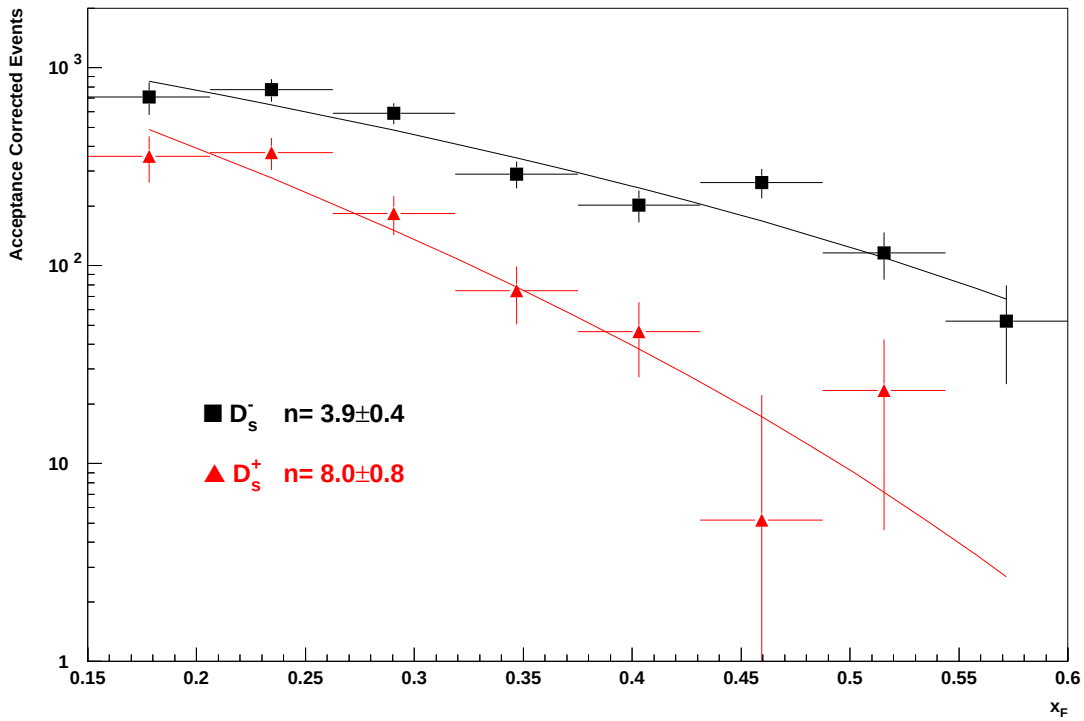

Figure 56: The acceptance corrected x_F distribution from Σ^- beam

String model and intrinsic charm model that are described in the chapter 2. The Color-drag model is pronounced at high x_F and does not depend on p_t, whereas the intrinsic charm model occurs at low p_t and large x_F.

Our results show that the production asymmetry is increasing as x_F increases and p_t^2 dependent asymmetry is flat so that the results favor the "color-drag" explanation of production asymmetry.

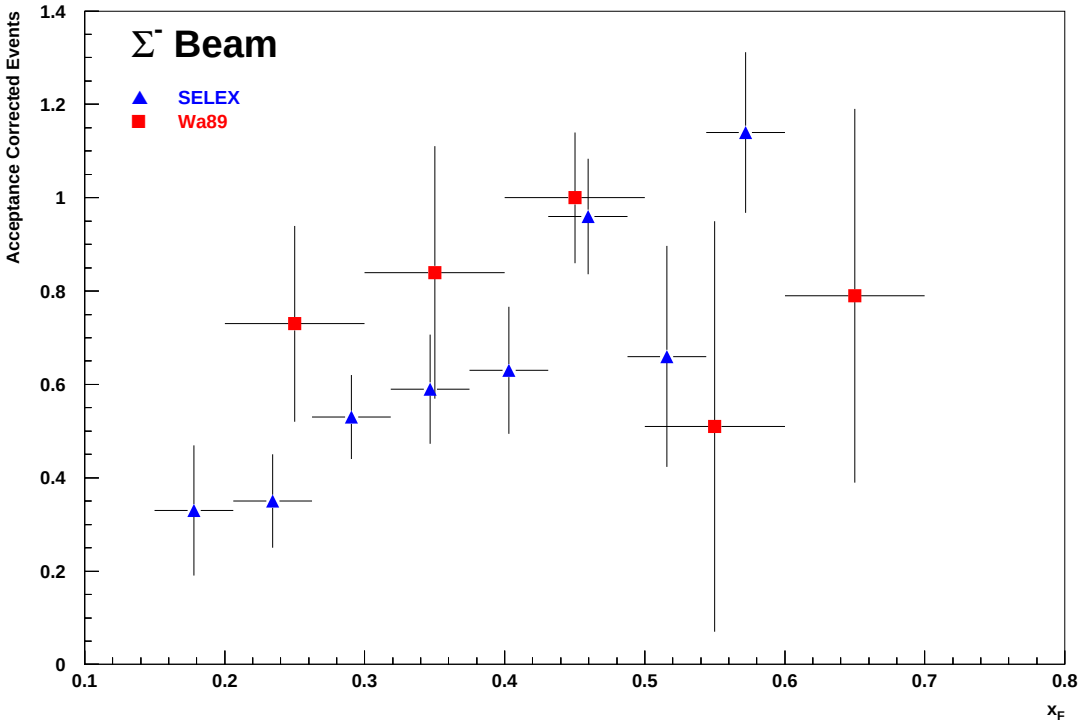

Figure 57: Comparison of the D_s production asymmetry as a function of x_F from a Σ^- beam. The acceptance corrected data are integrated over the x_F interval (0.15 - 0.6) for SELEX data and (0.2 - 0.7) for WA89 data

APPENDIX A
THE SELEX (E781) COLLABORATION

The SELEX Collaboration

G.P. Thomas
Ball State University, Muncie, IN 47306, U.S.A.

E. Gülmez
Bogazici University, Bebek 80815 Istanbul, Turkey

R. Edelstein, S.Y. Jun, A.I. Kulyavtsev[1], A. Kushnirenko, D. Mao[1], P. Mathew[2], M. Mattson, M. Procario[3], J. Russ, J. You[4]
Carnegie-Mellon University, Pittsburgh, PA 15213, U.S.A.

A.M.F. Endler
Centro Brasiliero de Pesquisas Físicas, Rio de Janeiro, Brazil

P.S. Cooper, J. Kilmer, S. Kwan, J. Lach, E. Ramberg, D. Skow, L. Stutte
Fermilab, Batavia, IL 60510, U.S.A.

V.P. Kubarovsky, V.F. Kurshetsov, A.P. Kozhevnikov, L.G. Landsberg, V.V. Molchanov, S.B. Nurushev, S.V. Petrenko, A.N. Vasiliev, D.V. Vavilov, V.A. Victorov
Institute for High Energy Physics, Protvino, Russia

Li Yunshan, Mao Chensheng, Zhao Wenheng, He Kangling, Zheng Shuchen, Mao Zhenlin
Institute of High Energy Physics, Beijing, P.R. China

M.Y. Balatz[5], G.V. Davidenko, A.G. Dolgolenko, G.B. Dzyubenko, A.V. Evdokimov, M.A. Kubantsev, I. Larin, V. Matveev, A.P. Nilov, V.A. Prutskoi, A.I. Sitnikov, V.S. Verebryusov, V.E. Vishnyakov
Institute of Theoretical and Experimental Physics, Moscow, Russia

U. Dersch[6], I. Eschrich[7], I. Konorov[8], H. Krüger[9], J. Simon[10], K. Vorwalter[11]
Max-Planck-Institut für Kernphysik, 69117 Heidelberg, Germany

I.S. Filimonov[5], E.M. Leikin, A.V. Nemitkin, V.I. Rud
Moscow State University, Moscow, Russia

A.G. Atamantchouk, G. Alkhazov, N.F. Bondar, V.L. Golovtsov, V.T. Kim, L.M. Kochenda, A.G. Krivshich, N.P. Kuropatkin, V.P. Maleev, P.V. Neoustroev, B.V. Razmyslovich, V. Stepanov, M. Svoiski, N.K. Terentyev[12], L.N. Uvarov, A.A. Vorobyov

Petersburg Nuclear Physics Institute, St. Petersburg, Russia

I. Giller, M.A. Moinester, A. Ocherashvili, V. Steiner
Tel Aviv University, 69978 Ramat Aviv, Israel

J. Engelfried[4], A. Morelos
Universidad Autónoma de San Luis Potosí, San Luis Potosí, Mexico

M. Luksys
Universidade Federal da Paraíba, Paraíba, Brazil

V.J. Smith
University of Bristol, Bristol BS8 1TL, United Kingdom

M. Kaya, E. McCliment, K.D. Nelson[13], C. Newsom, Y. Onel, E. Ozel, S. Ozkorucuklu, P. Pogodin
University of Iowa, Iowa City, IA 52242, U.S.A.

L.J. Dauwe
University of Michigan-Flint, Flint, MI 48502, U.S.A.

M. Gaspero, M. Iori
University of Rome "La Sapienza" and INFN, Rome, Italy

L. Emediato, C.O. Escobar[14], F.G. Garcia[4], P. Gouffon, T. Lungov[15], M. Srivastava,
R. Zukanovich-Funchal
University of São Paulo, São Paulo, Brazil

A. Lamberto, A. Penzo, G.F. Rappazzo, P. Schiavon
University of Trieste and INFN, Trieste, Italy

December 12, 2000

[1]Present address: Lucent Technologies, Naperville, IL
[2]Present address: SPSS Inc., Chicago, IL
[3]Present address: DOE, Germantown, MD
[4]Now at Fermilab, Batavia, IL 60510, U.S.A.
[5]deceased
[6]Present address: SAP, Walldorf, Germany
[7]Now at Imperial College, London SW7 2BZ, U.K.
[8]Now at Physik-Department, Technische Universität München, 85748 Garching, Germany
[9]Present address: The Boston Consulting Group, München, Germany
[10]Present address: Siemens Medizintechnik, Erlangen, Germany
[11]Present address: Deutsche Bank AG, Eschborn, Germany
[12]Now at Carnegie-Mellon University, Pittsburgh, PA 15213, U.S.A.
[13]Now at University of Alabama at Birmingham, Birmingham, AL 35294
[14]Now at Instituto de Física da Universidade Estadual de Campinas, UNICAMP, SP, Brazil
[15]Now at Instituto de Física Teórica da Universidade Estadual Paulista, São Paulo, Brazil

APPENDIX B
ADDITIONAL FIGURES

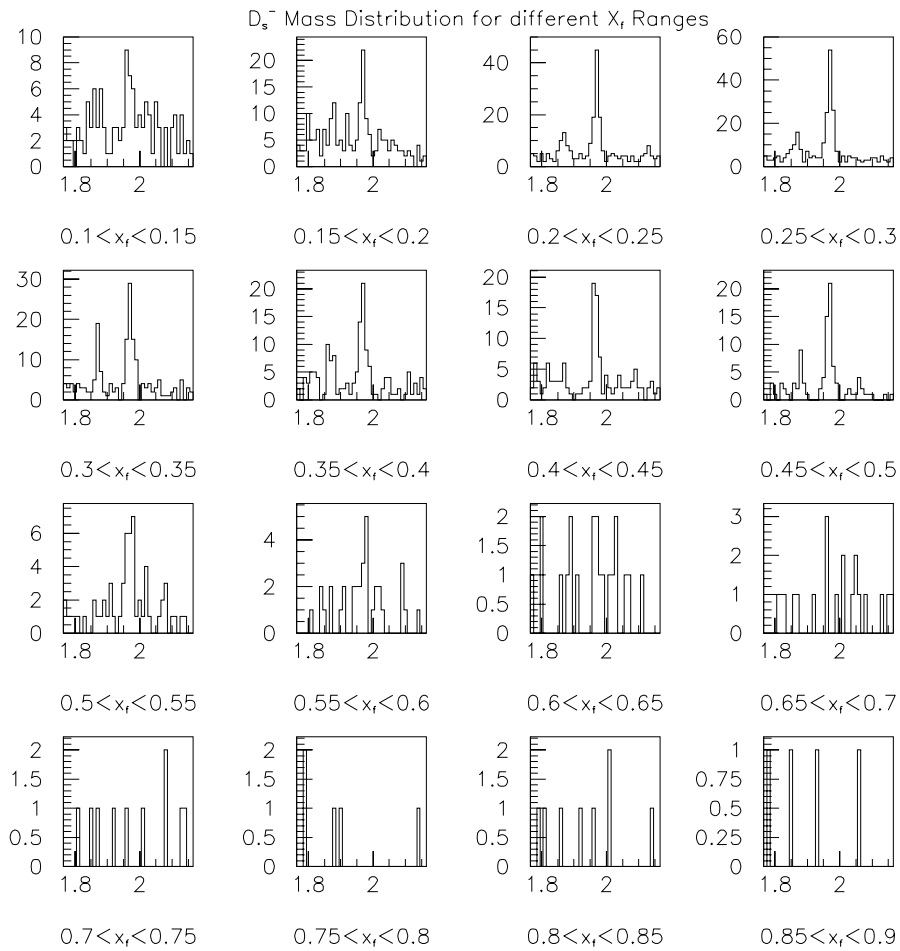

Figure 58: Mass distributions of $D_s^- \rightarrow K^+K^-\pi^-$ for different x_F ranges from Σ^- beam. y and x axis's show number of events($10\ MeV/c^2$) and invariant mass(GeV/c^2) respectively

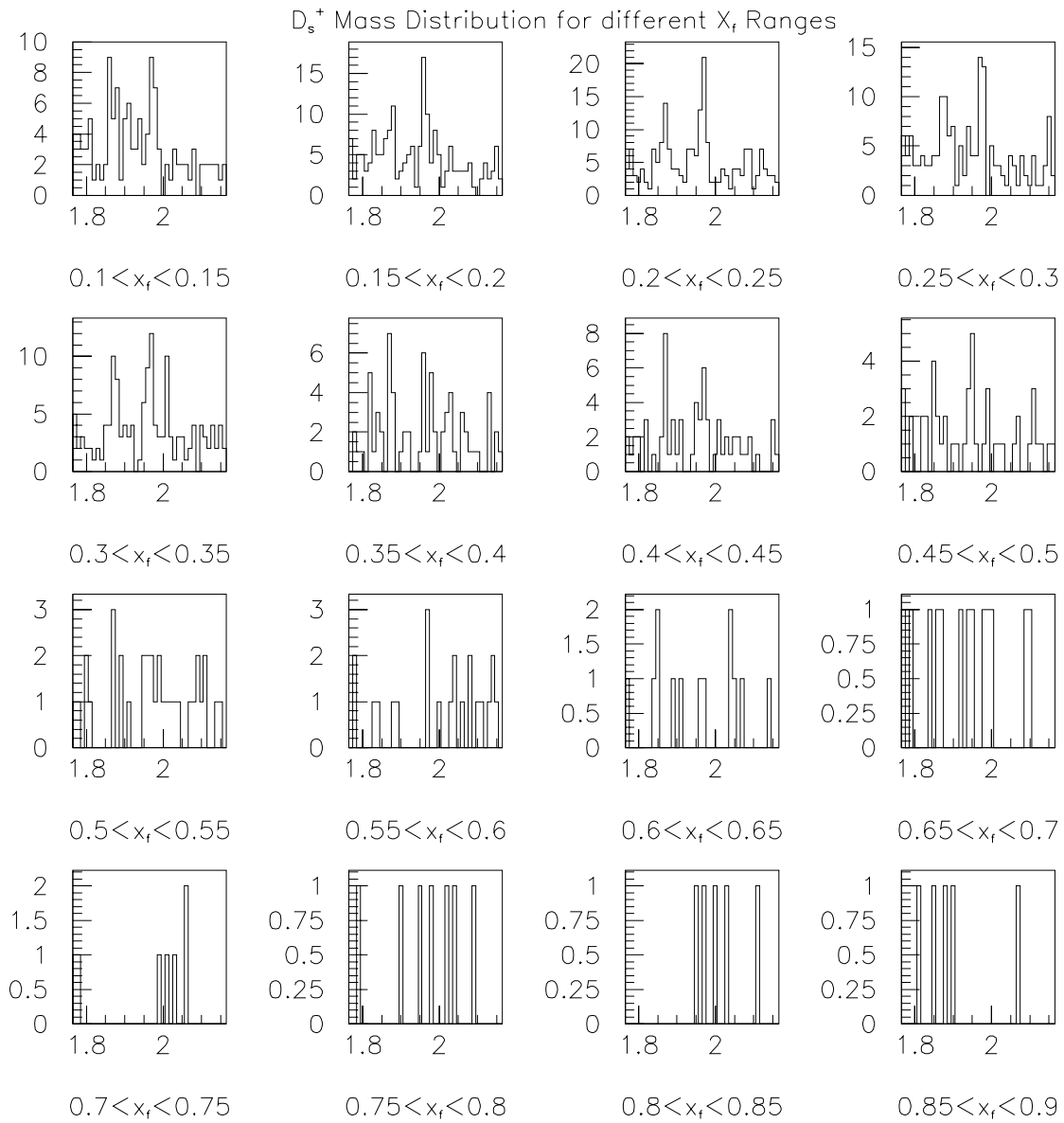

Figure 59: Mass distributions of $D_s^+ \to K^+K^-\pi^+$ for different x_F ranges from Σ^- beam. y and x axis's show number of events($10\ MeV/c^2$) and invariant mass(GeV/c^2) respectively

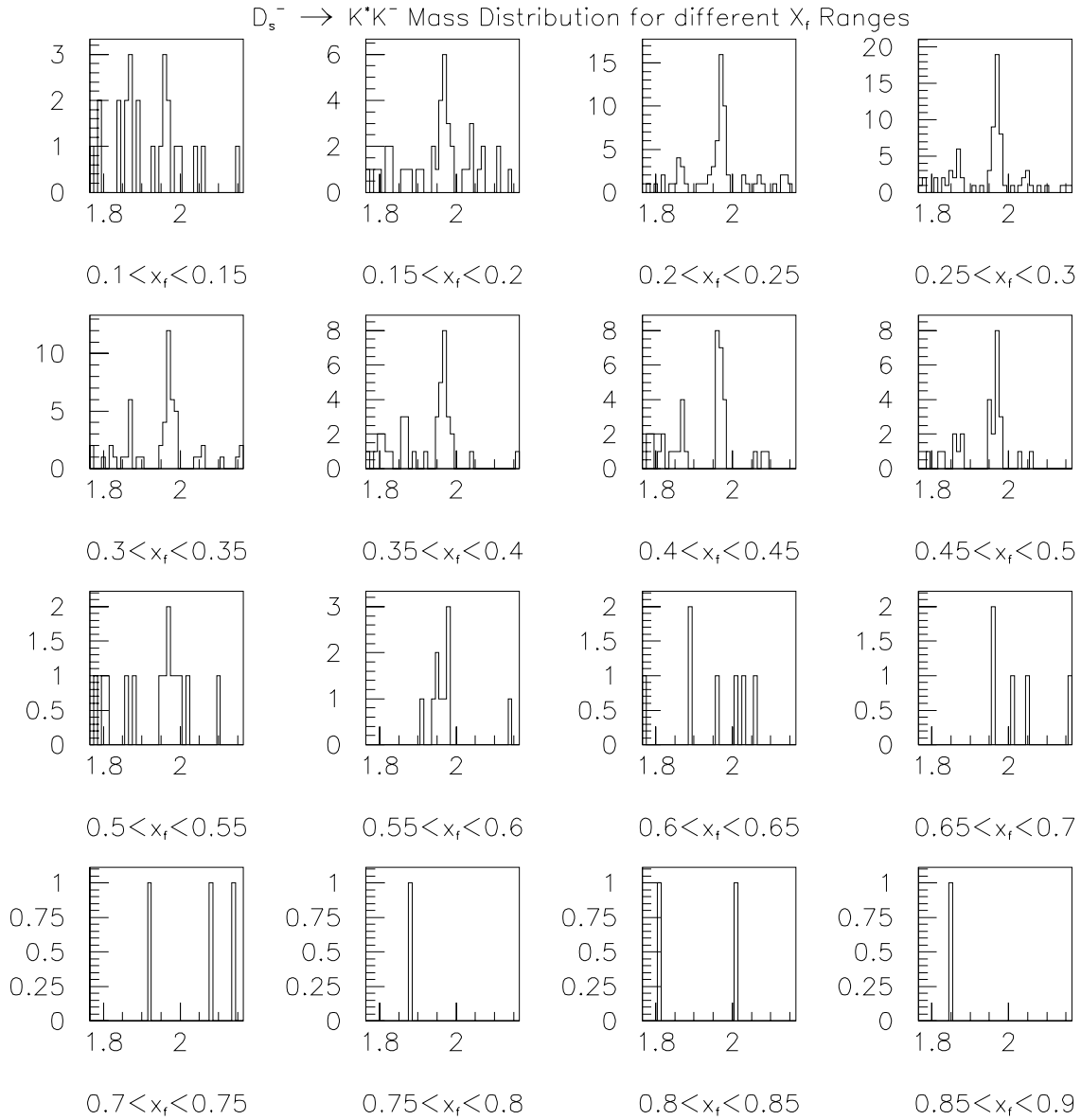

Figure 60: Mass distributions of $D_s^- \rightarrow K^*K^-$ for different x_F ranges from Σ^- beam. y and x axis's show number of events($10\ MeV/c^2$) and invariant mass(GeV/c^2) respectively

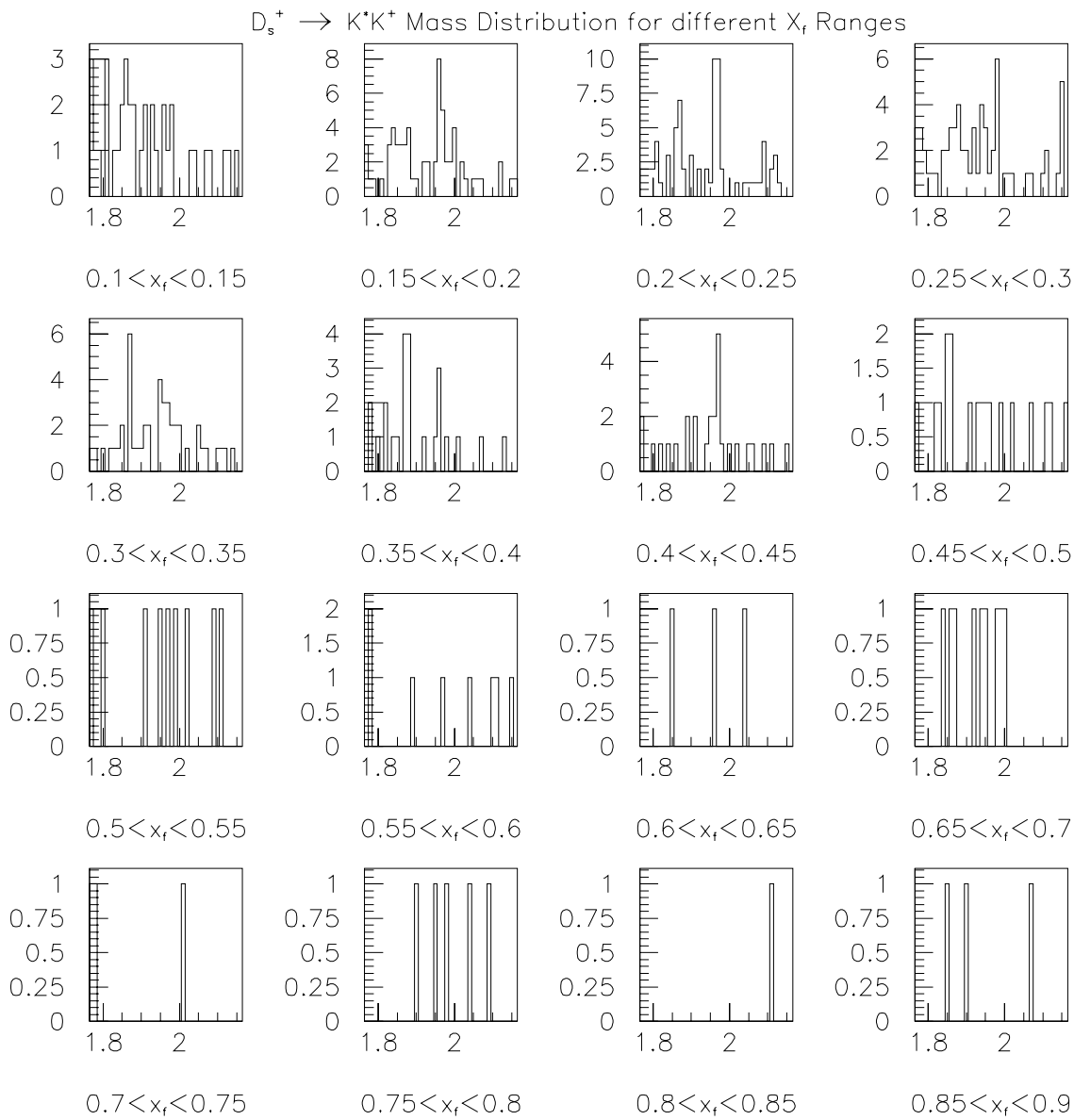

Figure 61: Mass distributions of $D_s^+ \rightarrow K^*K^+$ for different x_F ranges from Σ^- beam.y and x axis's show number of events(10 MeV/c^2) and invariant mass(GeV/c^2) respectively

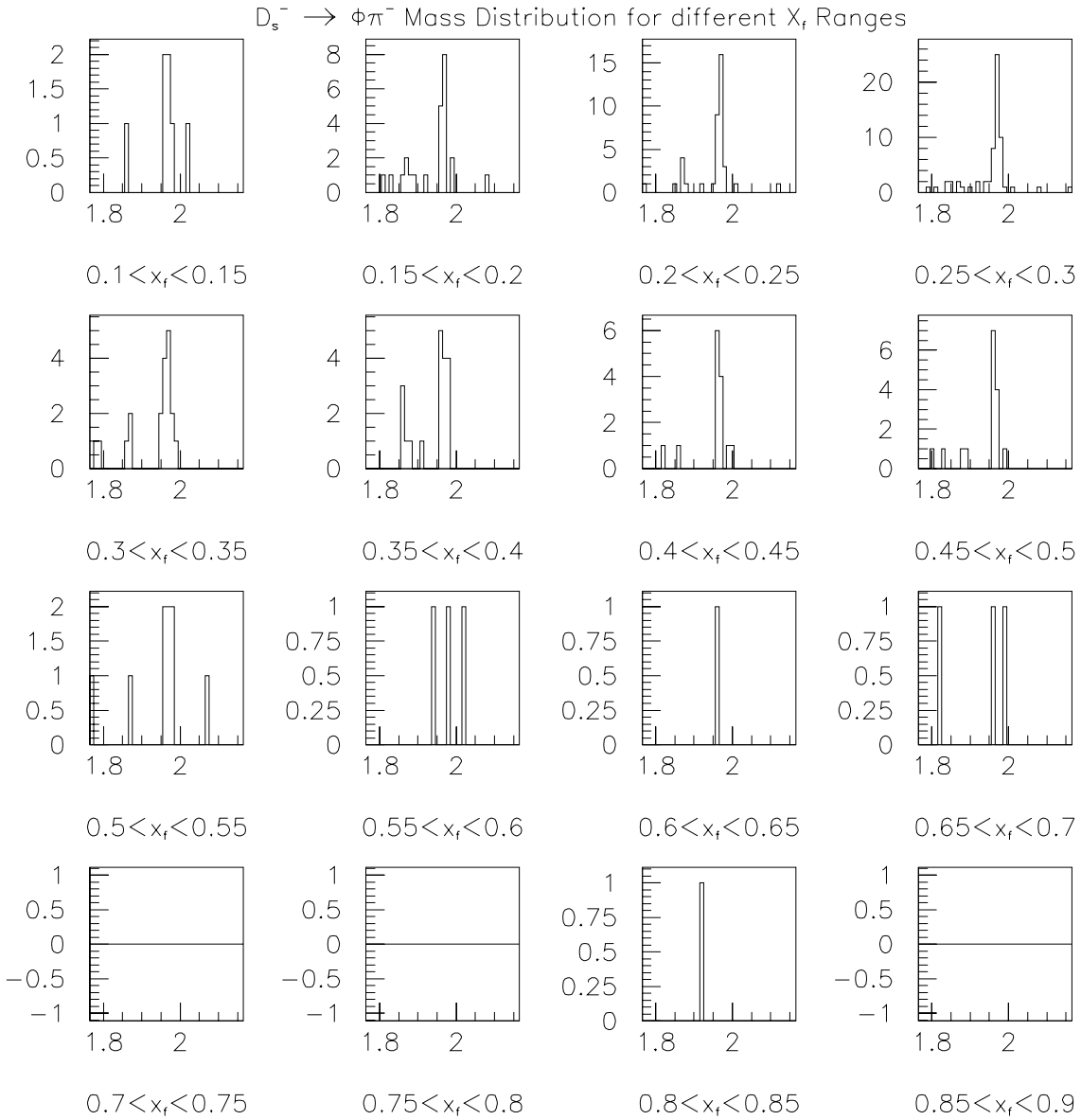

Figure 62: Mass distributions of $D_s^- \rightarrow \phi\pi^-$ for different x_F ranges from Σ^- beam. y and x axis's show number of events(10 MeV/c^2) and invariant mass(GeV/c^2) respectively

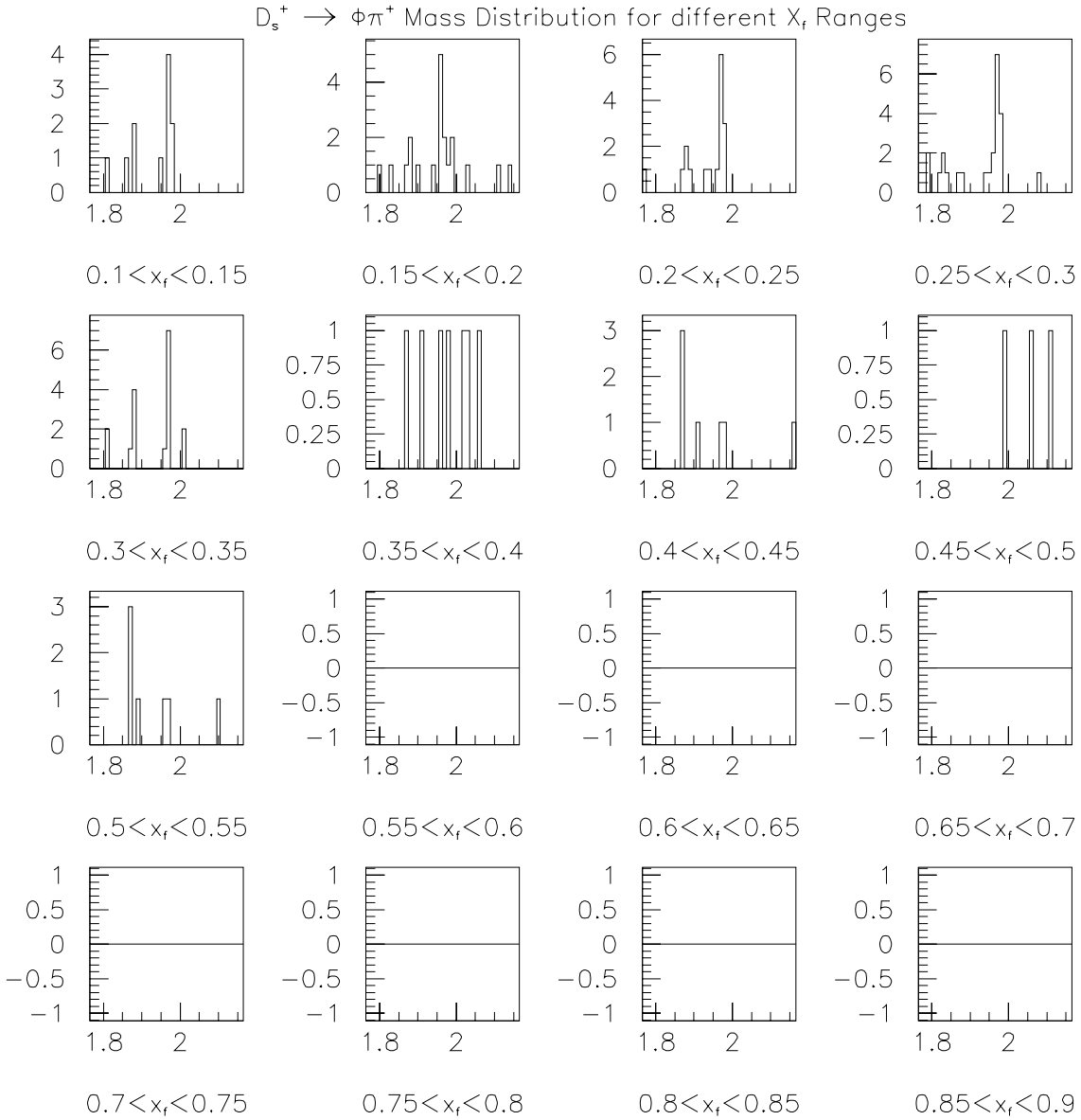

Figure 63: Mass distributions of $D_s^+ \rightarrow \phi\pi^+$ for different x_F ranges from Σ^- beam. y and x axis's show number of events(10 MeV/c^2) and invariant mass(GeV/c^2) respectively

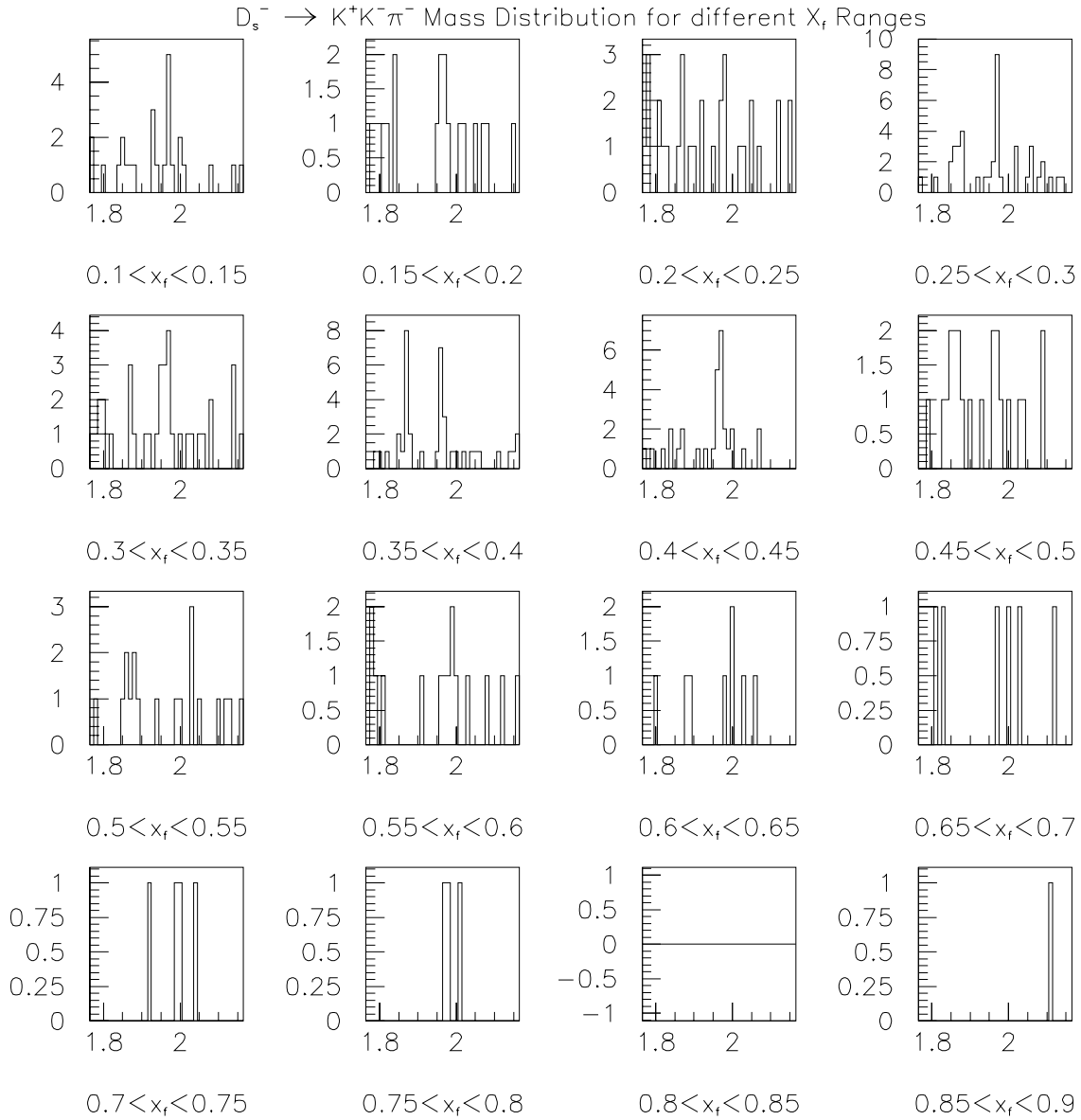

Figure 64: Mass distributions of $D_s^- \rightarrow K^-K^+\pi^-$ for different x_F ranges from π^- beam. y and x axis's show number of events($10\ MeV/c^2$) and invariant mass(GeV/c^2) respectively

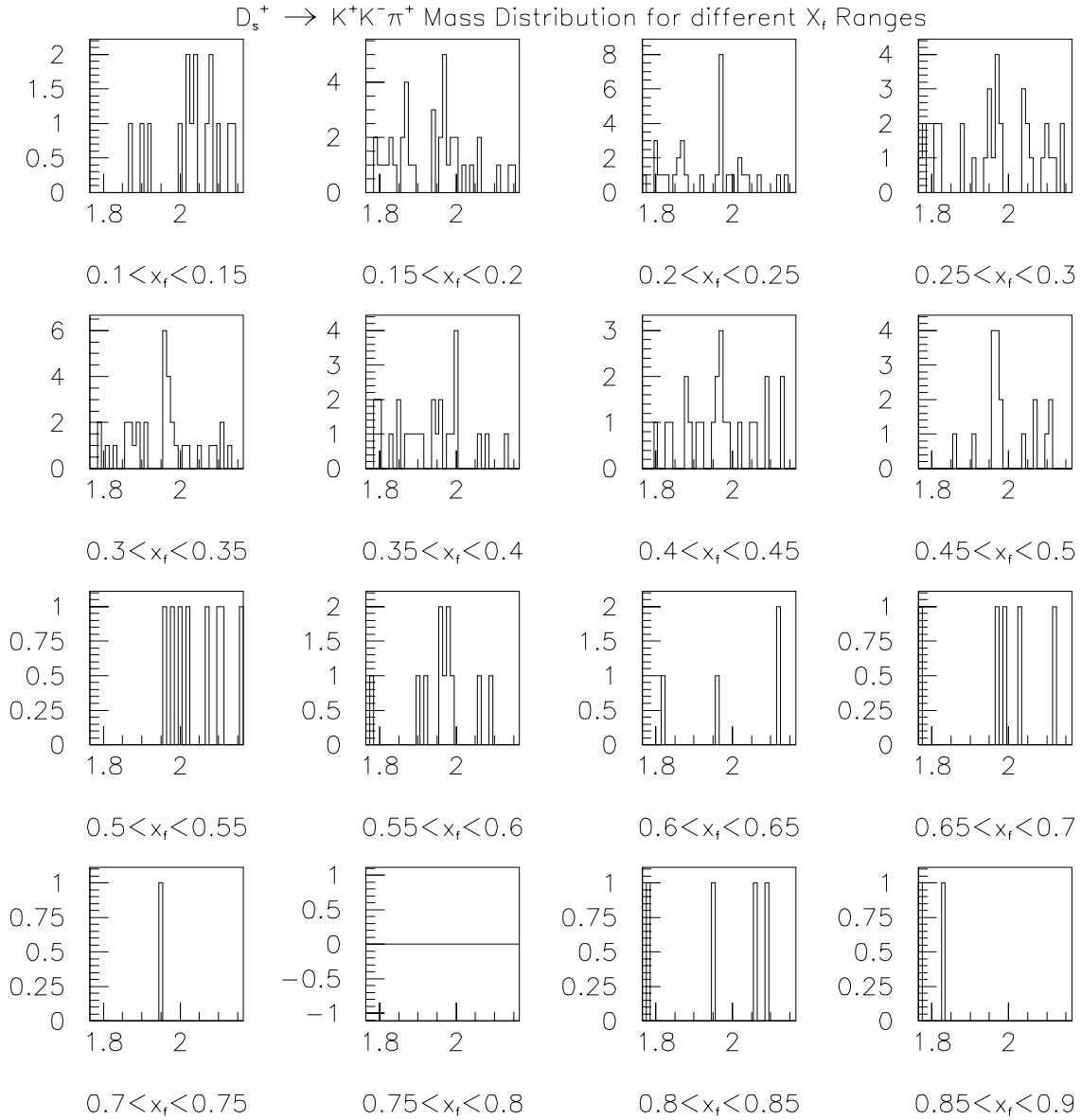

Figure 65: Mass distributions of $D_s^+ \rightarrow K^-K^+\pi^+$ for different x_F ranges from π^- beam. y and x axis's show number of events($10\ MeV/c^2$) and invariant mass(GeV/c^2) respectively

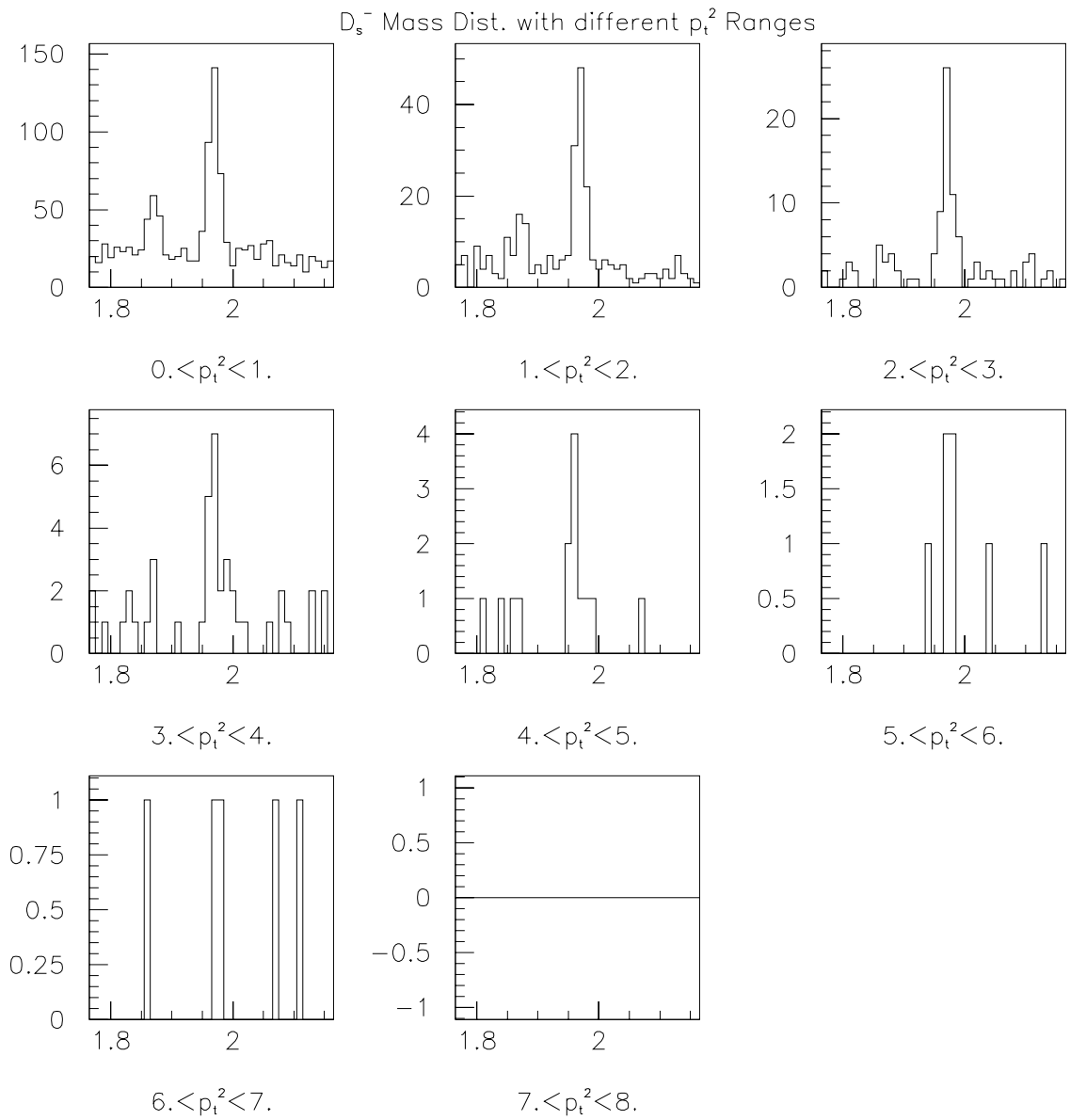

Figure 66: Mass distributions of $D_s^- \to K^-K^+\pi^-$ for different p_t^2 ranges from Σ^- beam. y and x axis's show number of events($10\ MeV/c^2$) and invariant mass(GeV/c^2) respectively

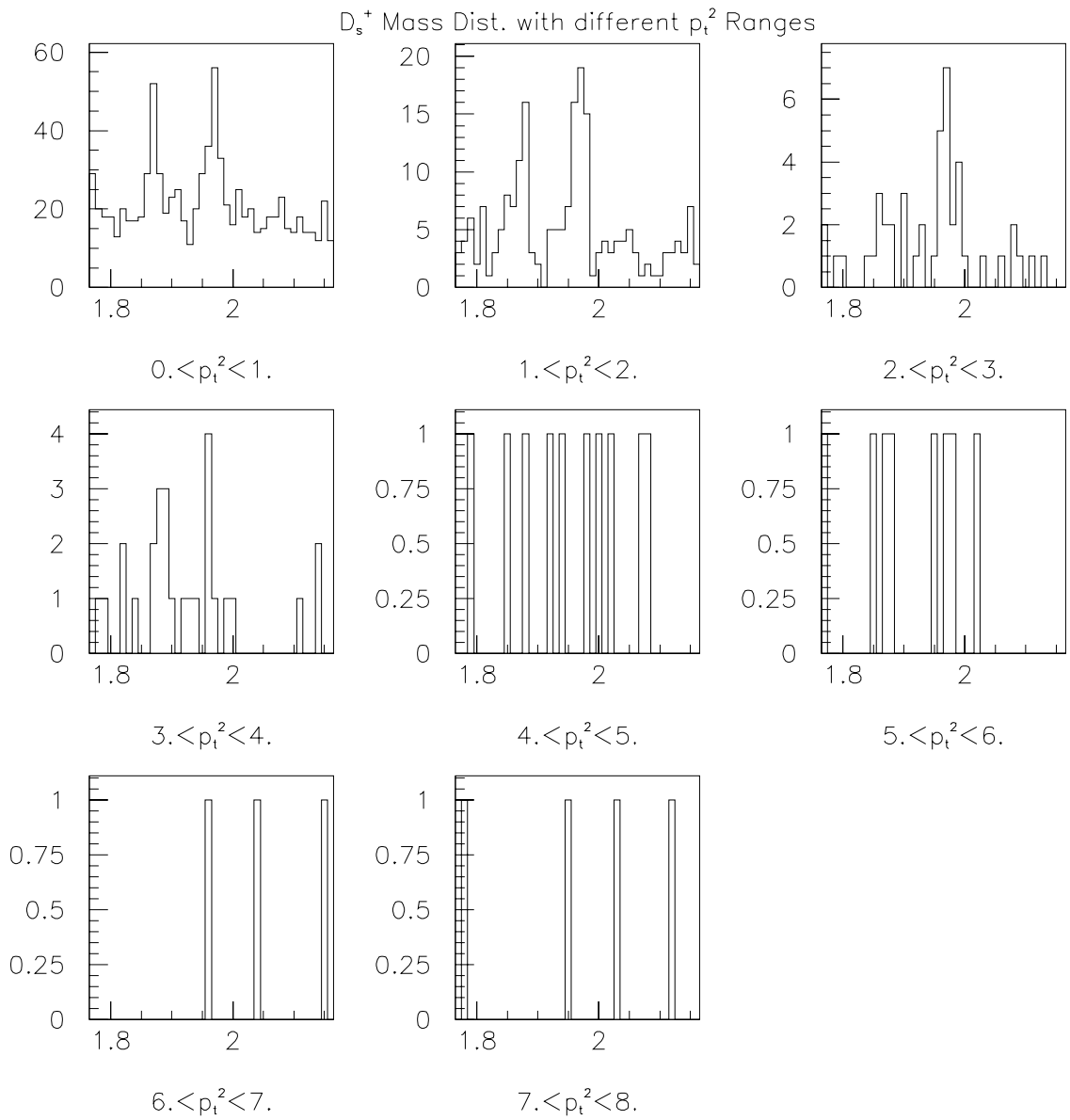

Figure 67: Mass distributions of $D_s^+ \to K^-K^+\pi^+$ for different p_t^2 ranges from Σ^- beam. y and x axis's show number of events($10\ MeV/c^2$) and invariant mass(GeV/c^2) respectively

REFERENCES

[1] WA89 Collaboration, M.Adamovich *et al.*, Eur. Phys. J. **C8**, 593, (1999)

[2] E791 Cllaboration, E.M. Aitala *et al.*, Phys. Lett. **B411**, 230, (1997)

[3] E769 Collaboration, G.A. Alves *et al.*, Phys. Rev. Lett. **72**, 812, (1994)

[4] Piskounova O.I. e-Print Archive: hep-ph/9904208, (1999)

[5] WA82 Collaboration, M. Adamovich *et al.*, Phys. Lett. **B305**, 402, (1993)

[6] P. Nason, S. Dawson and K. Ellis, Nucl. Phys. **B327**, 49, (1989)

[7] S.Frixione, M.L. Mangano, P. Nason, G. Ridolfi, Nucl. Phys. **B431**,453, (1994)

[8] E791 Cllaboration, E.M. Aitala *et al.*, Phys. Lett. **B371**, 157, (1996)

[9] H.-U. Bengtsson and T. Sjostrand, Comp. Phys. Comm. 46, 43 (1987)

[10] E. Norrbin, T. Sjostrand (Lund U.). e-Print Archive: hep-ph/9905493, (1999)

[11] E. Norrbin, T. Sjostrand , e-Print Archive: hep-ph/9809266, (1998)

[12] E. Norrbin, T. Sjostrand (Lund U.). Eur. Phys. J. **C17**, 137, (2000)

[13] S.J. Brodsky et al., Phys. Lett. **93B**, 451, (1980)

[14] T. Gutierrez and R. Vogt, Nucl. Phys. **B539**, 189, (1999)

[15] R.C. Hwa, Phys. Rev. **D51**, 85, (1995)

[16] R. Vogt and S.J. Brodsky, Nucl. Phys. **B438**, 261, (1995)

[17] S.J. Brodsky, C. Peterson and N. sakai, Phys. Rev. **D23**, 2745, (1981)

[18] SELEX Internal Notes (FNAL/E781/H-808) E781 Hyperon Spectrometer Constants, J.Lach,3/21/99

[19] K. Konigsman *et. al.* The Large Angle Silicon Detectors (LASD) for E781, SELEX Internal Report (FNAL/E781/H-661)

[20] F. Sauli Lectures given in the Academic Training Program of CERN 1975-1976 Geneva, 1977

[21] J.C Tarle and H.Verweij, "RMH module, type 4236", Technical Specifications,CERN, NP Division, (1975)

[22] W.R. Leo, "Techniques for Nuclear and Particle Physics Experiments", Berlin, (1994)

[23] Engelfried J. *et al.* Nucl. Instrum. Methods A **431**, 53, (1999)

[24] SELEX Internal Notes (FNAL/E781/H-697), The E781 Trigger and Data Acquisition System;J.Engelfried. Talk at the CHARM2000 Workshop, Fermilab, june 7-9, 1994

[25] R.Pordes et al., "Data Flow Manager for DART", **FERMILAB-CONF-94-104**

[26] Physics Analysis Workstation, An Introductary Tutorial, Application Software Group Computing and Networks Division CERN Geneva, Switzerland.(*http* : *//wwwinfo.cern.ch/asd/paw/index.html*)

[27] *http* : *//www.lns.cornell.edu/public/CLEO/soft/QQ/qq_expert.html*

[28] Particle Data Group, Phys. Rev. **D54**, 471, (1996)

[29] Review of Particle Physics D.E. Groom *et al.*, The European Physical Journal **C15**, 1, (2000)

[30] R. Vogt, S.J. Brodsky Nucl. Phys. **B478**, 311, (1996)

[31] Kaidalov A.B. Physics lett. **116B**, 459, (1982)

[32] J.C. Anjos, E. Cuautle (Rio de Janeiro,CBPF). CBPF-NF-026-00, **hep-ph/0005057** 27pp, (1999)

[33] Richard P. Feynman Phys. Rev. Lett. **23**, 1415, (1969)

[34] M. Aquilar-Benitez *et al.*, Z.Phys. **C31**, 491, (1986)

[35] S. Barlag *et al.*, Z.Phys. **C49**, 555, (1991)